Physiological and Pharmacological Regulation of Ferroptosis

Inaugural-Dissertation

zur Erlangung des Doktorgrades
der Mathematisch-Naturwissenschaftlichen Fakultät
der Heinrich-Heine-Universität Düsseldorf

vorgelegt von

Leonie Christin Thewes
aus Hagen

Düsseldorf, Mai 2025

aus der Klinik für Neurologie des
Universitätsklinikums Düsseldorf und
der Heinrich-Heine-Universität Düsseldorf

Gedruckt mit der Genehmigung der
Mathematisch-Naturwissenschaftlichen Fakultät der
Heinrich-Heine-Universität Düsseldorf

Berichterstatter:

1. PD Dr. Carsten Berndt

2. Prof. Dr. Petra Bauer

Tag der mündlichen Prüfung: 12.09.2025

Table of contents

1 List of scientific contributions based on data of this thesis

1.1 Publications

1.1.1 Glutaredoxin 2-dependent glutathionylation modulates Glutathione peroxidase 4 functionality

All authors:

Leonie Thewes, Yana Bodnar, Irina Ingold, Lora Denson, Morris Haid, Hend Abdelhamid, Daniel Trnka, Hannah Weber, Tim Prozorovski, Sven G. Meuth, Orhan Aktas, Christoph Thiele, Manuel Etzkorn, Yvonne M. W. Janssen-Heininger, Gereon Poschmann, Christopher H. Lillig, Marcus Conrad, Carsten Berndt.

Copyright notice:

Summary and contribution:

Ferroptosis is an iron-dependent form of cell death that is characterized by lipid peroxidation. Glutathione peroxidase 4 (GPX4) is key player in the protection against ferroptosis, as it is the only enzyme capable of converting toxic lipid peroxides in phospholipids to their corresponding alcohols. This study proposes a potential physiological regulation of ferroptosis based on redox regulation. The glutathionylation of GPX4 at cysteine 75 has been demonstrated to result in a shift in electrostatic surface potential, thereby impairing the binding of phospholipids and consequently decreasing cell survival upon ferroptosis induction. The present study characterizes glutaredoxin 2 as a modulator of ferroptosis, as it is able to reduce the glutathionylation of GPX4, thus increasing its binding to phospholipids and enhancing the resistance against ferroptosis. My contribution to this research project entailed the management of the project, as well as the planning, execution, and analysis of the majority of the experiments. These experiments included cell culture, cell survival, detection of lipid peroxidation, immunoprecipitation of GPX4, detection of glutathionylated GPX4, fluorescent GSSG labeling, protein quantification, electrophoresis and western blot, GPX4 activity, and bio-layer interferometry measurements and immunohistochemistry. Furthermore, I have contributed to the preparation of the manuscript.

1.1.2 Diroximel fumarate protects against neuroinflammation via upregulation of anti-ferroptotic pathways

All authors:

Katinka Fischer*, **Leonie Thewes***, Tim Prozorovski, Mary Bayer, Torsten Lowin, Philipp Albrecht, Sven G. Meuth, Orhan Aktas, Carsten Berndt.

*These authors contributed equally to this project and should be considered as co-first authors

Copyright notice:

Summary and contribution:

Inflammatory diseases affect millions of people worldwide, with multiple sclerosis (MS) serving as a prime example. MS is characterized by chronic inflammation of the central nervous system, leading to demyelination, axonal damage, and progressive neurological disability. Despite the absence of a definitive cure, therapeutic interventions such as diroximel fumarate (DRF) have demonstrated efficacy in delaying disease progression, primarily through the activation of the NRF2 pathway, which enhances the expression of antioxidant proteins. Ferroptosis, an iron-dependent form of cell death driven by lipid peroxidation, has been identified as a pathological hallmark not only in MS but also in the inflammatory diseases rheumatoid arthritis (RA), a chronic autoimmune joint disease, and osteoarthritis (OA), a degenerative joint disorder. The objective of this study was to investigate the potential protective effect of DRF against ferroptosis in these diseases. We demonstrated that DRF effectively protected against ferroptosis-induced damage in mouse myelin and improved the survival of ferroptosis-challenged rat oligodendrocytes. Furthermore, DRF treatment led to an upregulation of key ferroptosis-related genes (*FSP1, SLC7A11, GPX4*) in rat oligodendrocytes. Additionally, GPX4 protein expression was found to be elevated in MS patients treated with the predecessor drug dimethyl fumarate (DMF). Conversely, DRF exhibited no protective effects in synovial fibroblasts from patients with RA or OA, with no alterations observed in cell survival, lipid peroxidation, and GPX4 expression, or with these effects being only slightly diminished. These findings suggest that the protective effect of DRF is tissue- and disease-specific and may involve mechanisms beyond classical ferroptosis inhibition. My contribution to this research was

to translate the results found in MS and neuronal-related tissues and cells into tissues and cells derived from RA and OA samples. This process entailed the execution of a series of assays, encompassing cell survival assays, lipid peroxidation detection using immunohistochemistry and flow cytometry, gel electrophoresis, western blot analysis, and qPCR. Furthermore, I have contributed to the preparation of the manuscript.

1.2 Presentations

Leonie Thewes, Yana Bodnar, Daniel Trnka, Gereon Poschmann, Manuel Etzkorn, Christoph Thiele, Marcus Conrad, Christopher Horst Lillig, Carsten Berndt. Grx2 regulates posttranslational modifications of GPX4 and ferroptosis.
Symposium of RTG 2578 (2023, Düsseldorf - Germany) – Award for best presentation

Leonie Thewes, Carsten Berndt. H_2O_2 and iron: small molecules inducing cell death.
Redox Research Rheinland (2024, Düsseldorf – Germany)

Leonie Thewes, Yana Bodnar, Manuel Etzkorn, Gereon Poschmann, Christoph Thiele, Torsten Lowin, Yvonne Janssen-Heiniger, Christopher Horst Lillig, Marcus Conrad, Carsten Berndt. Glutaredoxin-dependent thiol redox regulation as modulator of ferroptosis.
Gordon Research Conference "Thiol-Based Redox Regulation and Signaling" (2024, Barcelona - Spain)

Leonie Thewes, Yana Bodnar, Manuel Etzkorn, Gereon Poschmann, Christoph Thiele, Torsten Lowin, Yvonne Janssen-Heiniger, Christopher Horst Lillig, Marcus Conrad, Carsten Berndt. Glutaredoxin-dependent thiol redox regulation as modulator of ferroptosis.
Symposium of iBrain Graduate School (2024, Düsseldorf – Germany)

Presentations at international retreats *(2022, Utrecht; 2024, Brussels)*

1.3 Poster presentations

Leonie Thewes, Hanna Weber, Daniel Trnka, Gereon Poschmann, Christoph Thiele, Marcus Conrad, Christopher Horst Lillig, Carsten Berndt. Glutathionylation regulates activity of GPX4 and thereby sensitivity against ferroptosis. *EMBO Workshop "Thiol oxidation in biology: Biochemical mechanisms to physiological outcomes" (2022, Sant Feliu de Guixols – Spain) – Award for best poster*

Leonie Thewes, Hanna Weber, Daniel Trnka, Gereon Poschmann, Christoph Thiele, Marcus Conrad, Christopher Horst Lillig, Carsten Berndt. Glutathionylation regulates

activity of GPX4 and thereby sensitivity against ferroptosis. *Symposium of RTG 2578 (2022, Radevormwald – Germany)*

Leonie Thewes, Hanna Weber, Daniel Trnka, Gereon Poschmann, Christoph Thiele, Marcus Conrad, Christopher Horst Lillig, Carsten Berndt. Glutathionylation regulates activity of GPX4 and thereby sensitivity against ferroptosis. *Symposium of SPP 2306 (2022, Dresden – Germany)*

Leonie Thewes, Yana Bodnar, Daniel Trnka, Gereon Poschmann, Manuel Etzkorn, Christoph Thiele, Marcus Conrad, Christopher Horst Lillig, Carsten Berndt. Grx2 regulates posttranslational modifications of GPX4 and ferroptosis. *Compartmentalized Redox Biology (2023, Düsseldorf – Germany)*

Leonie Thewes, Yana Bodnar, Manuel Etzkorn, Gereon Poschmann, Christoph Thiele, Torsten Lowin, Yvonne Janssen-Heiniger, Christopher Horst Lillig, Marcus Conrad, Carsten Berndt. Glutaredoxin-dependent thiol redox regulation as modulator of ferroptosis. *Gordon Research Conference "Thiol-Based Redox Regulation and Signaling" (2024, Barcelona - Spain)*

Leonie Thewes, Yana Bodnar, Manuel Etzkorn, Christoph Thiele, Gereon Poschmann, Christopher Horst Lillig, Marcus Conrad, Carsten Berndt. Thiol redox regulation of ferroptosis. *Cold Spring harbor Conference Asia "Iron, Reactive Oxygen Species & Ferroptosis In Life, Death & Disease" (2024, Suzhou – China) – selected for oral presentation*

Leonie Thewes, Yana Bodnar, Daniel Trnka, Gereon Poschmann, Manuel Etzkorn, Christoph Thiele, Marcus Conrad, Christopher Horst Lillig, Carsten Berndt. Grx2 regulates posttranslational modifications of GPX4 and ferroptosis. *EMBO Workshop "Ferroptosis: When Metabolism Meets Cell Death" (2023, Seeon – Germany)*

Tim Prozorovski, **Leonie Thewes**, Gereon Poschmann, Christina Wilms, Lars Bräutigam, Benjamin Odermatt, Guido Reifenberger, Orhan Aktas, Carsten Berndt. Glutaredoxin-

dependent differentiation and survival in the brain. *Redox Sendai Week (2025, Sendai – Japan)*

2 List of figures

3 List of tables

4 Abstract

Ferroptosis is a non-apoptotic, iron-dependent cell death mechanism that relies on the accumulation of lipid peroxides. While several aspects of ferroptosis have been described in recent years, physiologically relevant molecular mechanisms modulating ferroptosis are still poorly understood.

This study identifies a novel redox-dependent mechanism that regulates ferroptosis through posttranslational modification of glutathione peroxidase 4 (GPX4), a central enzyme in the suppression of ferroptosis. It is shown that glutathionylation at cysteine 75 of GPX4 impairs its ability to bind to cell membranes, thereby inhibiting its lipid peroxide-reducing activity and making cells more susceptible to ferroptotic cell death. Furthermore, the obtained data show that glutaredoxin 2 (Grx2), a key player in redox regulation, can reverse this glutathionylation, thereby restoring GPX4's membrane association and ability to reduce lipid peroxidation. This redox-dependent regulation by Grx2 represents one of the first described physiological mechanisms that directly modulates ferroptosis sensitivity. To investigate this mechanism, a combination of cellular, tissue-based and biochemical models have been used, in particular cells and tissues from transgenic mice as well as proteins isolated from these.

Beyond the mechanistic insight, the relevance of drug-dependent regulation of ferroptosis in disease context was investigated. Ferroptosis is associated with inflammatory diseases such as multiple sclerosis (MS), rheumatoid arthritis (RA) and osteoarthritis (OA), in which oxidative stress and lipid peroxidation contribute to disease progression. Although previous data from our research group has been shown that the MS drug diroximel fumarate protects oligodendroglia cells and MS patients against ferroptosis, this work shows that it has no protective effect on cells derived from RA and OA patients. For this part of the study, human cells and tissues from OA and RA patients were used.

In summary, this work uncovers a previously unknown, physiologically relevant mechanism of ferroptosis regulation by Grx2-mediated control of GPX4 activity and highlights the importance of cell-specific responses in the development of ferroptosis therapies. Key techniques included cell survival assays and lipid peroxidation detection by

flow cytometry, as well as western blot, immunohistochemistry, and qPCR to analyze protein and mRNA expression.

5 Zusammenfassung

Ferroptose ist ein nicht-apoptotischer, eisenabhängiger Zelltodmechanismus, der auf der Akkumulation von Lipidperoxiden beruht. Obwohl in den letzten Jahren mehrere Aspekte der Ferroptose beschrieben wurden, sind die physiologisch relevanten molekularen Mechanismen, welche die Ferroptose modulieren, noch immer kaum erforscht.

Diese Studie identifiziert einen neuartigen redoxabhängigen Mechanismus, der die Ferroptose durch posttranslationale Modifikation von Glutathionperoxidase 4 (GPX4), einem zentralen Enzym bei der Unterdrückung der Ferroptose, reguliert. Es wird gezeigt, dass die Glutathionylierung an Cystein 75 von GPX4 dessen Fähigkeit beeinträchtigt, an Zellmembranen zu binden, wodurch die Lipidperoxid-reduzierende Aktivität gehemmt wird und Zellen anfälliger für ferroptotischen Zelltod werden. Darüber hinaus zeigen die gewonnenen Daten, dass Glutaredoxin 2 (Grx2), ein wichtiges Element in der Redoxregulation, diese Glutathionylierung rückgängig machen kann, wodurch die Membranassoziation von GPX4 und die Fähigkeit, die Lipidperoxidation zu reduzieren, wiederhergestellt werden. Diese redoxabhängige Regulierung durch Grx2 stellt einen der ersten physiologischen Mechanismen dar, der die Ferroptose-Empfindlichkeit direkt moduliert. Um diesen Mechanismus zu untersuchen, wurde eine Kombination aus zellulären, gewebebasierten und biochemischen Modellen verwendet, insbesondere Zellen und Gewebe von transgenen Mäusen, sowie aus Zellen isolierte Proteine.

Über diese mechanistische Erkenntnis hinaus wurde die Relevanz therapieabhängiger Regulation von Ferroptose im Krankheitskontext untersucht. Ferroptose wird mit entzündlichen Erkrankungen wie Multipler Sklerose (MS), rheumatoider Arthritis (RA) und Osteoarthritis (OA) in Verbindung gebracht, bei denen oxidativer Stress und Lipidperoxidation zum Fortschreiten der Krankheit beitragen. Obwohl frühere Daten unserer Arbeitsgruppe zeigen, dass das MS-Medikament Diroximelfumarat Oligodendrozyten und MS-Patienten vor Ferroptose schützt, zeigt diese Arbeit, dass es keinen schützenden Effekt auf Zellen von RA- und OA-Patienten hat. Für diesen Teil der Studie wurden menschliche Zellen und Gewebe von OA- und RA-Patienten verwendet.

Zusammenfassend deckt diese Arbeit einen bisher unbekannten, physiologisch relevanten Mechanismus der Ferroptoseregulierung durch Grx2-vermittelte Kontrolle der GPX4-Aktivität auf und unterstreicht die Bedeutung zellspezifischer Reaktionen bei der Entwicklung von Ferroptosetherapien. Zu den wichtigsten Methoden gehörten Zellüberlebenstests und der Nachweis der Lipidperoxidation mittels Durchflusszytometrie sowie Western Blotting, Immunhistochemie, und qPCR zur Analyse der Protein- und mRNA-Expression.

6 Introduction

6.1 Ferroptosis

Cell death can be classified into two broad categories: accidental cell death (ACD) and regulated cell death (RCD). ACD is triggered by severe insults of physical, chemical, or mechanical nature (e.g. temperature fluctuations, pH variations, shear forces). In contrast, RCD is characterized by the engagement of a genetically encoded molecular apparatus, contingent on both extra- and intracellular signals [1-3]. Beyond apoptosis, the most widely recognized form of RCD, there is also regulated necrosis, which includes several subtypes of cell death, such as necroptosis, pyroptosis, parthanatos and ferroptosis [4-6]. First proposed by Scott Dixon in 2012, ferroptosis results from a complex interplay between iron, oxygen, and oxidizable phospholipids within the cell [7, 8]. A distinguishing feature of ferroptosis is the accumulation of phospholipid peroxides, which sets it apart from other forms of regulated necrosis [3, 7, 9]. Morphologically, ferroptosis is characterized by a reduction in mitochondrial volume and increased bilayer membrane density, while the nucleus maintains its normal size and chromatin does not condense [7, 8]. The biochemical processes involved in ferroptosis are described in more detail in the following subchapters.

6.1.1 Iron metabolism

Iron (Fe) is a vital nutrient for nearly all organisms, as it plays a pivotal role in the synthesis of essential iron cofactors, such as heme and iron-sulfur (FeS) clusters. It is indispensable for essential biological processes, including DNA synthesis, erythropoiesis, and oxygen transport. However, excess or unbound iron can become toxic, necessitating the precise regulation of cellular iron metabolism through the coordinated processes of iron uptake, storage, utilization, and export [10, 11]. Iron is capable of accepting and donating electrons, transitioning between its ferric (Fe^{3+}) and ferrous (Fe^{2+}) states. Within cells, iron can be stored in ferritin or remain as part of the labile iron pool. The labile iron pool exhibits high chemical reactivity, as free iron reacts with hydrogen peroxide (H_2O_2) via the Fenton reaction, producing hydroxyl or hydroperoxyl radicals. These reactive radicals can target polyunsaturated fatty acids in cell membranes, leading to the formation of phospholipid peroxides and ultimately triggering ferroptosis [12, 13]. The iron metabolism is subject to regulation by the iron-responsive elements/iron regulatory proteins (IRE/IRP) system. The

IRE/IRP system modulates the cellular iron balance by regulating the expression of specific proteins (e.g., ferritin and transferrin receptor 1 (TFR1)), depending on the intracellular iron levels [14, 15].

6.1.2 Lipid metabolism

As delineated in Section **6.1**, the accumulation of phospholipid peroxides is a hallmark of ferroptosis. The lipid bilayer, a fundamental component of cellular membranes, is predominantly composed of glycerophospholipids. Glycerophospholipids are structured by a glycerol backbone, two fatty acid chains (at the *sn*-1 and *sn*-2 positions), and a head group. Their chemical diversity stems from the combination of different fatty acid chains and head groups. The *sn*-1 position is typically occupied by saturated fatty acids (SFAs) or monounsaturated fatty acids (MUFAs), while the *sn*-2 position frequently contains MUFAs or polyunsaturated fatty acids (PUFAs). Depending on the head group, glycerophospholipids are characterized into distinct classes: phosphatidylcholine (PC), phosphatidylethanolamine (PE), phosphatidylserine (PS), phosphatidylinositol (PI), and phosphatidic acid (PA). Among these, PC is the most prevalent type in mammalian cell membranes [16-18]. PUFAs are particularly prone to lipid peroxidation since the C-H bonds at the bisallylic positions are the weakest in the molecule (**Figure 1 A**). Radicals, such as peroxyl- and hydroperoxyl radicals, which are generated through the Fenton reaction (see **6.1.1**), can readily abstract these hydrogen atoms, leading to the formation of a lipid radical at the bisallylic position. Subsequent to this abstraction, molecular oxygen reacts with the lipid radical to produce a lipid peroxide and a new peroxyl radical, thereby initiating a chain reaction process. The decomposition of lipid peroxides generates additional radicals and aldehydes, such as 4-hydroxynonenal (4-HNE) (**Figure 1 B**) [19-21]. The accumulation of lipid peroxidation products has been demonstrated to impede the integrity of the plasma membrane, ultimately resulting in ferroptotic cell death [3, 22].

The susceptibility of membranes to lipid peroxidation and ferroptosis depends strongly on the lipid composition, since lipids containing PUFAs are particularly sensitive to lipid peroxidation. Certain enzymes can exert a substantial influence on the lipidome, thereby modulating the sensitivity to ferroptosis. Acyl-CoA synthetase long-chain family member 4 (ACSL4) was described in 2017 as an essential component for ferroptosis execution, as ACSL4 promotes the incorporation of PUFAs into PE lipids, resulting in a PUFA-enriched

cellular membrane and increased sensitivity to lipid peroxidation and ferroptosis [23]. Conversely, membrane-associated O-acyl transferase (MBOAT) 1 and MBOAT2 have been characterized in the context of the specific incorporation of MUFAs into PE, a process that has been demonstrated to enhance resistance to lipid peroxidation and ferroptosis [24].

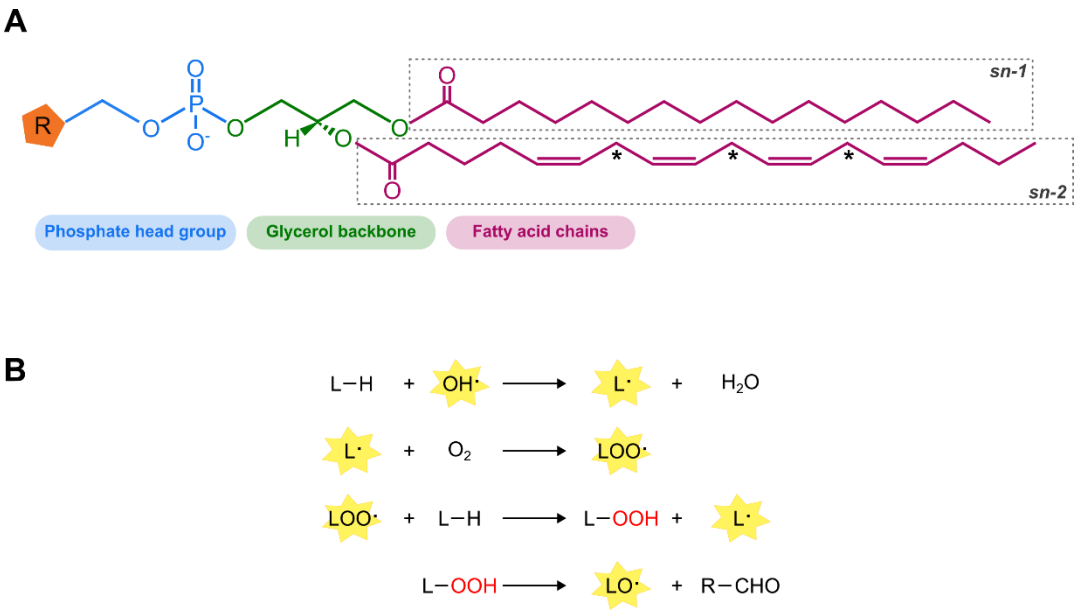

Figure 1: Glycerophospholipid structure and lipid peroxidation

(A) The classical structure of a glycerophospholipid is shown schematically. It consists of a phosphate head group (blue structure), to which a substituent (orange pentagon) is attached, which differentiates the glycerophospholipid into various subtypes. The structure is also composed of a glycerol backbone (green structure) and two fatty acid chains (purple structure). The fatty acid chain located at the *sn*-1 position is typically saturated (illustrated here), or monounsaturated. The fatty acid chain at the *sn*-2 position is predominantly monounsaturated or polyunsaturated (illustrated here). The asterisks denote the bisallylic positions. Figure adapted from [18]. **(B)** The simplified reaction of lipid peroxidation is illustrated. The process entails the oxidation of a lipid (L) by a peroxyl radical ($HO^{\cdot}$), resulting in the formation of a lipid radical ($L^{\cdot}$) and water (H_2O). Subsequently, oxygen (O_2) reacts with the lipid radical, forming a lipid peroxyl radical ($LOO^{\cdot}$). This lipid peroxyl radical can then react with other lipids, forming a lipid peroxide (L-OOH), another lipid radical, and a lipid-derived aldehyde (-CHO), resulting in a chain reaction. The yellow stars mark the radicals.

6.1.3 Enzymes protecting against ferroptosis

In addition to the molecular events that lead to ferroptosis, the presence of certain protective enzymes has been identified, suggesting the possibility of a regulated mechanism underlying this process. The protective enzymes that have been identified include glutathione peroxidase 4, the primary enzyme responsible for preventing ferroptosis, as well as ferroptosis suppressor protein 1 and system X_C^-.

6.1.3.1 Glutathione peroxidase 4

Glutathione peroxidase 4 (GPX4) plays a crucial role in the prevention of ferroptosis, as it is the only mammalian enzyme known to reduce lipid peroxides in phospholipids to their respective alcohols, even when embedded within cellular membranes [3, 25-27]. GPX4 is expressed in three distinct isoforms: cytosolic, mitochondrial, and nuclear. The cytosolic form of GPX4 is ubiquitously expressed in most tissues and cell lines, while the mitochondrial GPX4 is exclusively found in male germ cells. The nuclear GPX4 is specifically expressed in the testis, particularly in late spermatids [3, 28, 29]. Interestingly, cytosolic GPX4 is detectable in mitochondria, presumably mainly in the intermembrane space (IMS) of mitochondria [30].

The crystal structure of GPX4 reveals a monomeric protein composed of 170 amino acids, featuring four α-helices localized on the protein surface and seven β-sheets. GPX4 contains a selenocysteine at its active site (U46), which is essential for reducing lipid peroxides (**Figure 2 A**). During the reduction, the selenol group is oxidized to selenenic acid by hydroperoxides (-OOH), which is subsequently converted into a stable alcohol (-OH). To regenerate the active site, selenenic acid is reduced by glutathione (GSH), resulting in the formation of selenadisulfide and water (H_2O). In the final reduction step of the catalytic cycle, GSH reduces the selenadisulfide back to selenol, producing glutathione disulfide (GSSG) and resetting GPX4 for the next cycle (**Figure 2 B**) [29, 31].

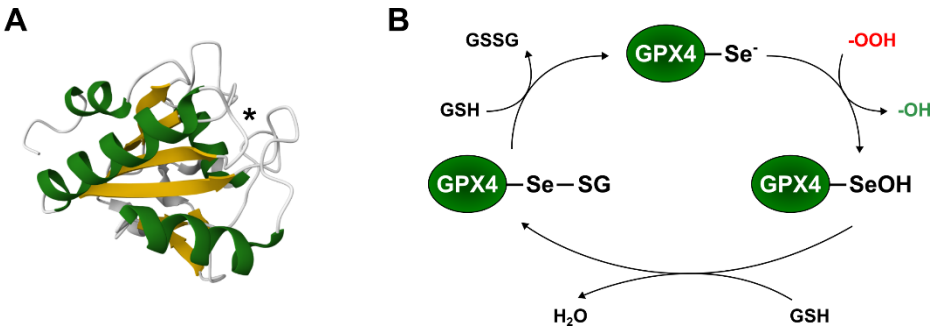

Figure 2: Glutathione peroxidase 4 and its catalytic cycle

(A) The three-dimensional structure of human glutathione peroxidase 4 (GPX4) is illustrated, with the four α-helices depicted in green, and the seven ß-sheets displayed in yellow. The asterisk indicates the active site (RCSB PDB number: 6ELW). **(B)** The diagram shows the catalytic cycle of GPX4. The selenol group ($-Se^-$) at the active site is oxidized to selenenic acid (-SeOH) by converting hydroperoxides (-OOH) to their corresponding alcohols (-OH). Selenenic acid is reduced by glutathione (GSH), leading to the formation of selenadisulfide (-Se-SG) and water (H_2O). GSH reduces selenadisulfide back to selenol, thereby producing glutathione disulfide (GSSG). Figure adapted from [29].

6.1.3.2 Ferroptosis suppressor protein 1

Ferroptosis suppressor protein 1 (FSP1) is a critical regulator of ferroptosis that functions independently of GPX4 [32, 33]. The expression of FSP1 is not restricted to specific cell organelles, but its localization to the plasma membrane is sufficient to effectively suppress ferroptosis [3, 32]. This localization shift is enabled by myristoylation at the N-terminus of FSP1. Once associated with the membrane, FSP1 contributes to the generation of lipophilic radical trapping agents that scavenge lipid peroxyl radicals, thereby preventing the propagation of lipid peroxides [3, 34]. The identified substrates of FSP1 encompass coenzyme Q_{10} and vitamin K, both known to suppress ferroptosis by interrupting lipid peroxidation chain reactions [32, 35]. Another substrate for FSP1 is the radical trapping agent vitamin E, which comprises eight natural forms: α-, β-, γ-, and δ-tocopherol and α-, β-, γ-, and δ-tocotrienol [34, 36]. These compounds have been shown to effectively interrupt the oxidation chain reaction. Since the 1980s, research has demonstrated that vitamin E exhibits a protective effect against cell death induced by cystine deprivation [37]. This process is now recognized as ferroptosis [3].

6.1.3.3 System X_C^-

GSH is the most abundant intracellular antioxidant and serves, for example, as a substrate for GPX4 in its catalytic cycle during the reduction of lipid peroxides (see **6.1.3.1** and **Figure 2 B**). GSH, a tripeptide composed of glutamic acid, cysteine, and glycine, is synthesized in a two-step process by γ-glutamylcysteine ligase (γ-GCL) and glutathione synthase (GSS) [3, 38]. The availability of cysteine is the rate-limiting factor in this process, as reduced cysteine levels lead to GSH depletion, ultimately promoting ferroptosis. A pivotal regulator of intracellular GSH levels is the amino acid antiporter system X_C^-, which facilitates cystine import in exchange for glutamate. Subsequent to its intracellular import, cystine is reduced to cysteine, which is then used for GSH biosynthesis [39, 40]. System X_C^- has emerged as a target for the development of ferroptosis-inducing agents. Next to elevating the level of extracellular glutamate, the small molecule erastin has been demonstrated to inhibit system X_C^-, resulting in the depletion of intracellular GSH and the subsequent induction of ferroptosis [40, 41].

6.1.4 Ferroptosis in diseases

Hallmarks of ferroptotic cell death are intracellular GSH depletion, reduced activity and expression levels of GPX4, as well as high levels of free iron and hydroxyl radicals. These features have been observed in various disease pathologies. This subchapter briefly describes the relationship between ferroptosis and the diseases relevant to this work, focusing on ischemia/reperfusion injury, inflammation, and degeneration.

6.1.4.1 Ischemia/reperfusion injury

Ischemia/reperfusion injury (I/R injury, IRI) is a complex and prevalent pathophysiological process that occurs when blood flow to a tissue is first interrupted (ischemia) and then restored (reperfusion). This process has the potential to affect multiple organs, resulting in substantial tissue injury [3, 42]. A paradigmatic example is a stroke, when blood clots obstruct the blood flow to downstream areas of the brain [43]. While the restoration of oxygenation is imperative for the delivery of nutrients to the tissue and its subsequent survival, reperfusion is frequently accompanied by the generation of superoxide, which can further react to form H_2O_2 [44, 45]. This, in turn, can generate hydroxyl radicals via the Fenton reaction (see **6.1.1**). Although research on IRI and ferroptosis is still limited, inhibitors of ferroptosis have been shown to have a protective effect against IRI [46, 47].

6.1.4.2 Inflammation

Recent findings suggest a potential role for ferroptosis in the pathogenesis of various chronic inflammatory conditions, including non-alcoholic steatohepatitis, chronic kidney disease, inflammation-induced neurodegeneration, and cancer [3].

A prominent example of inflammation-associated neurodegeneration is multiple sclerosis (MS), an autoimmune disorder characterized by chronic inflammation, demyelination, and the loss of oligodendrocytes [48]. Notably, reduced levels of GPX4 have been observed in neurons from the brains of MS patients, suggesting a potential link between impaired ferroptosis defense and disease progression [49]. This hypothesis is further substantiated by studies demonstrating elevated iron accumulation and increased levels of oxidized phospholipids in the brains and spinal cords of MS patients and in mice with experimental autoimmune encephalomyelitis (EAE), a widely accepted animal model of MS [50, 51].

Other examples include osteoarthritis (OA) and rheumatoid arthritis (RA), which are chronic inflammatory diseases characterized primarily by progressive cartilage degradation. Recent studies have identified key features of ferroptosis in OA, including increased iron accumulation, elevated lipid peroxidation, and reduced expression of GPX4 in cartilage tissue from OA patients [52-54]. In the context of RA, disturbances in iron metabolism have been documented, marked by reduced levels of ferritin and transferrin, along with systemic iron deficiency [55, 56].

6.1.4.3 Neurodegeneration

Neurodegenerative disorders such as Alzheimer's disease (AD) and Parkinson's disease (PD) represent a major global health burden. Although these diseases are distinct, they share common features, notably iron accumulation, oxidative stress, and progressive neuronal loss. These overlapping features raise ferroptosis as a potential common mechanism contributing to neurodegeneration [3].

In AD, increased iron levels in the brain have been associated with faster cognitive decline and more severe neurodegeneration [57, 58]. This is associated with decreased GSH levels and increased lipid peroxidation [59, 60]. In PD, iron accumulation in the substantia nigra is a well-known finding and correlates with disease severity [61]. A shift from ferrous to

ferric iron, increased ferritin levels and decreased GSH levels in this brain region may further sensitize neurons to ferroptosis [3, 62].

In summary, the evidence for ferroptosis in diseases, as well as the lack of knowledge about the physiological regulatory mechanisms of this cell death, underlines the importance of research in this area.

6.2 Redox regulation

Cells are capable of receiving and responding to distinct signals and environmental changes. The transmission of signals is facilitated by diverse signaling pathways. A notable example is the redox regulation pathway, which involves the transfer of electrons and subsequent posttranslational modifications of cysteine residues [63]. The specific modifications resulting from this process are contingent upon the prevailing second messenger in the environment. These modification may include the formation of inter- or intramolecular disulfide bridges, glutathionylation through the formation of a disulfide with GSH, nitrosation in the presence of nitric oxide (NO), the formation of sulfenic acid mediated by H_2O_2, or the formation of sulfhydration by hydrogen sulfide (H_2S). All these modifications have the capacity to reversibly influence proteins in terms of their structure, localization, and/or activity [63, 64].

Proteins belonging to the thioredoxin (Trx) family have been identified as being essential components of redox regulation. These proteins are classified as conserved oxidoreductases, possessing the capacity to either form or reduce posttranslational modifications. A common structural motif characterizes these proteins, featuring a central, four-stranded, anti-parallel β-sheet surrounded by three α-helices. A Cys-x-x-Cys motif is found at the catalytic center of these proteins, and it is imperative for their oxidoreducase function (**Figure 3 A**) [64, 65]. The Trx family encompasses a diverse array of proteins, including Trxs, Peroxiredoxins (Prxs), GPXs, and Glutaredoxins (Grxs), and is predominantly nicotinamide adenine dinucleotide phosphate- (NADPH) and GSH-dependent [63, 64].

6.2.1 Glutaredoxins

The classification of Grxs is determined by their catalytic motif, which can be either dithiol (Cys-x-x-Cys) or monothiol (Cys-x-x-Ser). The presence of four distinct Grxs has been identified in mammals [64]. Grx1 and Grx2, classified as dithiol Grxs, are present in the cytosol, with Grx2 exhibiting different isoforms. Grx2a is a mitochondrial protein, while Grx2b and Grx2c are localized both in the cytosol and in the nucleus [64, 66, 67]. Grx1 carries the active site Cys-Pro-Tyr-Cys, while the active site of Grx2 is a Cys-Ser-Tyr-Cys motif. In contrast to Grx1 and Grx2, the monothiol glutaredoxins 3 and 5 do not exhibit an oxidoreductase activity but have functions in iron homeostasis [68-70].

6.2.1.1 Glutaredoxin 2

Alongside Grx1, Grx2 possesses the capacity to reduce disulfides and glutathionylation via a distinct reaction system, the GSH-system [68, 71-73]. The primary electron donor in this system is NADPH, and the electrons are transferred to glutathione reductase (GR). The reduced GR reduces GSSG, resulting in its reduction to two GSH molecules, and GSH transfers the electrons to Grx, which can then reduce the mentioned cysteine modifications (**Figure 3 B**) [64, 72].

Additionally, Grx2 was identified as the first FeS cluster-coordinating protein of the Trx family. Two Grx2 monomers can bind a FeS cluster, forming a Grx2 dimer. This cluster is coordinated using the active site cyteines and two GSH molecules. The catalytic motif is thereby blocked, and the oxidoreductase function of the protein is prevented [74, 75]. However, at elevated levels of hydroxyl radicals or low concentrations of GSH, the FeS cluster disintegrates and Grx2 reactivates its oxidoreductase function, making Grx2 a promising redox sensor [74, 75].

The physiological relevance of Grx2 has been demonstrated in several disease contexts. In 2017, for instance, it was demonstrated that Grx2 can protect oligodendrocytes against damage triggered by nitric oxide released by activated microglia [76]. The presence of activated microglia and their secretion of nitric oxide is a hallmark of MS, contributing to the persistent neuroinflammation that characterizes this disease [77].

Another example of a disease that has been linked to Grx2 is metabolic dysfunction-associated fatty liver disease (MASLD). In 2022, it was demonstrated that the absence of Grx2 can lead to the induction of the disease in mice, characterized by lipid accumulation in the liver and hepatocyte cell death [78].

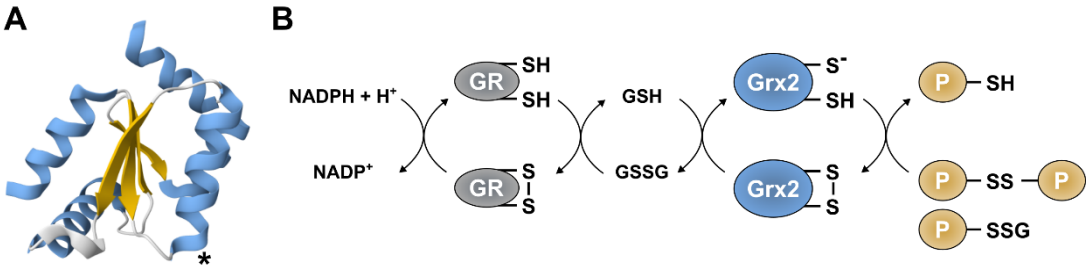

Figure 3: Glutaredoxin 2 and the glutathione system

(A) The figure presents the structural organization of glutaredoxin 2 (Grx2), with α-helices shown in blue and the β-sheets represented in yellow. The asterisk indicates the position of the catalytic Cys-Ser-Tyr-Cys motif (RCSB PDB number 2FLS). **(B)** The scheme illustrates the glutathione system with Grx2. NADPH + H^+ functions as an electron donor, reducing glutathione reductase (GR). Reduced GR has the capacity to reduce glutathione disulfide (GSSG) to glutathione (GSH). Grx2 is reduced by GSH, thereby activating its ability of Grx2 to reduce posttranslational cysteine modifications on proteins (P), such as disulfide bridges (-SS-) and glutathionylation (-SSG). Figure adapted from [64].

7 Aims of the thesis

Ferroptosis, a form of regulated necrosis, has recently garnered significant attention in the research community. The hallmarks of this form of cell death have been implicated in various diseases and represents a potential target for cancer therapies. However, the regulatory pathways and underlying mechanisms of ferroptosis remain elusive.

In previous studies of our research group, there are first indications that glutathione peroxidase 4 (GPX4) is a substrate for glutaredoxin 2 (Grx2), which emphasizes the central role of redox regulation in ferroptosis, especially through the possible posttranslational cysteine modifications.

This thesis aims to identify and evaluate novel regulatory pathways of ferroptosis, with a particular emphasis on redox regulation. Moreover, this study explores the potential of ferroptosis as a therapeutic target for various diseases.

Specific aims of this thesis are:

- Investigating regulatory pathways of ferroptosis through reversible posttranslational redox modifications
- Identification of the responsible oxidoreductases regulating ferroptosis
- Examine possible protective effects of diroximel fumarate, a drug against multiple sclerosis, in the context of ferroptosis

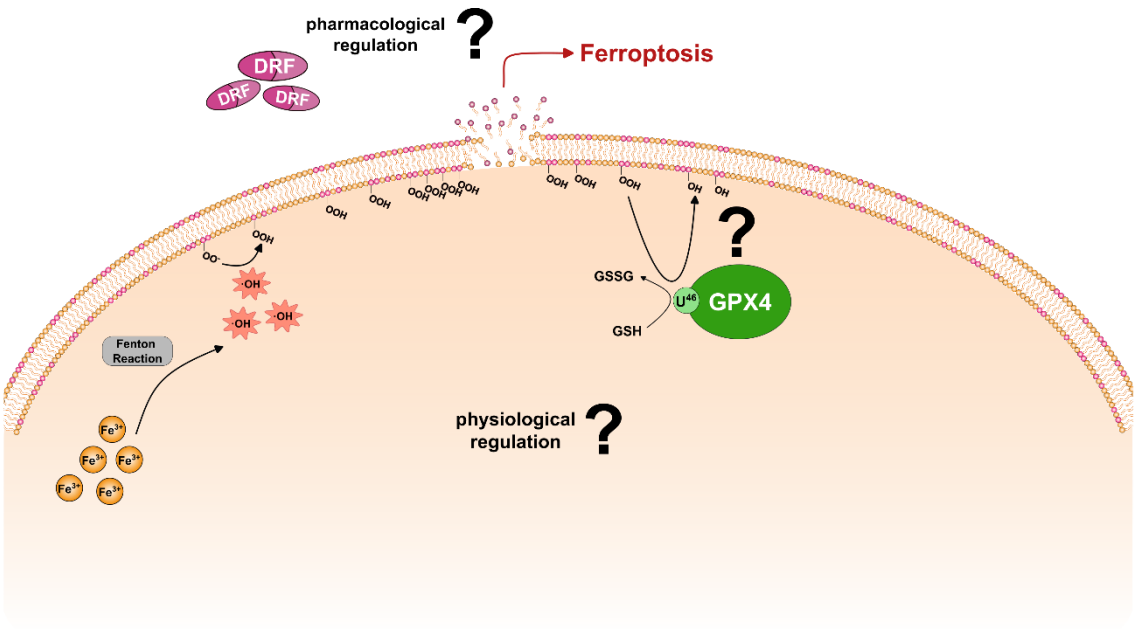

Figure 4: Graphical illustration of the aims of this work

Ferroptosis is an iron-depenend cell death which is based on the accumulation of lipid peroxides (-OOH) triggered e.g. by hydroxyl radicals (·OH). These lipid peroxides compromise membrane integrity and ultimately lead to ferroptotic cell death. The enzyme GPX4 counteracts this process by reducing lipid peroxides to non-toxic lipid alcohols (-OH), thereby protecting cells from ferroptosis. However, it remains unclear how ferroptosis is regulated under physiological and pharmacological conditions, which post-translational modifications may be involved, and what role specific oxidoreductases play.

8 Material and Methods

8.1 Material

8.1.1 Cell lines

Table 1: Cell lines

Cell line	Characteristics	Reference
MEF GPX4 WT	Mouse embryonic fibroblasts, flag- and biotin-tagged wild-type GPX4	Marcus Conrad, Munich, Germany
MEF GPX4 C75S	Mouse embryonic fibroblasts, flag- and biotin-tagged GPX4 C75S	Marcus Conrad, Munich, Germany
MEF GPX4 C75E	Mouse embryonic fibroblasts, flag- and biotin-tagged GPX4 C75E	Marcus Conrad, Munich, Germany
MEF Grx2 WT	Mouse embryonic fibroblasts	Marcus Conrad, Munich, Germany
MEF $Grx2^{-/-}$	Mouse embryonic fibroblasts lacking Grx2	Marcus Conrad, Munich, Germany
MEF Grx1 WT	Mouse embryonic fibroblasts	Yvonne Janssen-Heininger, Vermont, USA
MEF $Grx1^{-/-}$	Mouse embryonic fibroblasts lacking Grx1	Yvonne Janssen-Heininger, Vermont, USA
HeLa WT	Human endothelial cells from cervical carcinoma	Arne Holmgren, Stockholm, Sweden and [79]
HeLa Grx2a OE	Human endothelial cells from cervical carcinoma, overexpressing Grx2a	Arne Holmgren, Stockholm, Sweden and [79]
HeLa Grx2c OE	Human endothelial cells from cervical carcinoma, overexpressing Grx2c	Arne Holmgren, Stockholm, Sweden and [79]
OASF	Human synovial fibroblasts from osteoarthritis patients	Torsten Lowin, Düsseldorf, Germany
RASF	Human synovial fibroblasts from rheumatoid arthritis patients	Torsten Lowin, Düsseldorf, Germany

8.1.2 Cell culture reagents and supplements

Table 2: Cell culture reagents and supplements

Reagent	Reference
Dulbecco's modified Eagle's medium, 1.0 g/L glucose	Gibco, Thermo Fisher Scientific, USA
Dulbecco's modified Eagle's medium, 4.5 g/L glucose	Gibco, Thermo Fisher Scientific, USA
Fetal calf serum	Gibco, Thermo Fisher Scientific, USA
GlutaMAX	Gibco, Thermo Fisher Scientific, USA
Human TNFα	PeproTech, Thermo Fisher Scientific, USA
Penicillin/Streptomycin	Gibco, Thermo Fisher Scientific, USA
Roswell Park Memorial Institute 1640 medium	Gibco, Thermo Fisher Scientific, USA
Trypsin-EDTA	Gibco, Thermo Fisher Scientific, USA

8.1.3 Mouse strains

The breeding of the mice was conducted at the animal facility of the Heinrich-Heine-University of Düsseldorf (Zentrale Einrichtung für Tierversuche und Tierschutzaufgaben; ZETT). The conditions were maintained under pathogen-free conditions, with a 12-hour light/dark cycle, and the mice had access to pelletized dry food and germ-free water.

Table 3: Mouse strains

Mouse strain	Characteristics	Reference
C57BL/6	Laboratory mouse, wild-type	Orhan Aktas, Düsseldorf, Germany
$Grx2^{-/-}$	Laboratory mouse, lacking Grx2	Marcus Conrad, Munich, Germany

8.1.4 Antibodies

Table 4: Primary antibodies

Primary antibodies	Host	Reference
4-Hydroxynonenal	Rabbit	Bioss, USA
Glutaredoxin 1	Rabbit	Abcam, UK
Glutaredoxin 2	Rabbit	Abcam, UK
Glutathione peroxidase 4	Rabbit	Abcam, UK
Parvalbumin	Chicken	Antibodies.com, UK
β-actin	Mouse	Sigma-Aldrich, USA

Table 5: Secondary antibodies and detection agents

Name	Host	Reference
Chicken - HRP	Goat	Invitrogen, Thermo Fisher Scientific, USA
Fluorescent GSSG	-	Lucia Coppo, Stockholm, Sweden
Mouse - IRDye® 680RD	Goat	LI-COR Environmental, USA
Mouse - IRDye® 800CW	Goat	LI-COR Environmental, USA
Rabbit - HRP	Goat	Jackson ImmunoResearch, USA
Rabbit - IRDye® 680RD	Goat	LI-COR Environmental, USA
Rabbit - IRDye® 800CW	Goat	LI-COR Environmental, USA
Streptavidin - IRDye® 680RD	-	LI-COR Environmental, USA

8.1.5 Kits and assays

Table 6: Kits and assays

Name	Reference
3,3´- diaminobenzidine and chromogen solution	Agilent, USA
BC Assay Quantification Kit	Interchim, France
BODIPY 581/591 C11	Invitrogen, Thermo Fisher Scientific, USA
CellTiter-Blue®	Promega, USA
Nanodisc	Manuel Etzkorn, Düsseldorf, Germany
Negatively charged POPG lipids	Manuel Etzkorn, Düsseldorf, Germany
peqGOLD Protein-Marker IV	VWR Life Science, USA
Pierce™ 660 nm Protein-Assay kit	Thermo Fisher Scientific, USA
PowerUP SYBR Green Master Mix	Thermo Fisher Scientific, USA
Reverse Transcription Kit	Thermo Fisher Scientific, USA
TRIzol Reagent	Thermo Fisher Scientific, USA

8.1.6 Chemicals

Table 7: Chemicals

Name	Reference
Acetic acid	Merck, Germany
Acetone	Merck, Germany
Anti-FLAG® M2 magnetic beads	Sigma-Aldrich, USA
BioGEE	Invitrogen, Thermo Fisher Scientific, USA
Bovine serum albumin	Roth, Germany
CHAPS	Amersham Bioscience, UK
Coomassie brilliant blue	Roth, Germany
Cumene hydroperoxide	Sigma-Aldrich, USA
Dimethyl sulfoxide	Roth, Germany

Dipotassium hydrogen phosphate	Sigma-Aldrich, USA
Entellan™ new	Sigma-Aldrich, USA
Erastin	Sigma-Aldrich, USA
Ethanol	Merck, Germany
Ethylenediaminetetraacetic acid	Sigma-Aldrich, USA
EveryBlot blocking buffer	Bio-Rad, USA
Fluorescent GSSG	Lucia Coppo, Stockholm, Sweden
Formic acid	Sigma-Aldrich, USA
Glucose	Sigma-Aldrich, USA
Glutathione	Sigma-Aldrich, USA
Glycine	Sigma-Aldrich, USA
HEPES	Life Technologies, USA
Laemmli protein sample buffer	Bio-Rad, USA
Liproxstatin-1	Sigma-Aldrich, USA
Mayer's hematoxylin solution	Merck, Germany
Methanol	VWR Chemicals, Avantor, USA
N-Ethylmaleimide	Sigma-Aldrich, USA
Nicotinamide adenine dinucleotide phosphate	Sigma-Aldrich, USA
Nonidet P-40	Fluka, Fisher Scientific, USA
Normal goat serum	Fisher Scientific, USA
Paraformaldehyde	Roth, Germany
Phosphate-buffered saline	Gibco, Thermo Fisher Scientific, USA
Phosphatidylcholine hydro peroxide	Marcus Conrad, Munich, Germany
Potassium chloride	Sigma-Aldrich, USA
Potassium dihydrogen phosphate	Sigma-Aldrich, USA
Protease inhibitor	Roche, Switzerland
Sodium acetate	Fluka, Fisher Scientific, USA
Sodium chloride	Sigma-Aldrich, USA
Sodium dodecyl sulfate	Roth, Germany
Sodium hydrogen phosphate	Sigma-Aldrich, USA

Sodium phosphate	Sigma-Aldrich, USA
Tris	Roth, Germany
Tris hydrochloride	Roth, Germany
Triton X-100	Sigma-Aldrich, USA
Tween	Sigma-Aldrich, USA
Xylene (Roti®Histol)	Roth, Germany
β-(4-hydroxyphenyl)ethyl iodoacetamide	Sigma-Aldrich, USA
β-mercaptoethanol	Gibco, Thermo Fisher Scientific, USA

8.1.7 Proteins

Table 8: Proteins

Name	Reference
Glutaredoxin 2	Carsten Berndt, Düsseldorf, Germany
Glutathione reductase	Sigma-Aldrich, USA

8.1.8 Primer

Table 9: Primer

Target gene	Sequence	Reference
Ferritin	FW: GCCATCAACCGCCAGATC RV: TCATGAGATTGGTGAAGAAAGTATTTG	Eurofins Genomics, Germany
GAPDH	no published sequence available	GeneGlobe ID: QT00079247 Qiagen, Germany
Glutathione peroxidase 4	FW: CCGATACGCTGAGTGTGGTT RV: TCACCACGCGAGCCGTTCT	Eurofins Genomics, Germany
Heme oxygenase	FW: GCCGAGAATGCTGAGTTCATG RV: TGCAGCTCCTCAGGGAAGTAGA	Eurofins Genomics, Germany

8.1.9 siRNA

Table 10: siRNA

Name	Target protein	Sequence	Reference
siCtrl	None, control	5‘ CUGAUGACCUGAGUGAAU 3‘ 5‘ CAUUCACUCAGGUCAUCA 3‘	Eurogentec, Belgium
siGrx1	Glutaredoxin 1	5‘ CGACAAAUUCCAGAAGCCC 3‘ 5‘ GGGCUUCUGGAAUUUGUCG 3‘	Eurogentec, Belgium
siGrx2	Glutaredoxin 2	5‘ UAUGAGUGUCAGUUGCAC 3‘ 5‘ GGUGCAACUGACACUCAU 3‘	Eurogentec, Belgium

8.1.10 Equipment

Table 11: Equipment

Device	Reference
Automatic Cell Counter TL10	Bio-Rad, USA
BD FACS Canto II	BD Bioscience, USA
Biosensor high precision streptavidin Octet® SAX	Sartorius AG, Germany
BLItz™ instrument	FortéBio, USA
BZ-X810 microscope	Keyence, Japan
Centrifuge 5417R	Eppendorf, Germany
Centrifuge 5418	Eppendorf, Germany
ChemiDoc Imaging System	Bio-Rad, USA
CLARIOstar Plus Plate Reader	BMG Labtech, Germany
Cryostat	Leica, Germany
DynaMag™-2 Magnet	Thermo Fisher Scientific, USA
Electroporator Gemini SC	BTX, USA
HERAcell 150i Incubator	Thermo Fisher Scientific, USA
Megafuge	Thermo Fisher Scientific, USA
Mini-PROTEAN® Tetra System	Bio-Rad, USA
Mini-PROTEAN® TGX™ Precast Gel	Bio-Rad, USA
Nanodrop 2000 Spectrophotometer	Thermo Fisher Scientific, USA
pH-Meter HI221	Hanna Instruments, Germany

QuantStudio 3	Thermo Fisher Scientific, USA
Sonopuls UW 2070	Bandelin electronic, Germany
Standard Power Pack P25T	Biometra, Germany
Thermocycler T Gradient	Biometra, Germany
Trans-Blot® Turbo™ Transfer System	Bio-Rad, USA
UV/Vis-Spektrometer/Photometer UV-1800	Shimadzu, Japan
Vibratome 7000smz-2	Campden Instruments, UK

8.1.11 Software

Table 12: Software

Name	Provider
DeepL	DeepL SE, Germany
Endnote	Clarivate, USA
FlowJo	BD Bioscience, USA
GraphPad Prism 9	GraphPad Software, USA
Image Lab	Bio-Rad, USA
ImageJ	Open Source (GNU General Public License)
Inkscape	Open Source (GNU General Public License)
MARS	BMG Labtech, Germany
Microsoft Office	Microsoft Corporation, USA

8.2 Methods

8.2.1 Cell culture

Mouse embryonic fibroblast (MEF) cell lines were generated and provided by Marcus Conrad at the Helmholtz Center Munich and Yvonne Janssen-Heininger from University of Vermont. MEFs were cultured in Dulbecco's modified Eagle's medium (DMEM) containing 4.5 g/L glucose, 10 % fetal calf serum (FCS), and 1 % penicillin/streptomycin. HeLa cells (human endothelial cells derived from cervical carcinoma) were cultured in DMEM containing 1.0 g/L glucose, 10 % FCS, and 1 % penicillin/streptomycin.
The osteoarthritis synovial fibroblast (OASF) and rheumatoid arthritis synovial fibroblast (RASF) cells were provided by Torsten Lowin from the University Clinic Düsseldorf. These cells are derived from patients suffering from osteoarthritis (OA) or rheumatoid arthritis (RA), and were extracted from the knee joint capsule. The cells were cultivated in Roswell Park Memorial Institute (RPMI) 1640 medium, which contained 10 % FCS, 1 % penicillin/streptavidin, and 1 % GlutaMAX.
All cells were maintained at 37 °C in a humidified atmosphere containing 5 % CO_2.

8.2.2 Electroporation

The transfection method of electroporation was used to transfer siRNA into HeLa cells. For this purpose, 3.5 x 10^6 cells together with 15 µg siRNA were transferred into 500 µl electroporation buffer (*21 mM HEPES, 137 mM NaCl, 5 mM KCl, 0.7 mM Na_2HPO_4, 6 mM Glucose, pH 7.15*) and electroporated at 250 V and 1500 µF for 23-25 ms using the electroporator Gemini SC (BTX, USA). This temporarily increases the permeability of the cell membrane, allowing siRNA to enter the cell. After electroporation, 500 µL of FCS was added directly to the cells and the solution was transferred to a 75 cm^2 cell culture flask together with 9 ml of medium. The entire procedure was repeated after 72 hours, and after an additional 24 hours, the cells were harvested and used for further experiments.

8.2.3 Cell viability assay

Cell viability was measured in a 96-well plate containing 1 x 10^4 cells per well. The cells were treated with increasing concentrations of erastin (Sigma-Aldrich, USA) or cumene hydroperoxide (Sigma-Aldrich, USA) for 24 hours to induce ferroptosis and co-treated with or without 100 nM Liproxstatin-1 (Sigma-Aldrich, USA) to inhibit ferroptosis. Following

this, the cells were incubated with CellTiter-Blue® reagent (Promega, USA), diluted in a 1:6 ratio in culture medium, for 1 hour at 37 °C and 5 % CO_2. Fluorescence (545/600 nm) was measured using the CLARIOstar plus plate reader (BMG Labtech, Germany).

8.2.4 Detection of lipid peroxidation

A total of 2 x 10^5 cells per well were seeded in a 6-well plate and treated with 10 µM erastin or 32 µM cumene hydroperoxide for 6 hours at 37 °C and 5 % CO_2 to induce lipid peroxidation. Following this, the cells were washed with phosphate-buffered saline (PBS), and lipid peroxidation was stained using 1 µM BODIPY 581/591 C11 for 15 minutes at 37 °C and 5 % CO_2. Subsequent to this, the cells were washed with PBS and trypsinized. The cell suspension was centrifuged at 700 g for 10 min and the pellet was resuspended in 300 µl of PBS, which contained 0.5 % bovine serum albumin (BSA) and 2 mM ethylenediaminetetraacetic acid (EDTA). Flow cytometry analysis was subsequently performed using the BD FACS Canto II. After establishing the cell gate (FSC-A/SSC-A), FSC-A and FSC-H were utilized for doublet discrimination. The signals from oxidized BODIPY were measured in the FITC detector channels (excitation laser 488 nm; 530/30 bandpass filter).

Data analysis was performed using the FlowJo Software.

8.2.5 Immunoprecipitation of GPX4

The isolation of flag-tagged GPX4 from MEFs was conducted through immunoprecipitation. To this end, MEFs were lysed with NP40 lysis buffer *(150 mM NaCl, 50 mM Tris-HCl, 1 % NP-40, pH 8.0)*, and the lysate was subsequently centrifuged for 10 minutes at 10000 g and 4 °C. The resultant clear supernatant was collected and incubated with 25 µl of Anti-FLAG® M2 magnetic beads (Sigma-Aldrich, USA) in 2 ml of IP buffer *(150 mM NaCl, 50 mM Tris-HCl, 2 % protease inhibitor, pH 7.4)* for 2 hours at 4 °C. Thereafter, the beads were washed thrice with wash buffer *(150 mM NaCl, 50 mM Tris-HCl, 2 % protease inhibitor, 0.1 % NP40, pH 7.4)*. The elution of GPX4 was achieved through incubation of the beads at 95 °C for 5 minutes.

8.2.6 Detection of glutathionylated GPX4

A vial (100 µg) of the glutathionylation detection reagent BioGEE (Invitrogen, USA) was diluted in 700 µl culture medium. MEFs were resuspended in BioGEE for 1 hour at 37 °C

and 5 % CO_2. Following this, the MEFs were divided into two cell culture flasks and treated with ferroptosis-inducing reagents or a vehicle control for 6 hours at 37 °C and 5 % CO_2. MEFs were washed twice with PBS containing 100 mM N-ethylmaleimide (NEM), trypsinized and centrifuged at 1000 g for 10 minutes. The cells were lysed in NP40 lysis buffer *(150 mM NaCl, 50 mM Tris-HCl, 1 % NP-40, pH 8.0)* containing 100 mM NEM at -20 °C. Subsequently, immunoprecipitation of GPX4 was carried out (see **8.2.5**), and the levels of BioGEE per GPX4 were determined by western blot as described in **8.2.9**.

8.2.7 Fluorescent GSSG labeling

Immunoprecipitated GPX4 labeled to magnetic beads (see **8.2.5**) were incubated with fluorescent GSSG (provided by Lucia Coppo from the Karolinska Institute of Stockholm) for 15 minutes at 4 °C. Subsequent to this, the beads were divided into 6 new tubes and incubated with either 1 mM GSH or 1 mM GSH and 100 nM recombinant Grx2 (provided by Carsten Berndt from University Clinic Düsseldorf) at 25 °C. The reaction was stopped with 100 mM NEM after 10 seconds, 30 seconds, or 60 seconds. Thereafter, the beads were diluted in 1x Laemmli protein sample buffer (Bio-Rad, USA) and incubated for 5 minutes at 95 °C. The level of GSSG remaining on GPX4 was determined by electrophoresis (see **8.2.9**) and visualized with UV light.

8.2.8 Protein quantification

The protein levels of the extracts of lysed cells were determined by using the BC assay quantification kit (Interchim, France) according to the manufacturer's protocol.

8.2.9 Electrophoresis and western blot

Samples were diluted in 1x Laemmli protein sample buffer (Bio-Rad, USA) and subsequently incubated for 5 minutes at 95 °C. Proteins were separated by mass in the Mini-PROTEAN® TGX™ Precast Gel (Bio-Rad, USA) in the Mini-PROTEAN® Tetra System (Bio-Rad, USA) with running buffer *(25 mM Tris, 192 mM Glycine, 0.1 % SDS, pH 8.3)* for approximately 1 hour at 130 V. To visualize total protein content, the gel was incubated with coomassie staining solution *(10 % acetic acid, 40 % EtOH, 0.1 % coomassie brilliant blue)* for 1 hour and subsequently incubated overnight at 4 °C with destaining solution *(10 % acetic acid, 20 % EtOH)* to wash out unspecific stains.

To detect specific proteins, the gel was transferred to a 0.2 µm nitrocellulose membrane using the Trans-Blot® Turbo™ Transfer System (Bio-Rad, USA) for 7 minutes at 1.3 A and 25 V. The membrane was then blocked with EveryBlot blocking buffer (Bio-Rad, USA) for 10 minutes. Following this, the membrane was stained with primary antibodies overnight at 4 °C. The following day, the membrane was washed thrice with PBS containing 0.05 % Tween and incubated for 1 hour at room temperature with fluorochrome-labeled secondary antibodies. The visualization process was facilitated by the ChemiDoc Imaging System (Bio-Rad, USA). Band intensity analysis was performed using the ImageLab software.

8.2.10 GPX4 activity

Frozen cell pellets of MEF GPX4 WT, MEF GPX4 C75S and MEF GPX4 C75E were resuspended in 100 µl extraction buffer *(1 mM EDTA, 150 mM KCl, 2 mM β-mercaptoethanol, 0.1 % CHAPS in 100 mM KH_2PO_4/K_2HPO_4, pH 7.4)* and centrifuged for 2 minutes at 17000 g and 4 °C. The assessment of enzymatic activity was conducted through the incubation of 50 µl of the supernatant with 1 ml of reaction buffer *(5 mM EDTA, 5 mM GSH, 0.1 % peroxide-free Triton X-100, 0.2 mM NADPH in 100 mM KH_2PO_4/K_2HPO_4, pH 7.8)*, in conjunction with 180 IU/ml glutathione reductase (GR) and 25 µM phosphatidylcholine hydroperoxide (PCOOH). The consumption of NADPH resulting from the enzymatic activity was measured at a wavelength of 340 nm using a spectrometer (Shimadzu, Japan). For normalization, protein content was measured using a Pierce™ 660 nm Protein-Assay kit (Thermo Fisher Scientific, USA) according to the manufacturer's protocol.

8.2.11 Bio-layer interferometry measurements

In order to investigate the binding of GPX4 WT and GPX4 C75E to membranes, bio-layer interferometry (BLI) was performed. For this purpose, nanodiscs loaded with negatively charged POPG lipids were utilized. All measurements were conducted at room temperature using the BLItz™ instrument (FortéBio, USA) and the high precision streptavidin Octet® SAX biosensors (Sartorius AG, Germany).

Prior to use, the biosensor was hydrated for 20 minutes in sodium phosphate buffer *(20 mM sodium phosphate, 50 mM NaCl, pH 7.4*). Subsequently, a baseline was measured for 30 seconds. Thereafter, the lysate containing the biotin-tagged GPX4 was immobilized on the

biosensor by loading 4 µl of the lysate onto the drop holder of the BLItz^{TM} device. The loading of the protein to the sensor was measured for 300 seconds, after which the sensor was returned to the sodium phosphate buffer for a second baseline measurement. Next, 4 µl of nanodiscs were loaded onto the drop holder and the association was monitored for 180 seconds. Following this, dissociation was performed for 240 seconds by placing the sensor into a fresh tube of sodium phosphate buffer. Different dilutions of the POPG-nanodiscs were measured.

8.2.12 GSH level measurement

To quantify GSH levels in cells, it is first necessary to label free thiols with β-(4-hydroxyphenyl)ethyl iodoacetamide (HPE-IAM). For this purpose, 2 x 10^5 cells per well were seeded on a 6-well plate and cultured for 24 h under standard culture conditions (see **8.2.1**). The medium was subsequently replaced with FCS-free culture medium, and the cells were incubated for 3 h. The cells were then washed twice with PBS. For labeling, 750 µl per well of a 5 mM HPE-IAM/50 mM sodium acetate (pH 6.5) solution in 70 % methanol was added to the cells. The cells were scraped and harvested in this solution. The cell suspension was then sonicated with 3 pulses of 6 cycles and 10 % power using a Sonopuls UW 2070 apparatus (Bandelin, Germany). Following this step, the samples were incubated at 37 °C for 20 minutes. The suspension was centrifuged and 50 µl of the resultant supernatant was mixed with 100 µl of 0.1 % formic acid. The samples were stored at -80 °C and shipped to Takaaki Akaike, Department of Environmental Medicine and Molecular Toxicology, Tohoku University, Sendai, Japan, for further analysis via mass spectrometry. The remaining protein pellets were diluted in 750 µl of 0.1 % SDS in PBS, sonicated, and centrifuged again as previously described. Protein quantification was performed as described in **8.2.8**.

8.2.13 RNA isolation and cDNA synthesis

The isolation of ribonucleic acid (RNA) from cells was conducted using TRIzol Reagent (Thermo Fisher Scientific, USA) in accordance with the manufacturer's protocol. The concentration of isolated RNA was subsequently measured using the NanoDrop 2000 (Thermo Fisher Scientific, USA). Subsequently, 1.5 µg of the isolated RNA was reverse-transcribed into complementary deoxyribonucleic acid (cDNA) using the Reverse Transcription Kit (Thermo Fisher Scientific, USA). The synthesis reaction was performed

in the Biometra T Gradient Thermocycler (Analytik Jena AG, Germany) using the following settings: 25 °C for 10 minutes, 37 °C for 2 hours, and 85 °C for 5 minutes. The synthesized cDNA was subsequently diluted to a concentration of 1:3 in nuclease-free water.

8.2.14 Quantitative polymerase chain reaction

The synthesized cDNA samples (see **8.2.13**) were subjected to quantitative polymerase chain reaction (qPCR). A total of 40 ng of cDNA were combined with 100 pmol of target primer and 10 µl of PowerUP SYBR Green Master Mix (Thermo Fisher Scientific, USA). The qPCR reaction was conducted in the QuantStudio 3 (Thermo Fisher Scientific, USA) using the settings outlined in **Table 13**.

Table 13: qPCR settings

Stage	Step	Temperature	Time
Hold stage	Step 1	50 °C	2 minutes
	Step 2	95 °C	10 minutes
PCR stage (40 cycles)	Step 1	95 °C	15 seconds
	Step 2	60 °C	1 minute
Melt curve stage	Step 1	95 °C	15 seconds
	Step 2	60 °C	1 minute
	Step 3	95 °C	15 seconds

8.2.15 Immunohistochemistry

The organs of wild-type (WT) and Grx2$^{-/-}$ mice were isolated and fixated using 4 % paraformaldehyde. For the preparation of cryosections, the organs were embedded in Tissue Tek, frozen, and cut into 8 µm sections using a cryostat. The sections on microscope slides were incubated for 10 min in PBS to remove excess Tissue Tek. Afterwards, the sections were fixated for 10 minutes in acetone at -20 °C. The sections were then incubated for 1 hour in blocking solution *(10 % normal goat serum in PBS)* at room temperature. After this, the sections were stained with a 4-hydroxynonenal (4-HNE) antibody *(1:250 in blocking solution)* (Bioss, USA) overnight at 4 °C. Subsequently, the sections were washed twice with PBS and incubated with a secondary peroxidase-conjugated antibody *(1:100 in blocking solution)* (Jackson ImmunoResearch, USA) for 1 hour at room temperature.

Following this, the sections were washed twice with PBS and incubated for 3 minutes with 3,3´-diaminobenzidine and chromogen solution (Agilent, USA). The reaction was stopped by incubating the sections for 5 minutes in dH_2O. The sections were co-stained with haematoxylin for 1 second, followed by an incubation of 5 minutes under running water. They were subsequently dehydrated with alcohol *(70 % EtOH, 80 % EtOH, 96 % EtOH, and 100 % EtOH).* Following this, the sections were incubated in xylene for 3 min and subsequently preserved with Entellan.

For parvalbumin-positive neuron staining, the brains of mentioned mice were sliced into 75 µm sections using the vibratome 7000smz-2 (Campden Instruments, UK). The sections were washed twice with PBS and incubated for 1 hour in blocking buffer *(10 % normal goat serum, 0.1 % Triton in PBS)*. Following this, the sections were incubated with a parvalbumin antibody *(1:1000 in blocking solution)* at 4 °C overnight. The sections were washed twice with PBS and subsequently incubated for 30 seconds with 3,3´-diaminobenzidine and chromogen solution (Agilent, USA). The reaction was stopped by incubating the sections for 5 minutes in dH_2O. The sections were transferred to a microscopy slide and preserved using Immomount.

All samples were analyzed with the microscope BZ-X800 (Keyence, Japan).

8.2.16 Statistical analysis

Graphs and statistical analyses were generated using GraphPad Prism 9 (GraphPad Software, USA). For $n \geq 4$, data are presented as box-whisker plots. All other plots show the mean and standard error of the mean (SEM). The statistical significance level was determined using the following p-values:

Not significant: $p > 0.05$
*: $p < 0.05$
**: $p < 0.01$
***: $p < 0.001$
****: $p < 0.0001$

9 Results

9.1 Glutathionylation of GPX4

In cooperation together with Gereon Poschmann and his team at the Molecular Proteomics Laboratory at Heinrich Heine University in Düsseldorf, mass spectrometric studies of GPX4 were performed. This analysis revealed glutathionylation at cysteine 75 (C75) of GPX4 found in the tryptic peptide ILAFPCNQFGR (m/z 524.24, 3-fold charged). The glutathionylation can be identified by a shift of the present mass (+ 305.07 Da) compared to the mass of the peptide variant with the cysteine in sulfhydryl form along with respective shift of the Y6-Y8 ions in the respective fragment spectrum (**Figure 5 A**). In order to evaluate potential alterations to the protein induced by glutathionylation at C75, Yana Bodnar (AG Lillig) at the Institute for Medical Biochemistry and Molecular Biology at University Medicine Greifswald performed molecular dynamics (MD) simulations. The MD simulations revealed three distinct conformations of GSH at C75, all of which resulted in a negative charge on the electrostatic surface potential in the C75 region. In the simulation with a reduced C75, this region exhibited a predominantly positive charge. To further investigate the effects of this change, simulations were carried out with GPX4 in which C75 was exchanged for a serine (C75S), and with GPX4 in which C75 was exchanged for a glutamic acid (C75E). The GPX4 C75S mutant revealed the same electrostatic surface potential distribution as the reduced GPX4 (**Figure 5 B**). Therefore, in future experiments, this mutant will be considered as reduced GPX4 C75. The GPX4 C75E mutant displayed a comparable surface potential distribution to that of the simulated glutathionylated GPX4. Consequently, the GPX4 C75E mutant is regarded as the glutathionylated GPX4 C75 in subsequent experiments. The GPX4 mutants were generated as MEF cell lines by Marcus Conrad and his team at the Helmholtz Center in Munich and provided to us.

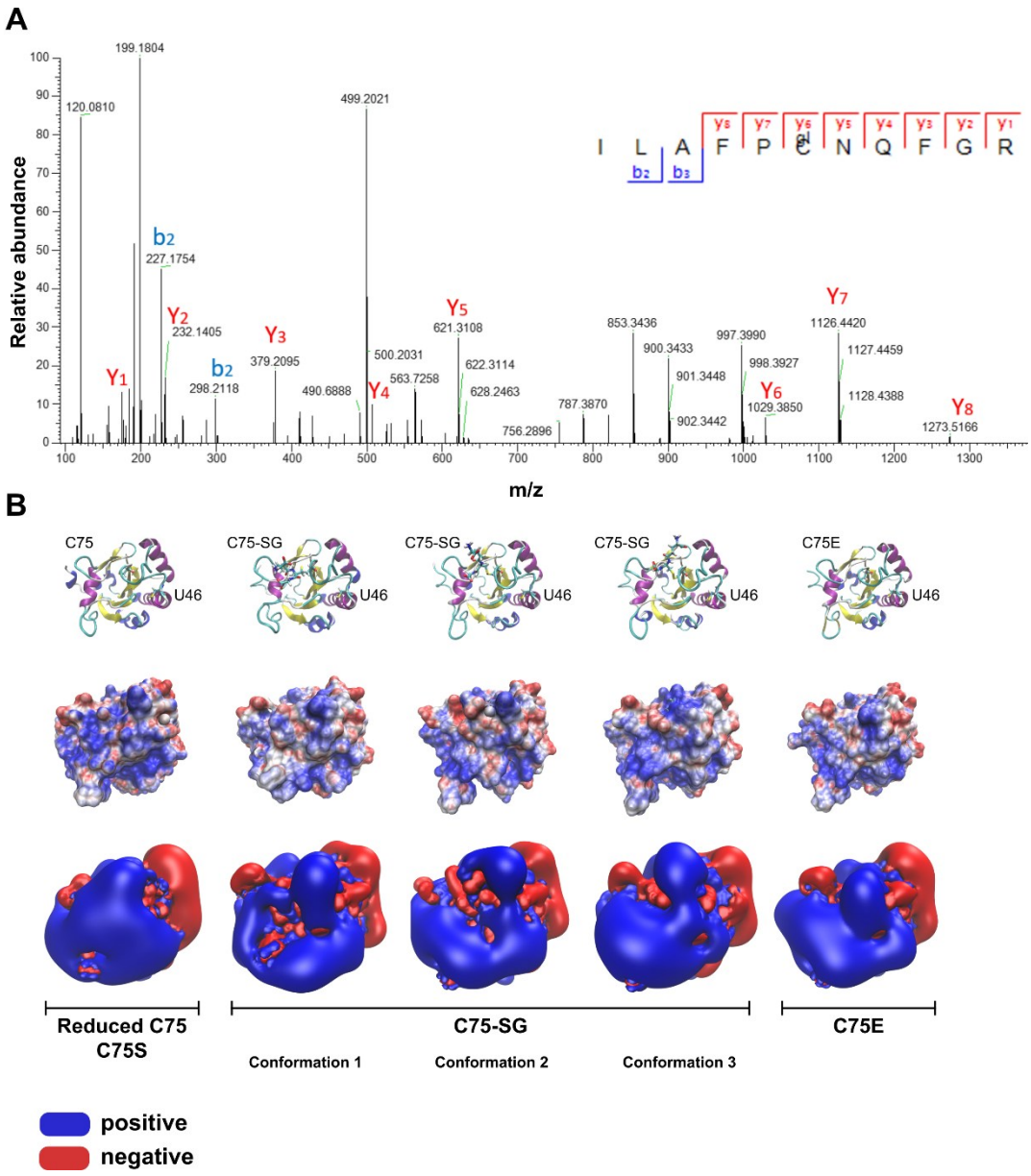

Figure 5: Glutathionylation on GPX4 C75 affects electrostatic surface potential

(A) The figure shows a fragment spectrum (parent mass m/z 524.24, 3x charged) from a mass spectrometric analysis of a tryptic digested GPX4, the parent mass and fragments support (Maxquant score 87.26) and glutathionylation at cysteine 75. The measurement and analysis were performed in cooperation together with Gereon Poschmann and his team at the Molecular Proteomics Laboratory at Heinrich Heine University in Düsseldorf. **(B)** Molecular dynamics simulations were performed by Yana Bodnar (AG Lillig) at the Institute for Medical Biochemistry and Molecular Biology at University Medicine Greifswald. The top row illustrates the structural arrangement of the protein, highlighting the approximate orientation of the active site (U46) and C75. The middle row represents the electrostatic surface potential mapped onto the protein surface (blue = positive charge, red = negative charge). The bottom row visualizes the electrostatic potential as a spatial distribution extending beyond the molecular surface. The first column (left) shows reduced GPX4 C75 or the GPX4 C75S mutant. The three middle columns display the three possible conformations of glutathione (GSH) bound at C75 (C75-SG). The last column (right) represents the GPX4 C75E variant.

9.1.1 GPX4 C75E sensitizes cells to ferroptosis

In order to investigate the influence of glutathionylation at GPX4 C75 on ferroptosis, cell viability assays were performed as outlined in **8.2.3**. Ferroptosis was induced in MEFs using erastin or cumene hydroperoxide (CHP), and the viability was measured after 24 hours. Erastin blocks the amino acid antiporter system X_C^-, resulting in decreased intracellular GSH levels and is described as a ferroptosis inducer [80, 81]. CHP serves as an organic oxidant, leading to increased oxidative stress in the cell [82]. The half-maximal inhibitory concentration (IC_{50}) values were subsequently calculated. For the erastin treatment MEF GPX4 WT demonstrated an IC_{50} of 8.2 ± 1.6 µM, while the MEF GPX4 C75S exhibited a significantly elevated viability with an IC_{50} of 22.4 ± 2.2 µM. Conversely, the viability of MEF GPX4 C75E was found to be significantly diminished with an IC_{50} of 1.2 ± 0.5 µM erastin (**Figure 6 A-B**). A parallel tendency was noted subsequent to ferroptosis induction with CHP. MEF GPX4 WT exhibited an IC_{50} of 77.5 ± 7.1 µM, while MEF GPX4 C75S demonstrated an IC_{50} of 71.4 ± 4.3 µM. In contrast, MEF GPX4 C75E exhibited a significantly reduced IC_{50} of 5.1 ± 1.0 µM CHP (**Figure 6 C-D**).

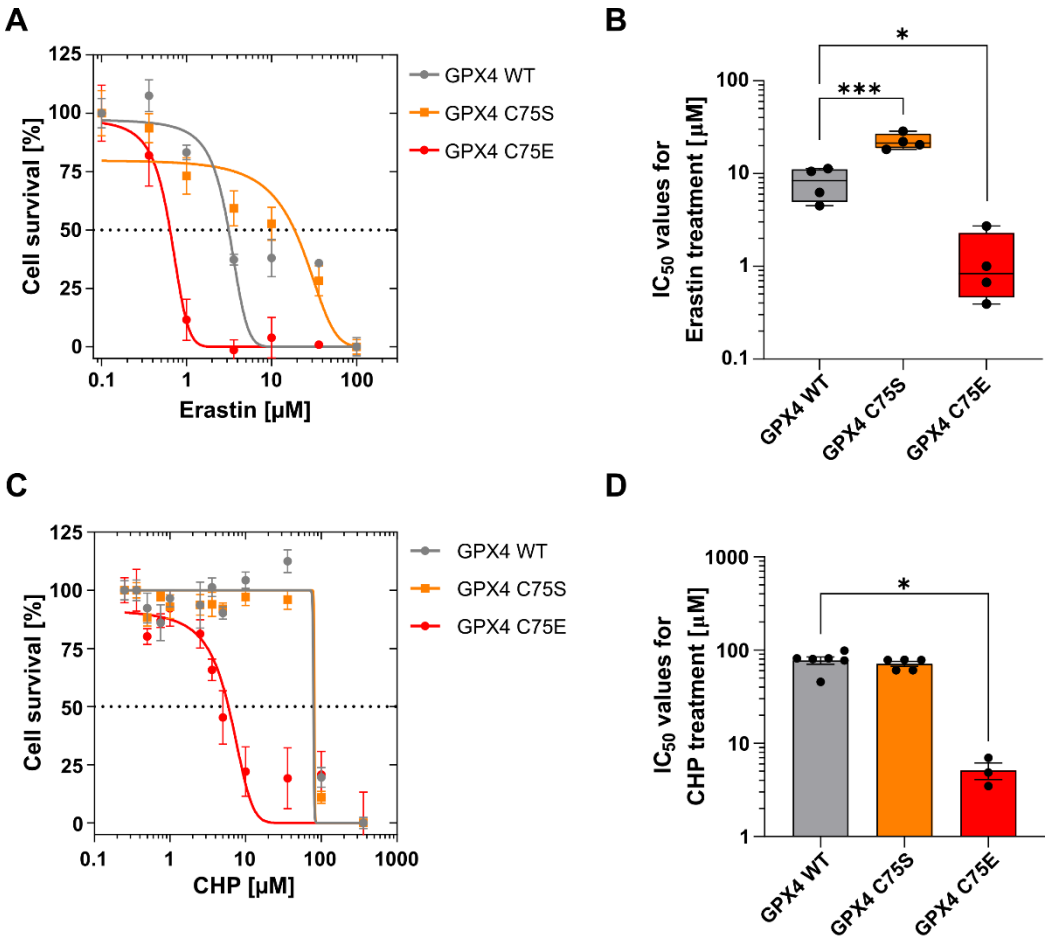

Figure 6*:* Cell viability of MEF GPX4 C75 mutants after ferroptosis induction

(A) The concentration-response curve illustrates the survival rates of MEF GPX4 WT (gray), MEF GPX4 C75S (orange), and MEF GPX4 C75E (red) subsequent to ferroptosis induction with increasing erastin concentrations (0.1 µM - 100 µM). The mean values (n = 4) and the standard error of the mean are shown. **(B)** A box-whisker plot represents the IC_{50} values derived from (A) for the three MEF cell lines. Black dots indicate individual IC_{50} values. A one-way ANOVA revealed a p-value of 0.0003 (***) for the comparison between GPX4 WT and GPX4 C75S, and a p-value of 0.0257 (*) for GPX4 WT and GPX4 C75E. **(C)** The second concentration-response curve shows the survival rates of the three cell lines in response to ferroptosis induction with increasing concentrations of cumene hydroperoxide (CHP) (0.32 µM – 320 µM). The mean values were calculated for n = 6 (WT), n = 5 (C75S), and n = 3 (C75E), along with the standard error of the mean. **(D)** A bar plot displays the IC_{50} values derived from (C), with mean values and the standard error of the mean shown. Black dots represent individual IC_{50} values. A Kruskal-Wallis test comparing GPX4 WT and GPX4 C75E yielded a p-value of 0.0115 (*). The trend lines shown in figures A and C are for illustrative purposes only and were not used in further calculations.

Given that lipid peroxidation is a hallmark of ferroptosis, the accumulation of lipid peroxides was measured using BODIPY C11 and flow cytometry analysis as outlined in **8.2.4**. In the event of lipid peroxidation, BODIPY is also oxidized and is detectable in the FITC detector channel. The induction of ferroptosis with 10 µM erastin led to an increase in oxidized BODIPY, reaching 387.3 ± 51.1 % in the GPX4 WT MEFs. In contrast, GPX4 C75S MEFs exhibited a substantially weaker oxidized BODIPY accumulation, reaching 192.2 ± 32.4 %. The accumulation of oxidized BODIPY in MEF GPX4 C75E was observed to be significantly increased to 623.7 ± 57.0 % (**Figure 7 A-B**). The findings demonstrated that the induction of ferroptosis by CHP resulted in an increase in oxidized BODIPY levels to 141.4 ± 4.9 % in GPX4 WT MEFs, as compared to their untreated control group, which was set to 100 %. GPX4 C75S MEFs exhibited an increase to 143.3 ± 4.2 %, as compared to their respective control groups. Conversely, MEF GPX4 C75E exhibited an increase in oxidized BODIPY levels to 244.1 ± 52.0 %, in comparison to their uninduced control group (**Figure 7 C-D**). In summary, the data demonstrate that following ferroptosis induction with erastin and with CHP, the highest level of oxidized BODIPY and thus the most accumulation of lipid peroxides is observed in the GPX4 C75E MEFs.

The results of these experiments indicate that glutathionylation at GPX4 C75 results in a decrease in resistance to ferroptosis.

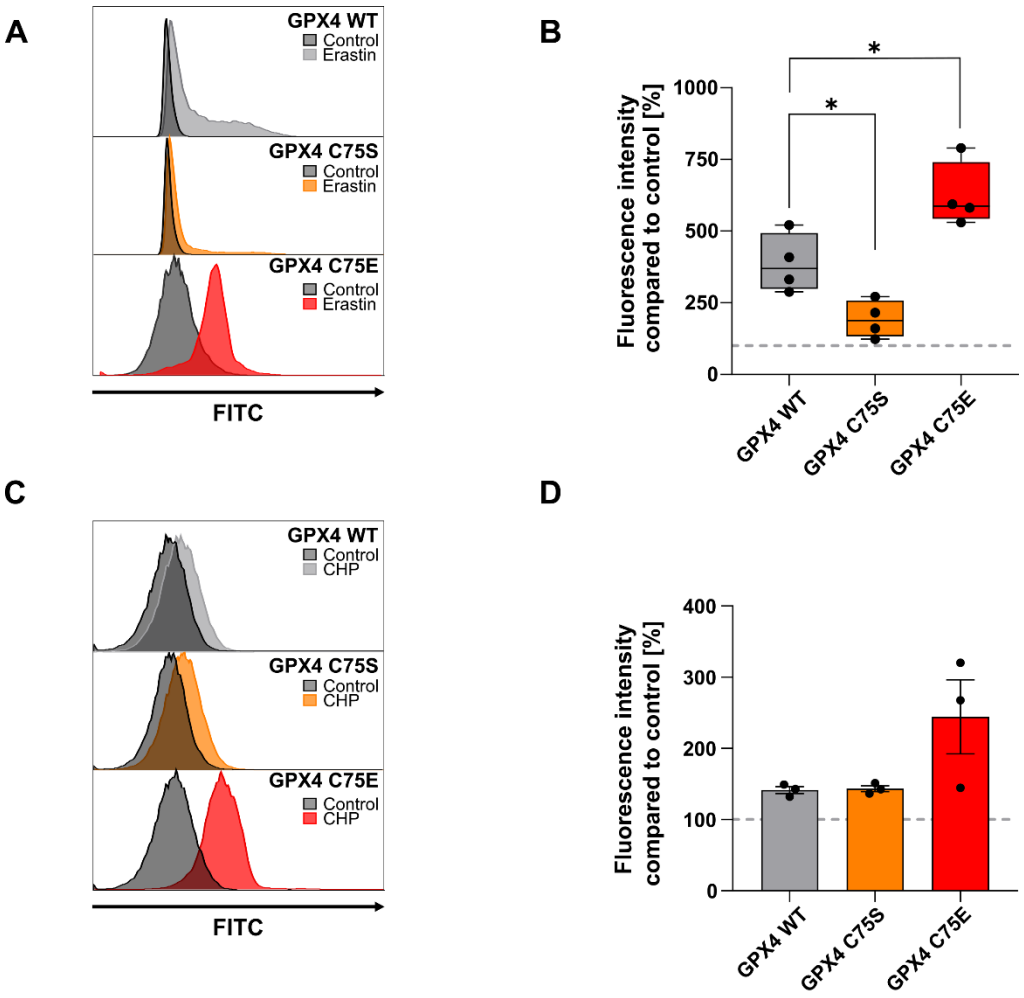

Figure 7: Lipid peroxide accumulation in MEF GPX4 C75 mutants

(A) Flow cytometry analysis in the FITC detector channels measured the fluorescence intensity of oxidized BODIPY C11. A representative histogram illustrates the fluorescence shift between untreated control groups and those exposed to ferroptosis induction with erastin (10 µM). **(B)** A box-whisker plot presents the fluorescence intensity. The gray dotted line marks the untreated control. Black dots indicate individual values from an n = 4 after erastin treatment. One-way ANOVA revealed a p-value of 0.0334 (*) for the comparison of GPX4 WT and GPX4 C75S, and a p-value of 0.0126 (*) for GPX4 WT versus GPX4 C75E. **(C)** Similar to (A), fluorescence intensity of oxidized BODIPY C11 was assessed by flow cytometry, showing the shift in fluorescence between untreated controls and CHP-treated samples (36 µM) in a representative histogram. **(D)** A bar plot displays the fluorescence intensity detected in the FITC detector channel. The gray dotted line represents the untreated control. Black dots indicate individual values from an n = 3 after CHP treatment, with mean and standard error of mean also shown.

9.1.2 C75E mutant has no effect on GPX4 enzyme activity

As indicated by measurements of cell viability and lipid peroxidation, glutathionylation appears to influence resistance to ferroptosis. Therefore, further investigations were conducted to determine the potential causes of this influence. To ensure whether these effects are connected to altered protein expression or stability, GPX4 expression was detected in all three cell lines by western blot (see **8.2.9**). Compared to GPX4 WT MEFs (100 %), the other two cell lines do not show significant differences in GPX4 expression. MEF GPX4 C75S has an increase to 123.7 ± 16.5 % and MEF GPX4 C75E exhibits an increase to 103.3 ± 7.6 % in GPX4 expression (**Figure 8 A-B**). Next, it was tested if the effects are based on changes in enzymatic activity (see **8.2.10**). In order to examine the enzymatic activity of the three GPX4 variants (WT, C75S, and C75E), the respective cell lysates were incubated with the required reaction components (NADPH, GSH, and GR), as well as phosphatidylcholine hydroperoxide (PCOOH) as a substrate. The amount of NADPH consumed, as measured by spectrometric analysis, indicates the amount of PCOOH converted. The measurements show no significant differences in enzymatic activity. The conversion rates of 1 mg of GPX4 WT, GPX4 C75S, and GPX4 C75E were determined to be 12.4 ± 2.6 nmoles PCOOH/minute, 8.8 ± 3.1 nmoles/minute, and 20.4 ± 7.1 nmoles/minute, respectively (**Figure 8 C**).

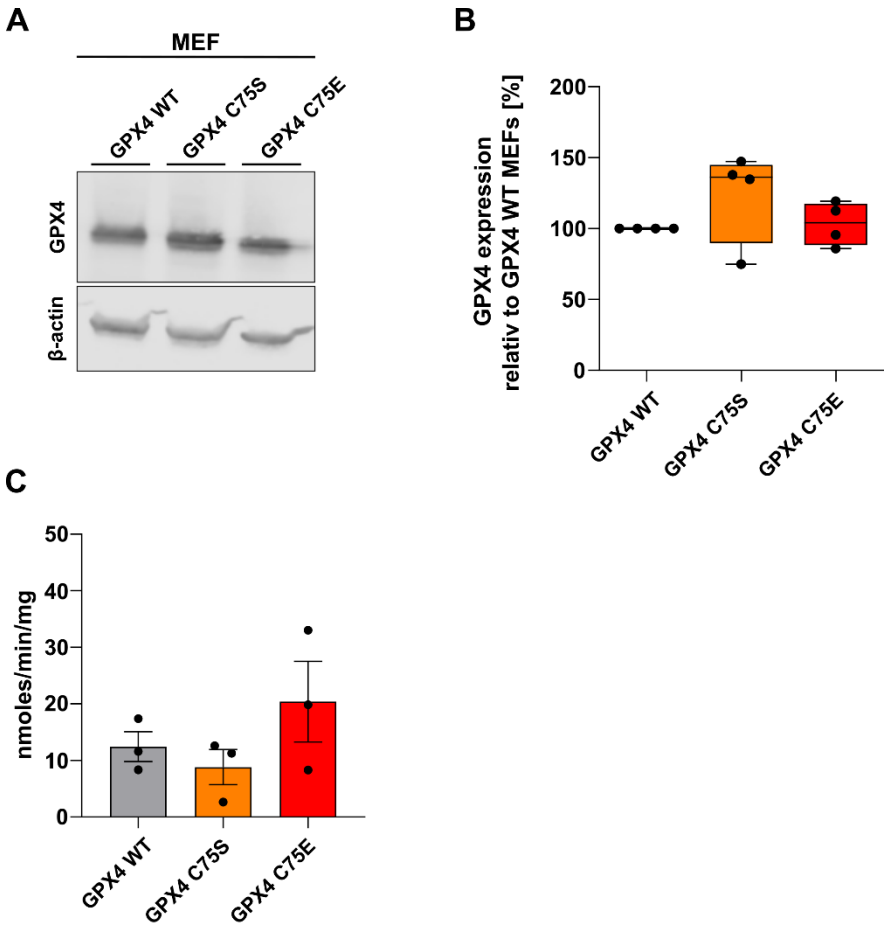

Figure 8: Expression and enzyme activity of GPX4

(A) The expression levels of GPX4 in GPX4 WT MEFs, GPX4 C75S MEFs and GPX4 C75E MEFs are shown in a representative western blot. The housekeeping gene β-actin serves as a loading control. **(B)** Quantification of GPX4 expression is shown in the box-whisker plot. GPX4 signals were first normalized to their corresponding β-actin signals. The resulting values were then expressed relative to GPX4 WT to visualize differences as percentages. Black dots indicate single measurements of n = 4. **(C)** The enzymatic activity of GPX4 was measured based on NADPH consumption after incubating cell lysates with glutathione, glutathione reductase, NADPH, and phosphatidylcholine hydroperoxide (PCOOH) as a substrate. The bar graph represents the amount of PCOOH converted, presented in nmol per minute per mg of GPX4. Black dots represents the individual values of the experiments (n = 3). The mean and standard error of mean are shown.

9.1.3 GPX4 C75E impairs membrane-binding affinity

As demonstrated in **9.1** and **Figure 5**, the electrostatic surface potential is influenced by glutathionylation at C75 of GPX4, resulting in a negatively charged surface at this specific site. Given that GPX4 has the capacity to reduce lipid peroxides at membranes, the membrane-binding affinity of GPX4 was investigated, both with GPX4 WT and with the GPX4 C75E mutant, which is designed to mimic a glutathionylated C75. For this purpose, a bio-layer interferometry was conducted, and the protein binding to nanodiscs loaded with negatively charged POPG phospholipids was measured as described in **8.2.11**. The association curve for GPX4 WT demonstrated a stronger increasing association in comparison to GPX4 C75E, which exhibited a substantially flatter association curve (**Figure 9 A**). After 180 seconds of association measurement, GPX4 C75E retained only 59.8 ± 6.6 % of the binding affinity observed for GPX4 WT (set to 100%) (**Figure 9 B**). The dissociation curves of both GPX4 variants indicated that GPX4 C75E has a greater tendency to dissociate (**Figure 9 A**). The combination of weaker association and faster dissociation suggests that GPX4 C75E has a reduced binding affinity for the POPG phospholipids.

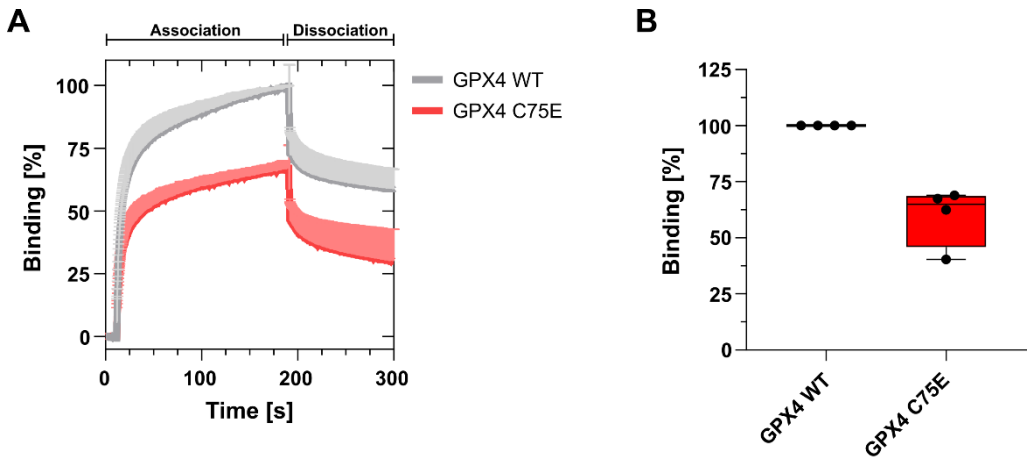

Figure 9: Membrane-binding affinity of GPX4

(A) GPX4 WT (gray) and GPX4 C75E (red) were incubated with nanodiscs loaded with negatively charged POPG phospholipids, and their binding affinity was measured using bio-layer interferometry. The resulting curve illustrates the association and dissociation of GPX4 with these lipids. **(B)** The binding affinity at the end of the association phase (after 180 seconds) is presented in a box-whisker plot. The highest affinity, observed for GPX4 WT, was set to 100 %, and the binding of GPX4 C75E was expressed as a percentage relative to this value. Black dots represent individual measurements (n = 4).

9.1.4 GPX4 C75 is de-glutathionylated under stress conditions

It has been demonstrated that GPX4 C75 undergoes glutathionylation, a modification that appears to influence proper membrane binding (**Figure 5** and **Figure 9**). Additionally, the data presented here so far suggest that glutathionylation at C75 increases cellular susceptibility to ferroptosis (**Figure 6** and **Figure 7**). To determine the conditions under which this modification occurs, the amount of glutathionylated GPX4 was quantified both with and without the induction of ferroptosis as described in **8.2.6**. GPX4 WT MEFs were incubated with the membrane-permeable, biotinylated GSH analog BioGEE, followed by ferroptosis induction using 32 µM CHP or 10 µM erastin. GPX4 were isolated via immunoprecipitation (see **8.2.5**), and levels of BioGEE bound to GPX4 were evaluated by western blot analysis (see **8.2.9**). In comparison with the control group, which was set to 100 %, the CHP-treated group demonstrated a decrease in bound BioGEE to 58.0 ± 6.3 %. The erastin-treated group exhibited a reduction to 79.8 ± 4.7 % (**Figure 10**). These findings suggest that ferroptosis conditions result in reduced BioGEE binding to GPX4, indicating a decrease in GPX4 glutathionylation.

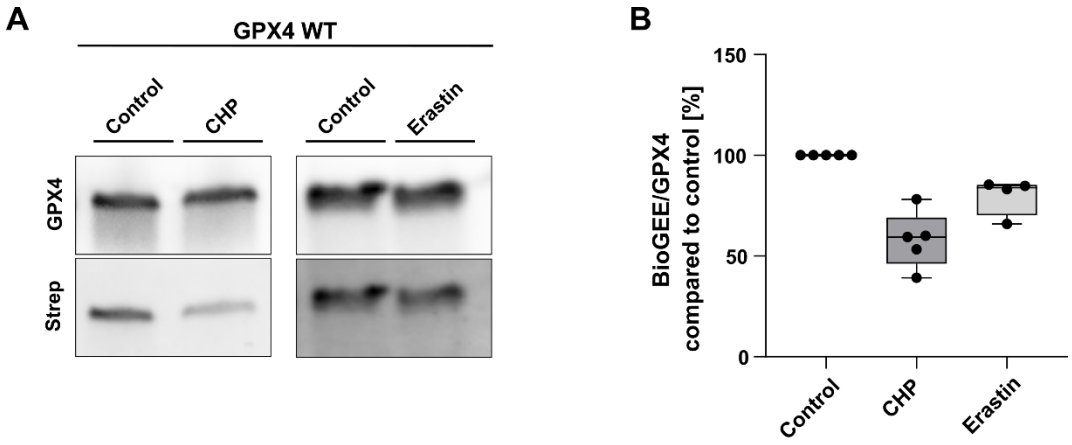

Figure 10: Levels of glutathionylated GPX4

(A) The representative western blots display GPX4 levels (detected using a GPX4 antibody) and its interaction with the biotinylated glutathione analog BioGEE. BioGEE was visualized using a streptavidin antibody (Strep). The left blot compares GPX4 isolated from CHP-treated cells to GPX4 isolated from the control cells, while the right blot compares GPX4 isolated from erastin-treated and control cells. **(B)** The box-whisker plot represents the relative amount of BioGEE bound to GPX4 following quantitative analysis, with the CHP- and erastin-treated groups normalized to the control group (set to 100 %). Black dots represent individual relative values (n = 5 for control and CHP-treated and n = 4 for erastin-treated samples).

9.2 Role of Grx2 in ferroptosis

Glutaredoxin 2 (Grx2) is a key element in redox regulation since it is able to reduce posttranslational modifications like glutathionylation. To investigate if GPX4 is a potential substrate for Grx2, GPX4 from GPX4 WT MEFs and GPX4 C75S MEFs were isolated via immunoprecipitation and incubated with fluorescence-labeled GSSG as described in **8.2.5** and **8.2.7**. Subsequent incubation with Grx2 and GSH provides the fundamental basis for the potential reduction of GPX4 and the subsequent cleavage of GSSG. The visualization of the remaining GSSG on GPX4 was achieved through gel electrophoresis (see **8.2.9**), by using UV light to stimulate fluorescence. The fluorescent GSSG signal exhibited a time-dependent decrease in GPX4 WT, indicating that Grx2 cleaved GSSG from GPX4, thereby suggesting that GPX4 is a substrate for Grx2. In the absence of Grx2, incubation with GSH alone does yield a minor observable effect, thus serving as a control condition (**Figure 11 A**). The same experiment was also carried out with GPX4 C75S. The presence of a serine at this position, as instead of the cysteine, results in the inability of the fluorescent GSSG to bind at position 75. This experiment yielded a weak signal for GSSG, and no decrease was observed upon the addition of Grx2 (**Figure 11 B**). These findings suggest that cysteine 75 is a specific target of Grx2.

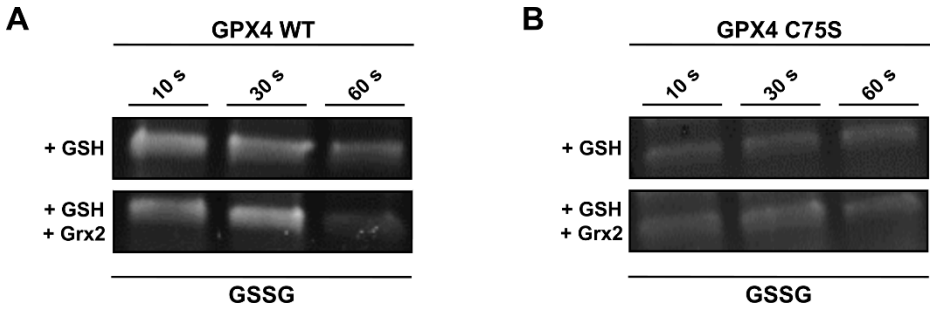

Figure 11: Interaction of Grx2 with GPX4 C75

Immunoprecipitated GPX4 WT **(A)** and GPX4 C75S **(B)** were incubated with fluorescently labeled GSSG, followed by incubation with either 1 mM GSH alone or 1 mM GSH in combination with 100 nM recombinant Grx2. The reaction was stopped after 10, 30, and 60 seconds, and GPX4 was analyzed by gel electrophoresis. The remaining fluorescent GSSG was visualized under UV light.

9.2.1 Grx2$^{-/-}$ MEFs are more susceptible to ferroptosis

In order to investigate the potential impact of Grx2 on ferroptosis, experiments were conducted using MEFs derived from wild-type (WT) and Grx2-deficient (Grx2$^{-/-}$) mice. The cell lines utilized in these experiments were provided by Marcus Conrad and his team at the Helmholtz Center in Munich. A western blot analysis of the two cell lines (Grx2 WT MEFs and Grx2$^{-/-}$ MEFs) revealed a distinct Grx2 signal in the Grx2 WT MEFs, while no Grx2 signal was detected in the Grx2$^{-/-}$ MEFs, confirming the successful knockout of Grx2 in the Grx2$^{-/-}$ MEFs (**Figure 12**).

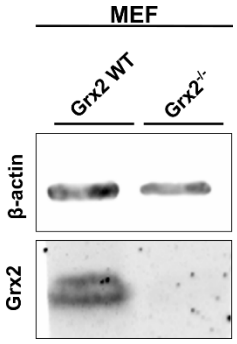

Figure 12: Grx2 expression levels in Grx2 MEFs

Representative western blot showing Grx2 protein expression in Grx2 WT MEFs and Grx2$^{-/-}$ MEFs. β-actin served as a loading control to ensure equal protein loading.

To test the overall effect of ferroptosis on Grx2 MEFs, a cell viability assay was performed as outlined in **8.2.3**. The results of this assay demonstrated a significant decrease in cell survival after ferroptosis induction with increasing concentrations of erastin (0.1 µM – 100 µM) in Grx2$^{-/-}$ MEFs, with an IC_{50} value of 3.6 ± 1.2 µM, in contrast to the 19.4 ± 3.7 µM value observed for Grx2 WT MEFs. The additional treatment with 100 nM of the ferroptosis inhibitor liproxstatin-1 (Lip-1) resulted in a significant enhancement of cell survival, with an IC_{50} value of 34.1 ± 0.7 µM for Grx2 WT MEFs and 20.6 ± 5.5 µM for Grx2$^{-/-}$ MEFs after erastin treatment (**Figure 13 A-B**). In addition, following the induction of ferroptosis with increasing concentrations of CHP (1 µM – 320 µM), Grx2$^{-/-}$ MEFs exhibited a diminished cell survival in comparison to Grx2 WT MEFs. The IC_{50} value of CHP treatment was determined to be 67.0 ± 25.4 µM for Grx2 WT and 30.6 ± 8.9 µM for Grx2$^{-/-}$ MEFs (**Figure 13 C-D**).

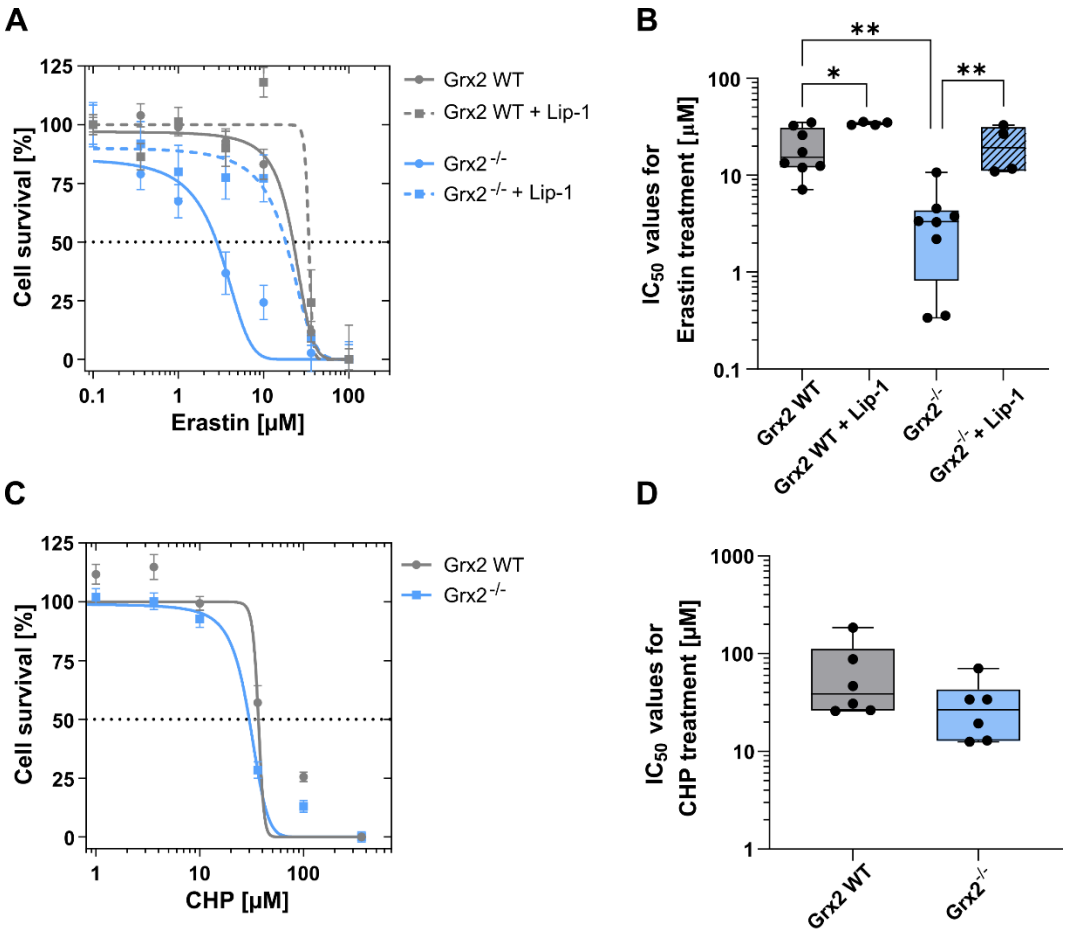

Figure 13: Impact of Grx2 on cell viability after ferroptosis induction

(A) The concentration-response curve illustrates the survival rates of MEF Grx2 WT (gray) and MEF Grx2$^{-/-}$ (blue) after ferroptosis induction with increasing erastin concentrations (0.1 µM – 100 µM), either in the presence of 100 nM of the ferroptosis inhibitor Lip-1 (dotted lines) or without Lip-1 (solid lines). Mean values (Grx2 WT: n = 8; Grx2 WT + Lip-1: n = 4; Grx2$^{-/-}$: n = 8; Grx2$^{-/-}$ + Lip-1: n = 4) and the standard error of the mean are shown. **(B)** A box-whisker plot represents the IC_{50} values for all four groups. Black dots indicate individual IC_{50} values. A one-way ANOVA revealed a significant difference between Grx2 WT and Grx2 WT + Lip-1 (p = 0.0165, *), Grx2 WT and Grx2$^{-/-}$ (p = 0.0016, **), and Grx2$^{-/-}$ and Grx2$^{-/-}$ + Lip-1 (p = 0.0054, **). **(C)** The second concentration-response curve shows the survival rates of both cell lines in response to ferroptosis induction with increasing concentrations of cumene hydroperoxide (CHP) (1 µM – 320 µM). The mean values (n = 6) and the standard error of the mean are presented. **(D)** A box-whisker plot displays the IC_{50} values. Black dots represent individual IC_{50} values. The trend lines shown in figures A and C are for illustrative purposes only and were not used in further calculations.

The accumulation of lipid peroxides – a well-established hallmark of ferroptosis - was analyzed in Grx2 WT and Grx2$^{-/-}$ MEFs using BODIPY C11 in combination with flow cytometry, as outlined in **8.2.4**. Following the induction of ferroptosis with 10 µM erastin, a significant increase in oxidized BODIPY levels was observed in both cell lines. In Grx2 WT MEFs, the levels of oxidized BODIPY increased to 242.3 ± 32.7 %, relative to the untreated control group, which was set to 100 %. In contrast, Grx2$^{-/-}$ MEFs exhibited a

significantly higher accumulation of lipid peroxides, with oxidized BODIPY levels reaching 641.4 ± 98.3 % compared to their respective control (**Figure 14**).

Combined with the results of the cell viability assay (**Figure 13**), these findings suggest a protective role of Grx2 against ferroptosis. This is reflected in the increased sensitivity of Grx2-deficient cells, as demonstrated by both reduced cell survival and elevated lipid peroxide accumulation following ferroptosis induction.

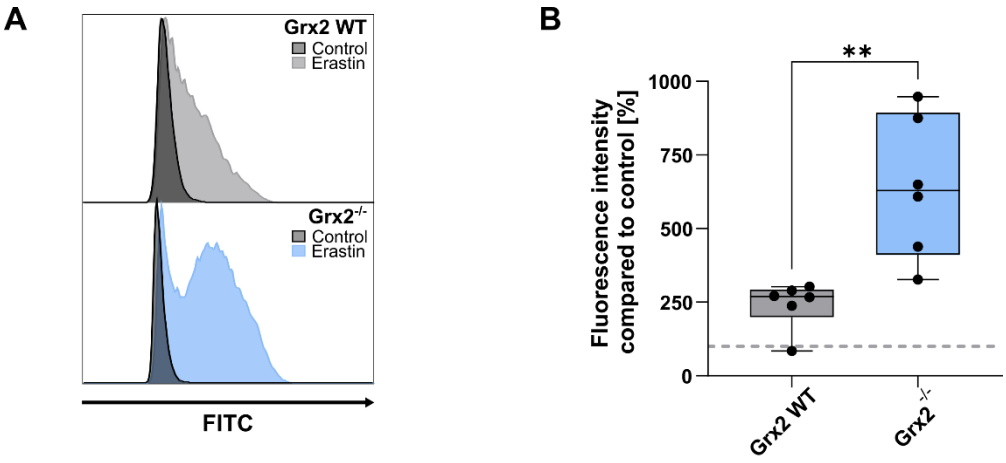

Figure 14: Effect of Grx2 on lipid peroxidation accumulation

(A) The fluorescence intensity of oxidized BODIPY C11 was measured by flow cytometry in the FITC detector channels. A representative histogram shows the fluorescence shift between untreated control groups and those exposed to ferroptosis induction with erastin (10 µM) and were already obtained during my master's thesis. **(B)** A box-whisker plot shows the mean intensity of the fluorescence. The gray dotted line indicates the untreated control. Black dots indicate individual values from n = 6 after erastin treatment. Unpaired t-test revealed a significant difference between Grx2 WT and Grx2$^{-/-}$ with a p-value of 0.0032 (**).

9.2.2 Impact of the Grx2 deficiency in mouse cells

Since the data presented above suggest that Grx2 impacts GPX4 functionality, it was investigated whether compensatory cellular mechanisms exist to counteract this effect under basal conditions and without any ferroptosis induction.

Given that GPX4 is the only mammalian enzyme capable of reducing the toxic lipid peroxides, its expression levels were analyzed in both Grx2 WT and Grx2$^{-/-}$ MEFs. Western blot analysis (see **8.2.9**) of cell lysates, followed by signal quantification, revealed an increase in GPX4 expression in the Grx2$^{-/-}$ MEFs, reaching 198.1 ± 37.8 % relative to Grx2 WT MEFs, which were set to 100 % (**Figure 15**).

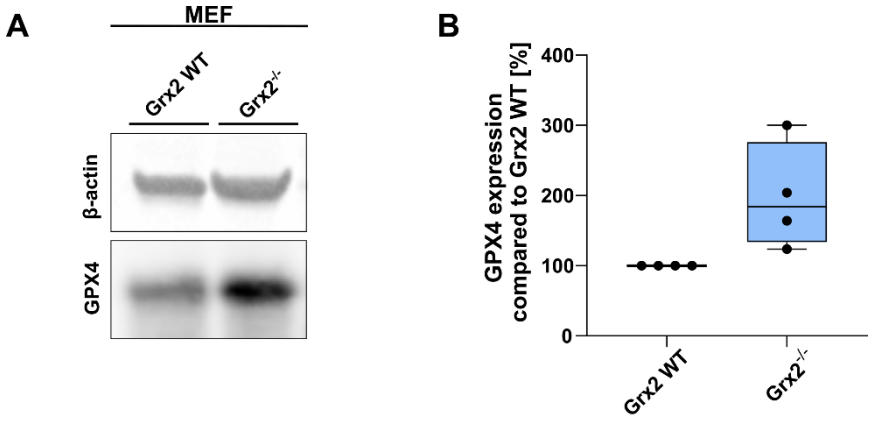

Figure 15: GPX4 expression in Grx2 MEFs

(A) The representative western blot illustrating GPX4 expression in Grx2 WT and Grx2$^{-/-}$ MEFs in the absence of ferroptosis induction. β-actin staining serves as a loading control. **(B)** A box-whisker plot quantifies GPX4 expression in Grx2 MEFs. GPX4 signals were first normalized to their respective β-actin signals, and the resulting values were expressed relative to Grx2 WT to highlight differences as percentages. Black dots represent individual measurements (n = 4).

Glutathione (GSH) is the substrate required by GPX4 to convert lipid peroxides. To detect possible differences in GSH levels, Grx2 WT and Grx2$^{-/-}$ MEFs were labeled with β-(4-hydroxyphenyl)ethyl iodoacetamide (see **8.2.12**) and subsequently analyzed by Takaaki Akaike and his team in the Department of Environmental Medicine and Molecular Toxicology at the Tohoku University in Sendai, by mass spectrometry. The analysis revealed an intracellular GSH level of 979.0 ± 139.8 pmol/mg protein in Grx2 WT MEFs. In contrast, Grx2$^{-/-}$ MEFs showed a significantly elevated GSH level, reaching 3255.9 ± 298.5 pmol/mg protein (**Figure 16**).

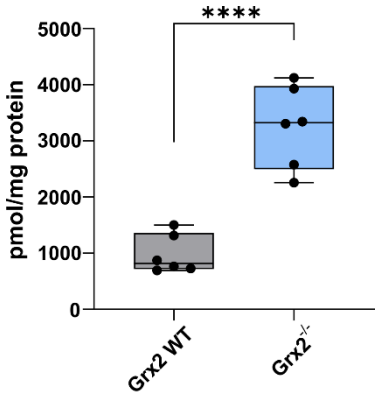

Figure 16: GSH level in Grx2 MEFs

The box-whisker plot illustrates the amount of GSH in Grx2 WT MEFs and Grx2$^{-/-}$ MEFs, expressed in pmol per mg of protein. GSH levels were determined by mass spectrometry analysis conducted by Takaaki Akaike and his team at the Department of Environmental Medicine and Molecular Toxicology, Tohoku University, Sendai, Japan. Black dots represent individual values from n = 6. An unpaired t-test comparing Grx2 WT and Grx2$^{-/-}$ MEFs revealed a p-value of <0.0001 (****).

As described in **6.1.2**, phosphatidylcholine lipids represent the most prevalent type of glycerophospholipids within mammalian cell membranes. To examine differences in the glycerophospholipid content, a lipidomic analysis of Grx2 WT and Grx2$^{-/-}$ MEFs was conducted by Christoph Thiele at the Life and Medical Science Institute at the University of Bonn. The analysis revealed elevated levels of phosphatidylcholine peroxides in Grx2$^{-/-}$ MEFs compared to Grx2 WT MEFs. Specifically, Grx2 WT MEFs displayed a phosphatidylcholine peroxide level of 50.3 ± 3.5 pmol, whereas Grx2$^{-/-}$ MEFs showed an increased amount of 73.1 ± 3.5 pmol (**Figure 17 A**). The same measurment was performed using HeLa cells transfected with control siRNA (siCtrl) or Grx2 siRNA (siGrx2) (see **8.2.2**). Transfection with siGrx2 were used to silence expression of Grx2, where unspecific siRNA (siCtrl) was used as control. Lipidomics analysis revealed increased levels of phosphatylcholine peroxides in HeLa siGrx2 (58.2 ± 3.0 pmol) compared to HeLa siCtrl (28.3 ± 0.3 pmol) (**Figure 17 B**).

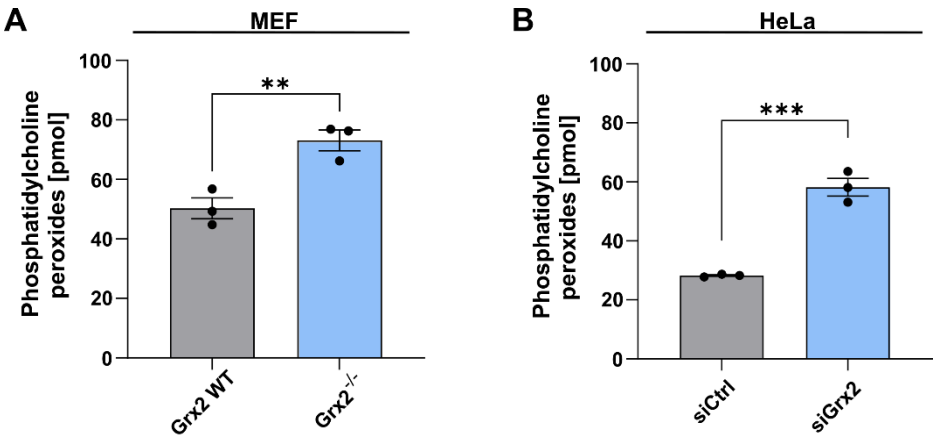

Figure 17: Level of phosphatidylcholine peroxides in cells lacking Grx2

The bar plots presents the level of peroxidized phosphatidylcholine lipids in **(A)** Grx2 WT and Grx2$^{-/-}$ MEFs and in **(B)** siCtrl and siGrx2 transfected HeLa cells. Lipidomic analysis was performed by Christoph Thiele at the Life and Medical Science Institute at the University of Bonn. Black dots represent individual values (n = 3). The mean and standard error of mean are shown. An unpaired t-test revealed a p-value of 0.0098 (**) for the comparison of Grx2 WT and Grx2$^{-/-}$ and an p-value of 0.0006 (***) for the comparison of siCtrl and siGrx2.

9.2.3 Impact of the Grx2 deficiency in mouse tissues

Lipid peroxidation is an important hallmark of ferroptosis. To investigate the previously demonstrated protective role of Grx2 not only in cell culture but also in tissues, the accumulation of 4-hydroxynonenal (4-HNE) – a byproduct of lipid peroxidation – was measured in the liver and brain of 15-month-old WT and Grx2$^{-/-}$ mice. Immunohistochemical staining was performed using a 4-HNE antibody with hematoxylin counterstaining to visualize cell nuclei as outlined in **8.2.15**. The staining revealed a markedly stronger brown staining in both liver and brain tissues of Grx2$^{-/-}$ mice compared to WT mice, indicating increased 4-HNE accumulation and consequently increased lipid peroxidation in the absence of Grx2 (**Figure 18**).

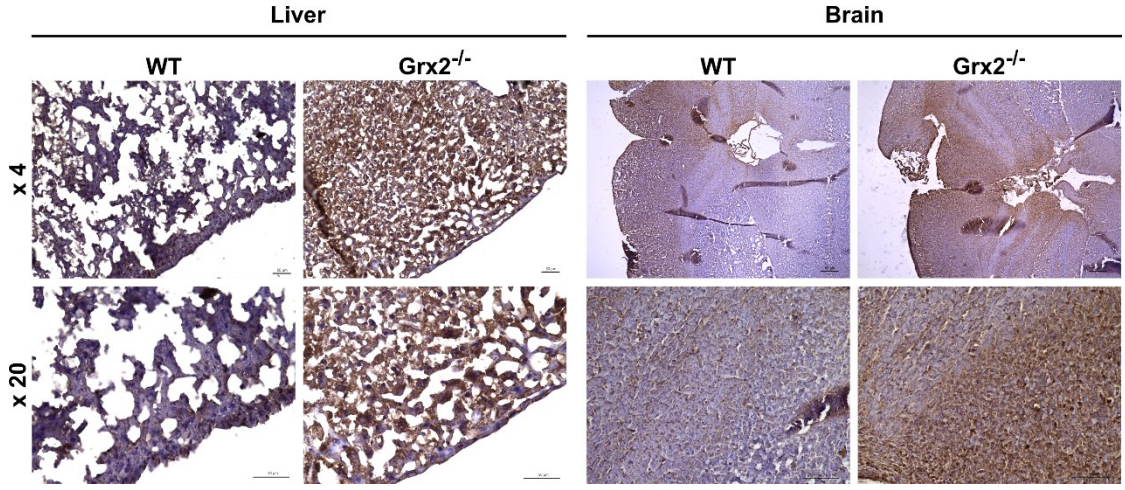

Figure 18: 4-HNE accumulation in liver and brain of aged mice

Representative microscopy images of 8 µm thick sections from the liver (left) and brain (right) of 15-month-old WT and Grx2$^{-/-}$ mice. Immunohistochemical staining was performed using a 4-HNE antibody (brown), with hematoxylin counterstaining (blue) to visualize tissue structure.

To investigate whether these differences occur at an earlier age, the same staining was performed on tissues from 2-week-old mice. While no detectable 4-HNE signal was observed in liver tissues of either WT or Grx2$^{-/-}$ mice, a weak 4-HNE signal was present in WT brains tissues. In contrast, the Grx2$^{-/-}$ brain tissues showed a more pronounced 4-HNE signal in the brain, suggesting increased lipid peroxidation even in young Grx2$^{-/-}$ mice brains, compared to their WT counterparts (**Figure 19**).

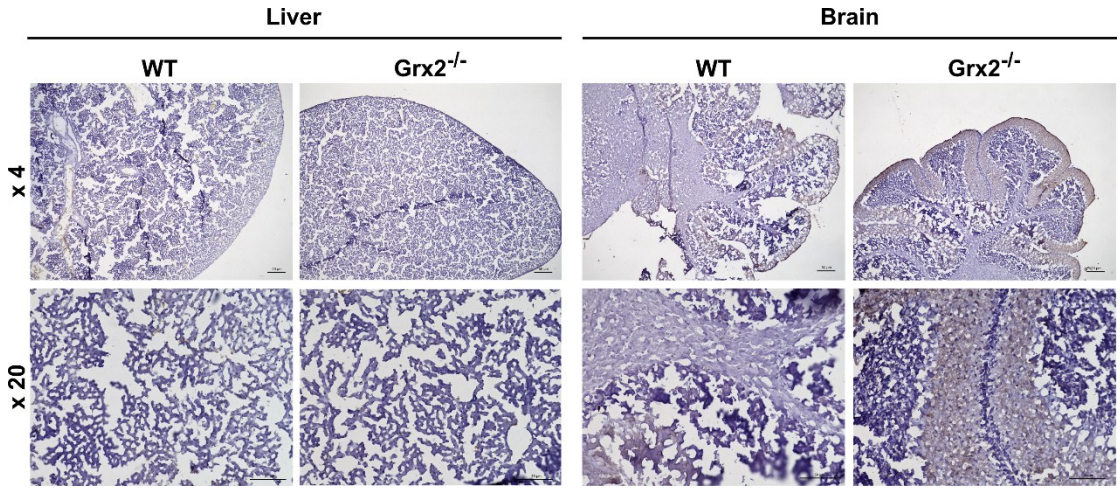

Figure 19: 4-HNE accumulation in liver and brain of young mice

Representative microscopy images of 8 µm thick sections from liver (left) and brain (right) of 2-week-old WT and Grx2$^{-/-}$ mice. Immunohistochemistry was performed using a 4-HNE antibody (brown). Hematoxylin counterstaining (blue) was used to visualize tissue structure.

Parvalbumin-positive (PV^{+}) neurons are GABAergic interneurons in the brain and play a central role in the regulation of excitability of neuronal networks by inhibiting excessive neuronal excitation. In addition, PV^{+} neurons show a particular susceptibility to oxidative stress and lipid peroxidation, as demonstrated in studies from 2010 and 2018 [31, 83]. Both the knockout of GPX4 and the expression of the inactive mutant GPX4 U46C in mice have been shown to lead to cell death of these PV^{+} neurons [31, 83].

To investigate the impact of Grx2 deficiency on these neurons, the brains of 6-month-old WT and Grx2$^{-/-}$ mice were isolated and sectioned into 75 µm thick slices. Immunohistochemistry was performed as deliniated in **8.2.15** using a parvalbumin antibody to specifically label PV^{+} neurons. PV^{+} neurons were counted within 0.14 mm^2 fields at three distinct positions per region of interest (cortex, dentate gyrus, cerebellum), with the analysis performed in a blinded manner. The results revealed a reduced number of PV^{+} neurons in the Grx2$^{-/-}$ mouse brains compared to WT brains across all examined regions. In the cortex, the average number of PV^{+} neurons was 54.6 ± 4.5 per 0.14 mm² in WT mice, while Grx2$^{-/-}$ mice exhibited an average of 37.2 ± 4.6. In the dentate gyrus of the hippocampus, the counts were 20.2 ± 1.0 PV^{+} neurons in WT mice and 14.9 ± 1.4 PV^{+} neurons in Grx2$^{-/-}$ mice per 0.14 mm^2. In the cerebellum, WT brains contained an average of 37.0 ± 4.6 PV^{+} neurons, compared to 24.5 ± 1.6 in Grx2$^{-/-}$ brains per 0.14 mm^2 (**Figure 20**)

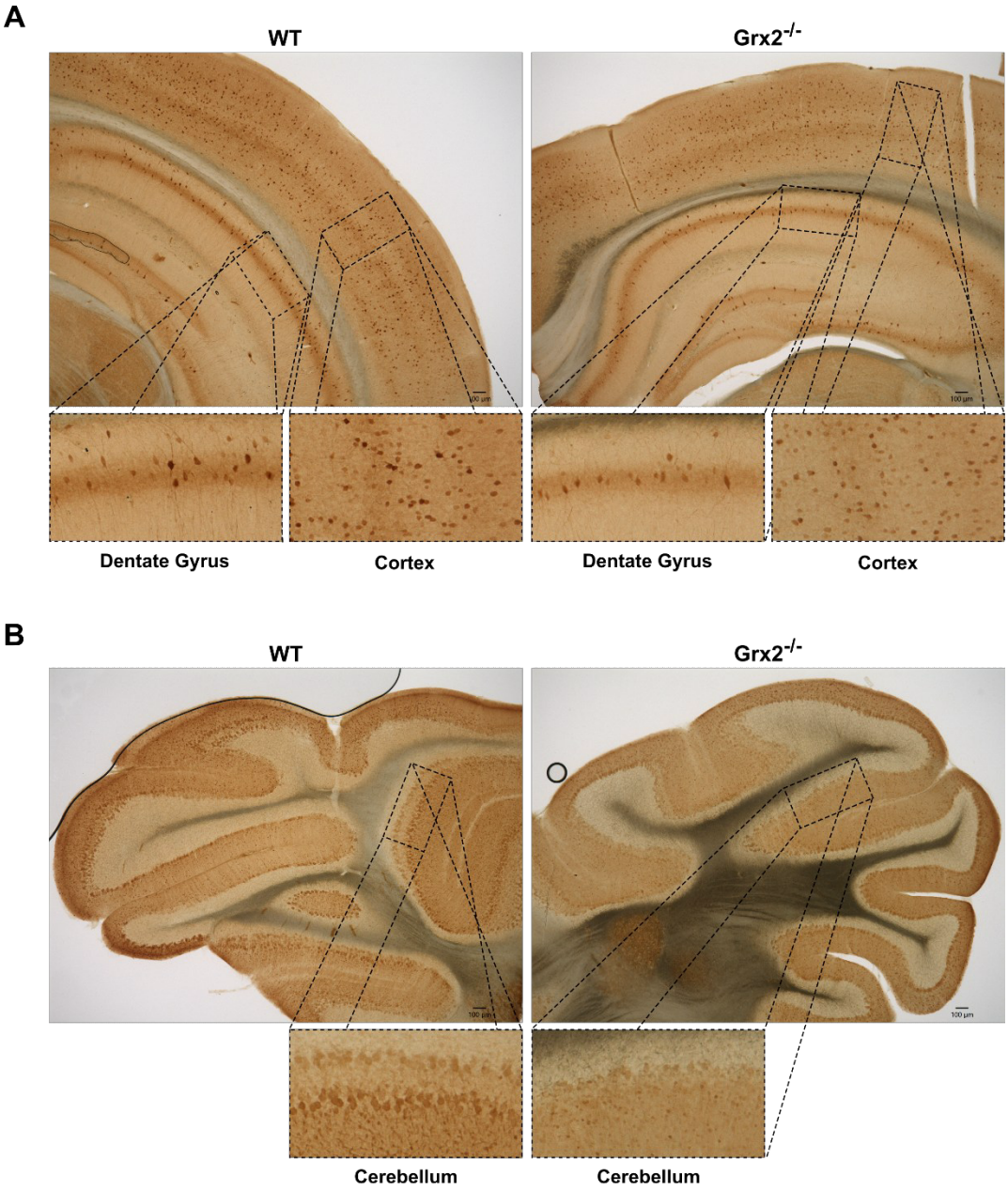

Figure 20: Parvalbumin^{+} neurons in Grx2$^{-/-}$ mouse brains

(A) Representative microscopy images of 75 µm thick brain sections from 6-month-old WT and Grx2$^{-/-}$ mice, which were stained with a parvalbumin antibody. The figure focuses on the cortex and dentate gyrus. **(B)** Representative images of parvalbumin-stained sections from the cerebellum. **(C)** The dot plot quantifies the number of parvalbumin-positive neurons per field (0.14 mm²) in the cortex, dentate gyrus, and cerebellum. For each brain region, three sections per mouse (from three mice per group) were stained, and three fields per region were counted in a blinded manner. Comparing WT and Grx2$^{-/-}$ in each region, Mann-Whitney test revealed a p value of 0.0055 (**) for the cortex, 0.0007 (***) for the dentate gyrus, and 0.0013 (**) for the cerebellum.

The experiment was repeated with 1-week-old mice to investigate the influence of Grx2 on PV^+ neurons at an earlier stage of development. Immunohistochemistry was performed, and 75 µm thick sections were stained using a parvalbumin antibody as delineated in **8.2.15**. The number of PV^+ neurons in the cerebellum of $Grx2^{-/-}$ mice is reduced compared to that of WT mice. On average, 18.4 ± 2.4 PV^+ neurons per 0.14 mm^2 were counted in $Grx2^{-/-}$ mice, whereas 26.8 ± 2.6 PV^+ neurons per 0.14 mm^2 were counted in the WT mice (**Figure 21**).

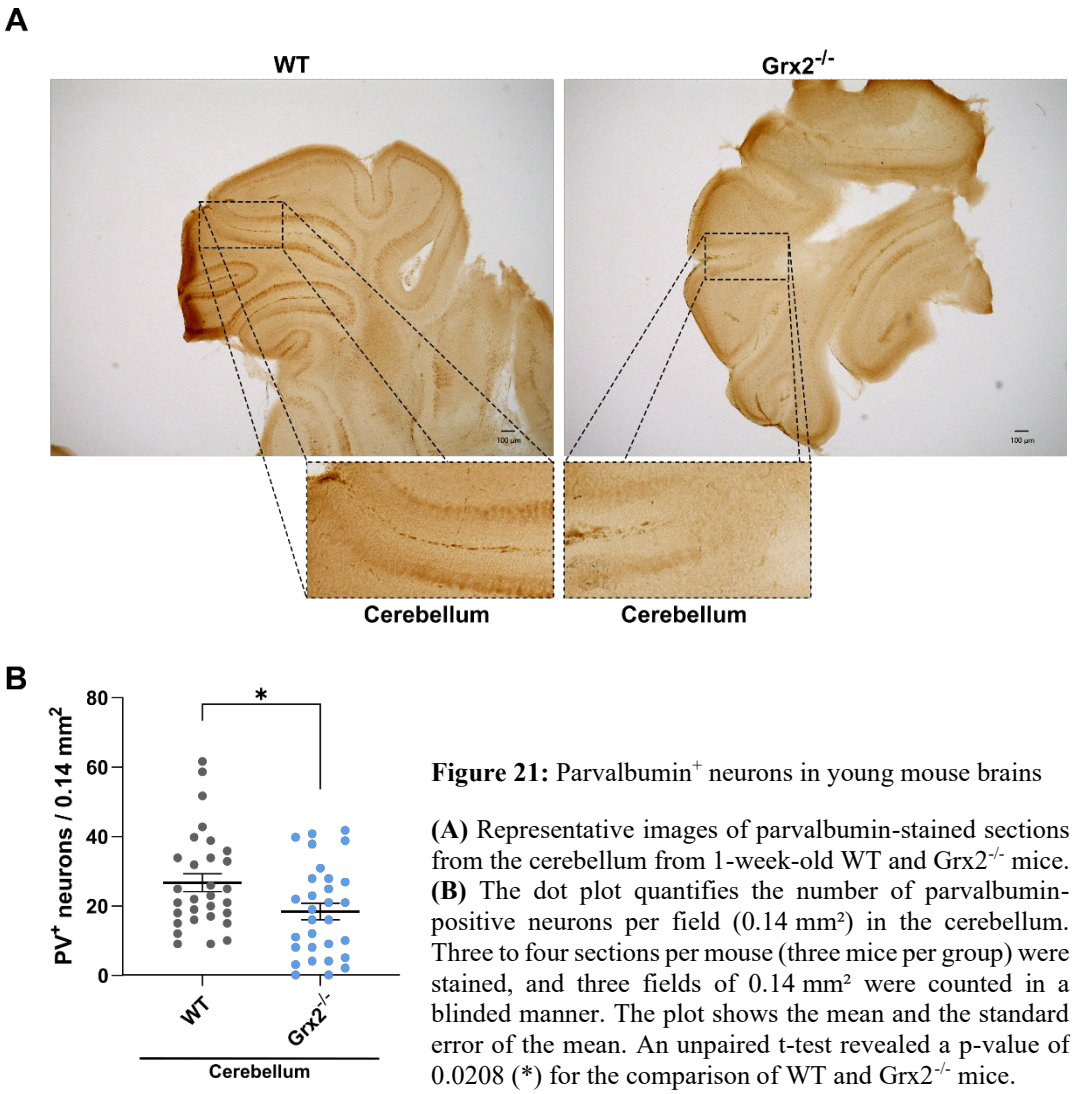

Figure 21: Parvalbumin$^+$ neurons in young mouse brains

(A) Representative images of parvalbumin-stained sections from the cerebellum from 1-week-old WT and $Grx2^{-/-}$ mice. **(B)** The dot plot quantifies the number of parvalbumin-positive neurons per field (0.14 mm^2) in the cerebellum. Three to four sections per mouse (three mice per group) were stained, and three fields of 0.14 mm^2 were counted in a blinded manner. The plot shows the mean and the standard error of the mean. An unpaired t-test revealed a p-value of 0.0208 (*) for the comparison of WT and $Grx2^{-/-}$ mice.

9.2.4 Grx2-overexpressing cells are more resistant to ferroptosis

In order to investigate whether a protective effect of Grx2 against ferroptosis can be achieved by higher intracellular levels of Grx2, cell survival assays were performed using HeLa cell lines overexpressing either the mitochondrial isoform of Grx2 (Grx2a) or the cytosolic isoform (Grx2c) as delineated in **8.2.3**. The three cell lines (HeLa WT, HeLa Grx2a, and HeLa Grx2c) were provided by Arne Holmgren from the Karolinska Institute in Sweden and established by Enoksson *et al.* in 2005 [79].

The induction of ferroptosis in these cells using increasing concentrations of erastin (0.1 µM – 100 µM) resulted in a modest increase in cell survival, particularly for the Grx2a and Grx2c overexpressing HeLa cells. The resulting IC_{50} values for the HeLa cells were 16.7 ± 5.5 µM for HeLa WT, 24.0 ± 7.1 µM for HeLa Grx2a, and 23.2 ± 6.4 µM for HeLa Grx2c (**Figure 22 A-B**). The same trend was observed by inducing ferroptosis with increasing concentrations of CHP (1 µM – 1000 µM). The Grx2a and Grx2c overexpressing HeLa cells exhibited a significant increase in cell survival compared to WT HeLa cells. The calculation of IC_{50} values revealed that HeLa WT cells exhibited an IC_{50} of 32.9 ± 8.7 µM, HeLa Grx2a cells demonstrated an IC_{50} of 174.3 ± 31.0 µM, and HeLa Grx2c cells showed an IC_{50} of 161.2 ± 37.1 µM (**Figure 22 C-D**).

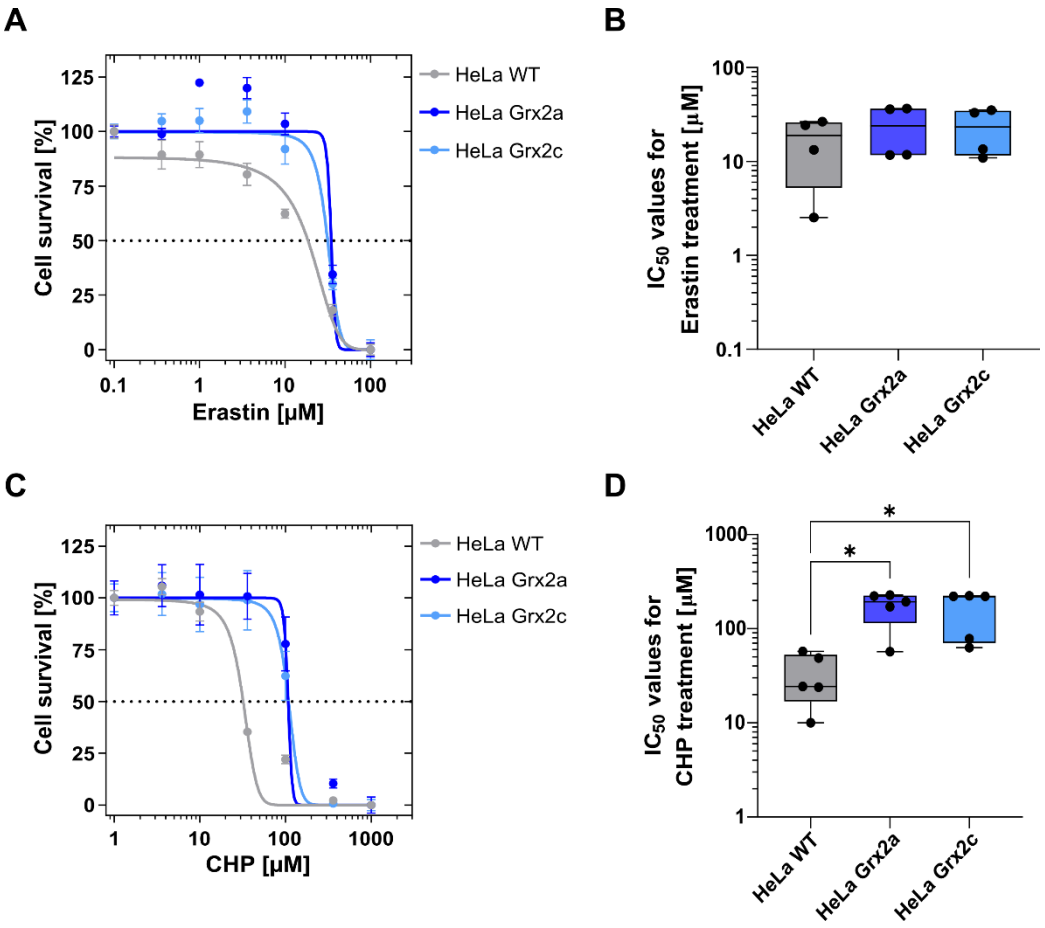

Figure 22: Cell viability of Grx2 overexpressing HeLa cells after ferroptosis induction

(A) The concentration-response curve illustrates the survival rates of HeLa WT (gray), HeLa Grx2a (dark blue), and HeLa Grx2c (light blue) subsequent to ferroptosis induction with increasing erastin concentrations (0.1 µM - 100 µM). The mean values (n = 4) and the standard error of the mean are shown. **(B)** A box-whisker plot represents the IC_{50} values derived from (A) for the three HeLa cell lines. Black dots indicate individual IC_{50} values. **(C)** The second concentration-response curve shows the survival rates of the three cell lines in response to ferroptosis induction with increasing concentrations of cumene hydroperoxide (CHP) (1 µM – 1000 µM). The mean values were calculated for n = 5, along with the standard error of the mean. **(D)** A box-whisker plot displays the IC_{50} values derived from (C). Black dots represent individual IC_{50} values. A Kruskal-Wallis test comparing HeLa WT with HeLa Grx2a and HeLa Grx2c yielded p-values of 0.0218 (*). The trend lines shown in figures A and C are for illustrative purposes only and were not used in further calculations.

The level of lipid peroxidation, which serves as an indicator for ferroptosis, was quantified through the use of BODIPY C11 staining and subsequent analysis via flow cytometry as described in **8.2.4**. Induction of ferroptosis using CHP (32 µM) lead to an increase in oxidized BODIPY to 352.7 ± 58.1 % in WT HeLa cells, in comparison to the control group, which was set to 100 %. In contrast, Grx2a and Grx2c overexpressing HeLa cells exhibited a significant diminished increase in oxidized BODIPY intensity, reaching 202.4 ± 32.3 %

in Grx2a HeLa and 197.4 ± 32.1 % in Grx2c HeLa, compared to their respective control groups, which were set to 100 % (**Figure 23**).

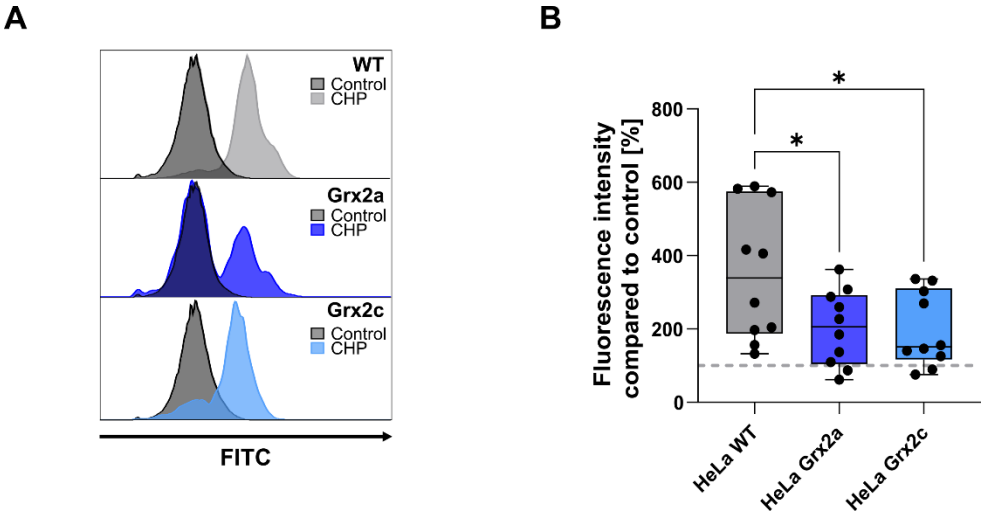

Figure 23: Effect of Grx2 overexpression on lipid peroxidation accumulation in HeLa cells

(A) The fluorescence intensity of oxidized BODIPY C11 was measured by flow cytometry in the FITC detector channels. A representative histogram shows the fluorescence shift between untreated control groups and those exposed to ferroptosis induction with CHP (32 µM). **(B)** A box-whisker plot shows the mean intensity of the fluorescence. The gray dotted line indicates the untreated control. Black dots indicate individual values from n = 10 after CHP treatment. One-way ANOVA revealed a significant difference between HeLa WT and HeLa Grx2a with a p-value of 0.0353 (*), and between HeLa WT and HeLa Grx2c with a p-value of 0.0294 (*). The results were partially obtained by Morris Haid under my supervision and are part of his bachelor's thesis.

9.3 Role of Grx1 in ferroptosis

Grx1, similar to Grx2, is an oxidoreductase that has the capacity to reduce glutathionylation. To explore the role of Grx1 in ferroptosis and assess the specificity of Grx2, cell viability and lipid peroxidation assays were conducted using Grx1-deficient MEFs (MEF Grx1$^{-/-}$). The primary Grx1 WT and Grx1$^{-/-}$ MEFs were isolated and provided by Yvonne Janssen-Heininger at the University of Vermont, and the resulting cell line was established by me. The successful knockout of Grx1 in these cells was confirmed by a representative western blot (**Figure 24**) (see **8.2.9**).

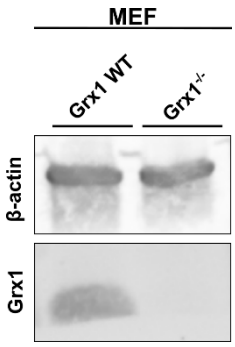

Figure 24: Grx1 expression levels in Grx1 MEFs

Representative western blot showing Grx1 protein expression in Grx1 WT MEFs and Grx1$^{-/-}$ MEFs. β-actin served as a loading control to ensure equal protein loading.

Cell viability was assessed in the MEF Grx1 WT and MEF Grx1$^{-/-}$ cell lines after induction of ferroptosis using increasing concentrations of erastin (0.1 µM – 100 µM) as described in **8.2.3**. The IC_{50} values exhibited no difference between Grx1 WT MEFs (16.3 ± 2.1 µM) and Grx1$^{-/-}$ MEFs (18.8 ± 4.1 µM) (**Figure 25**).

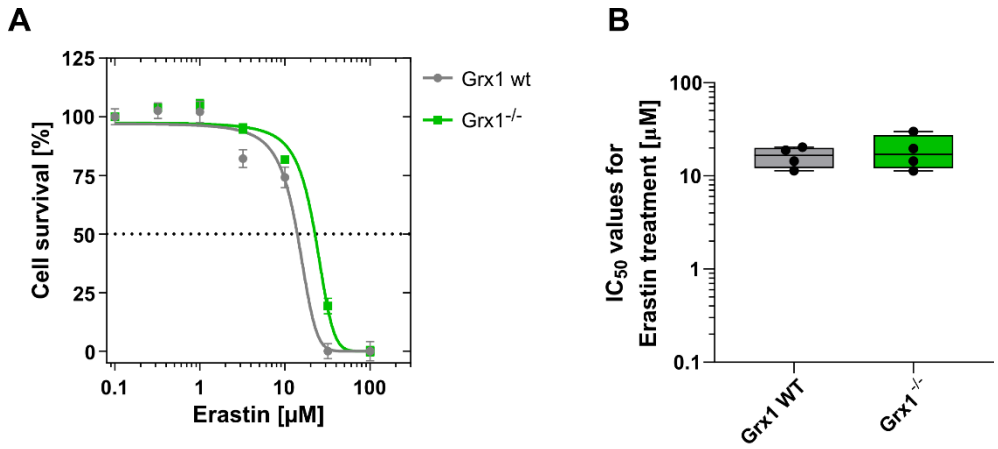

Figure 25: Effect of Grx1$^{-/-}$ on cell viability after ferroptosis induction

(A) The concentration-response curve shows the survival rates of MEF Grx1 WT (gray) and MEF Grx1$^{-/-}$ (green) cells after ferroptosis induction with increasing concentrations of erastin (0.1 µM – 100 µM). Data represent mean values (n = 4) and the standard error of the mean. The trend lines are for visualization purposes only and were not used for further calculations. **(B)** A box-whisker plot displays the IC_{50} values for both cell lines. Black dots represent individual IC_{50} measurements.

The accumulation of lipid peroxidation was measured using BODIPY C11 staining and flow cytometry after the induction of ferroptosis with CHP (32 µM) (see **8.2.4**). The analysis revealed an elevation of oxidized BODIPY levels in Grx1 WT MEFs, which reached 162.8 ± 44.8 % after ferroptosis induction relative to their control group (set to 100 %). A similar increase was observed in Grx1$^{-/-}$ MEFs, reaching 142.8 ± 26.4 % after CHP treatment compared to their respective control group, which was set to 100 % (**Figure 26**).

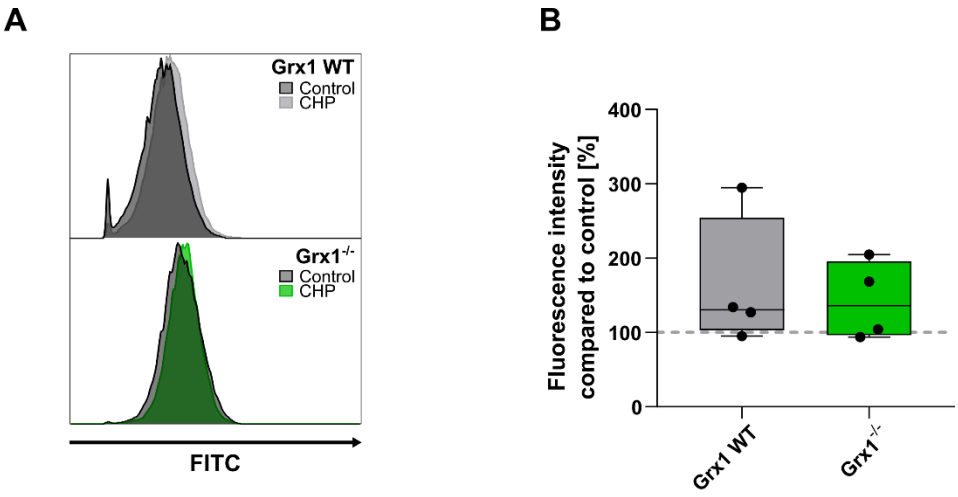

Figure 26: Impact of Grx1$^{-/-}$ on lipid peroxidation accumulation

(A) The fluorescence intensity of oxidized BODIPY C11 was measured by flow cytometry using the FITC detector channel. The representative histogram illustrates the fluorescence shift between untreated control groups and those exposed to ferroptosis induction with CHP (32 µM). **(B)** The box-whisker plot displays the mean fluorescence intensity, with the gray dotted line representing the untreated control. Black dots indicate individual values from n = 4 after CHP treatment.

To test the effect of Grx1 in human cells, HeLa cells were transfected with control siRNA (siCtrl) or Grx1 siRNA (siGrx1) as described in **8.2.2**. Transfection with siGrx1 were used to silence expression of Grx1, where unspecific siRNA (siCtrl) was used as control. The silenced expression of Grx1 in these cells was confirmed by a representative western blot (**Figure 27 A**). The impact of the knockout of Grx1 via siRNA on ferroptosis was investigated by inducing ferroptosis using 32 µM Erastin and afterwards measuring lipid peroxidation using BODPY C11 and flow cytometry analysis as indicated in **8.2.4**. The analysis revealed no clear differences between siCtrl HeLa and siGrx1 HeLa.

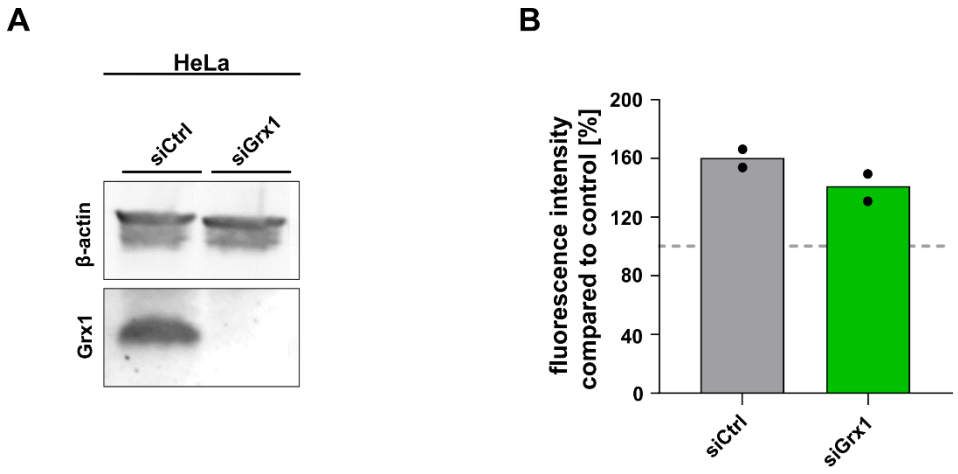

Figure 27: Grx1 expression and lipid peroxidation accumulation in HeLa lacking Grx1

(A) The representative western blot shows Grx1 protein expression in HeLa cells transfected with siCtrl or siGrx1. β-actin served as a loading control to ensure equal protein loading. **(B)** The bar plot displays the mean fluorescence intensity, with the gray dotted line representing the untreated control. Black dots indicate individual values from n = 2 after treatment with 32 µM Erastin for 6 hours.

9.4 Effect of diroximel fumarat on ferroptosis

In addition to the physiological mechanisms of ferroptosis, the pharmacological regulation of ferroptosis has also been investigated. Previous data from our group demonstrated protective effects of diroximel fumarat (DRF) – a pharmaceutical agent used to treat multiple sclerosis – on erastin-induced myelin damage in mice and oligodendrocyte survival in rats. Furthermore, an increase in the expression level of GPX4, along with an increase in the transcription rates of heme oxygenase (HMOX) and GPX4 encoding genes, was observed in rat oligodendrocytes treated with DRF and in MS patients treated with dimethyl fumarat (DMF) – the precursor of DRF, with an identical active ingredient.

To reveal whether these findings are specific for autoimmune diseases within the central nervous system, rheumatoid arthritis (RA) and osteoarthritis (OA) were utilized as additional disease models. Immunohistochemistry was performed on synovial tissues derived from RA and OA patients, which were provided by Torsten Lowin from the Clinic for Rheumatology at University Clinic Düsseldorf. The level of lipid peroxidation accumulation in these tissues was measured by staining for 4-HNE as delineated in **8.2.15**. The results of the immunohistochemistry revealed elevated levels of lipid peroxidation in

tissues derived from OA patients, as evidenced by the pronounced 4-HNE-signal. In the case of RA tissues, 4-HNE accumulation was also observed, though it was less pronounced compared to that seen in OA tissues (**Figure 28**).

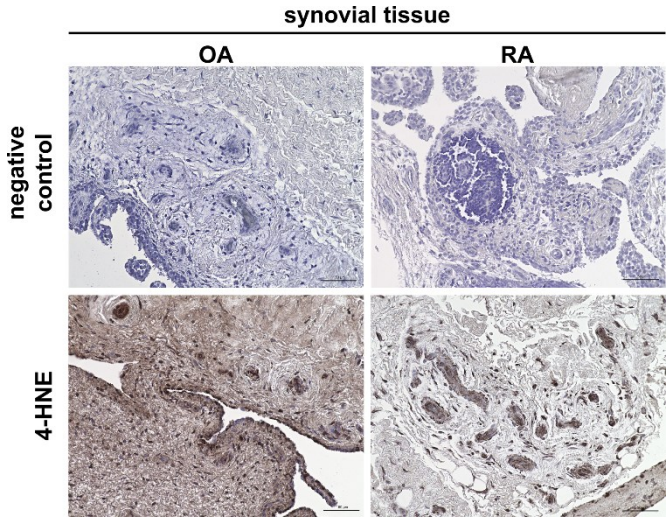

Figure 28: 4-HNE staining in synovial tissue from OA and RA patients

Representative microscopy images of synovial tissue sections from OA patients (left) and RA patients (right) are shown. Immunohistochemical staining was performed using a 4-HNE antibody (brown), with hematoxylin counterstaining (blue) to visualize tissue structure. The upper row represents the negative control.

To investigate potential effects of DRF on lipid peroxidation in RA and OA, further experiments were conducted using osteoarthritis synovial fibroblasts (OASF) and rheumatoid arthritis synovial fibroblast (RASF) provided by Torsten Lowin from the Clinic for Rheumatology at University Clinic Düsseldorf. The induction of inflammation in these cells was achieved through a TNFα (10 ng/ml) treatment for 72 h. Subsequently, the cells were exposed to DRF (2 µM) or monomethyl fumarate (MMF) (2 µM), the active metabolite of DRF, for a duration of 3 h. The accumulation of lipid peroxidation was determined using BODIPY C11 and flow cytometry as outlined in **8.2.4**.

Treatment of OASF with DRF resulted in a minor decrease in lipid peroxidation to 85.3 ± 3.4 %, compared to the control group, which was set to 100 %. MMF treatment resulted in a lipid peroxidation decrease to 80.5 ± 2.9 % compared to the control group (**Figure 29 A-B**). The experiment was repeated with RASF, yielding a minor decrease in lipid peroxidation to 87.0 ± 6.8 % following DRF treatment and to 74.0 ± 3.4 % following MMF treatment. These values were compared to the untreated control, which was set to 100 % (**Figure 29 C-D**).

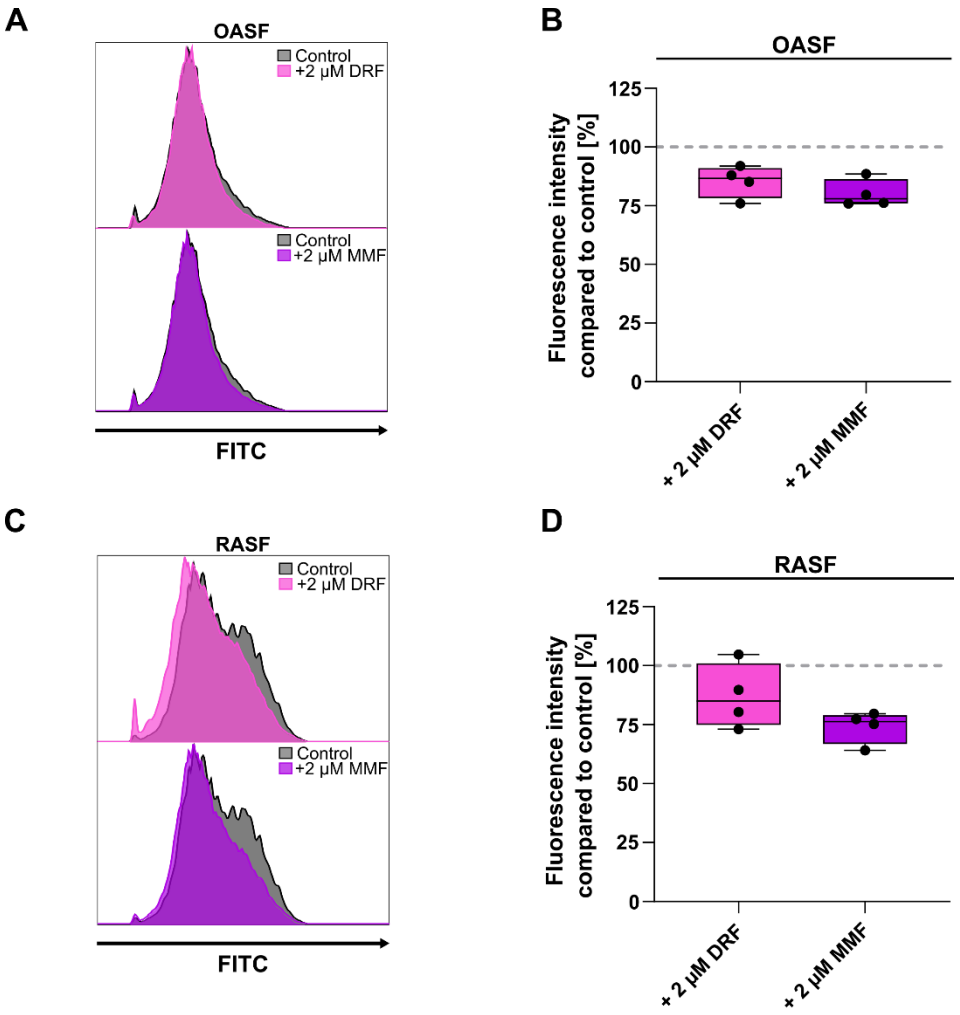

Figure 29: Effect of DRF and MMF on lipid peroxidation in OASF and RASF

(A) The fluorescence intensity of oxidized BODIPY C11 in OASF was measured by flow cytometry in the FITC detector channels. A representative histogram shows the fluorescence shift between OASF control groups (gray) and those exposed to DRF (2 µM) (pink) and MMF (2 µM) (purple). **(B)** A box-whisker plot shows the mean intensity of the fluorescence in OASF. The gray dotted line indicates the control group. Black dots indicate individual values from n = 4. **(C)** Similar to (A), fluorescence intensity of oxidized BODIPY C11 was assessed by flow cytometry, showing the shift in fluorescence between control RASF and DRF-treated samples (2 µM) or MMF-treated cells (2 µM) in a representative histogram. **(D)** A box-whisker plot displays the fluorescence intensity in RASF detected in the FITC detector channel. The gray dotted line represents the control. Black dots indicate individual values from an n = 4.

Given the absence of a substantial protective effect of DRF on lipid peroxidation in OASF and RASF cells, DRF was subsequently examined in terms of cell viability subsequent to ferroptosis induction with CHP. To this end, the cells were exposed to TNFα, as previously described, and then treated with DRF (2 µM and 10 µM) for 3 h. Following the pre-treatment, ferroptosis was induced by subjecting the cells to increasing concentrations of CHP (0.1 µM – 100 µM), in combination with or without the addition of DRF. Cell viability was subsequently assessed as outlined in **8.2.3**. The analysis of cell survival of OASF revealed no significant differences between control OASF, with an IC_{50} value of 14.5 ± 1.5 µM, and OASF treated with 2 µM DRF (IC_{50} value of 13.6 ± 0.9 µM) or 10 µM DRF (IC_{50} value of 9.1 ± 2.5 µM) (**Figure 30 A-B**). A similar trend was measured for RASF. The analysis revealed no significant difference in cell survival between control RASF (IC_{50} value of 11.4 ± 1.7 µM) and RASF treated with 2 µM DRF (IC_{50} value 13.6 ± 1.5 µM) after ferroptosis induction. Treatment of RASF with 10 µM DRF resulted in a minor decrease in cell viability subsequent to ferroptosis induction, yielding an IC_{50} value of 5.7 ± 3.6 µM (**Figure 30 C-D**).

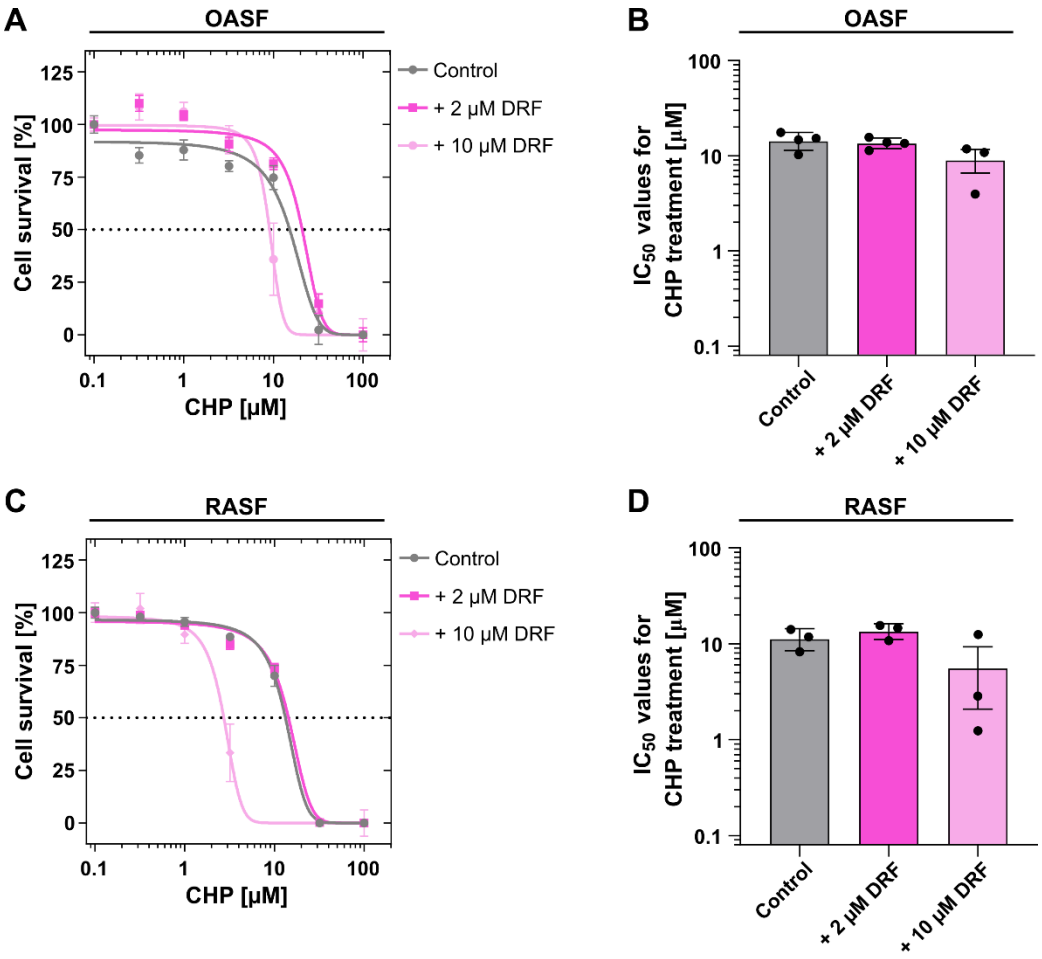

Figure 30: Impact of DRF on OASF and RASF on cell viability after ferroptosis induction

(A) The concentration-response curve illustrates the survival rates of OASF control group (gray), 2 µM DRF-treated OASF (dark pink) and 10 µM DRF-treated OASF (light pink) after ferroptosis induction with increasing CHP concentrations (0.1 µM – 100 µM). Mean values (Control and + 2 µM DRF: n = 4; + 10 µM DRF: n = 3) and the standard error of the mean are shown. **(B)** A bar plot represents the IC_{50} values for all three groups. Black dots indicate individual IC_{50} values. The mean and standard error of mean are shown. **(C)** The second concentration-response curve shows the survival rates of RASF control group (gray), 2 µM DRF-treated RASF (dark pink) and 10 µM DRF-treated RASF (light pink) in response to ferroptosis induction with increasing concentrations of CHP (0.1 µM – 100 µM). The mean values (n = 3) and the standard error of the mean are presented. **(D)** A bar plot displays the IC_{50} values, with mean and standard error of mean shown. Black dots represent individual IC_{50} values. The trend lines shown in figures A and C are for illustrative purposes only and were not used in further calculations.

To investigate the effects of DRF on anti-ferroptotic proteins and their related gene transcription, qPCR and western blotting were performed using the OASF and RASF.

For qPCR, the cells were first treated with TNFα as previously described, followed by a 3-hour incubation with 2 µM DRF. Afterwards, RNA was extracted from the samples, reverse transcribed into cDNA, and qPCR was conducted as outlined in **8.2.14**. The resulting cycle

threshold (CT) values of *ferritin*, *GPX4* and *HMOX* were correlated with *GAPDH* values. The results from the DRF-treated samples were normalized to the untreated control samples using ΔΔCT. Finally, fold changes were calculated using the formula $2^{-\Delta\Delta CT}$. In OASF, *ferritin* and *GPX4* levels exhibited a slight decrease following DRF treatment, with expression fold changes of 0.69 ± 0.16 for *ferritin* and 0.81 ± 0.19 for *GPX4* compared to the untreated control (set to 1). Conversely, *HMOX* levels demonstrated a pronounced increase, reaching an expression fold change of 10.77 ± 1.81 (**Figure 31 A**). A comparable pattern was observed in RASF. *Ferritin* levels exhibited a slight decline, reaching an expression fold change of 0.66 ± 0.13 relative to the control (set to 1), while *GPX4* levels remained unchanged with an expression fold change of 0.93 ± 0.13. However, *HMOX* transcription level demonstrated a clear increase, with an expression fold change of 5.72 ± 1.05 (**Figure 31 B**).

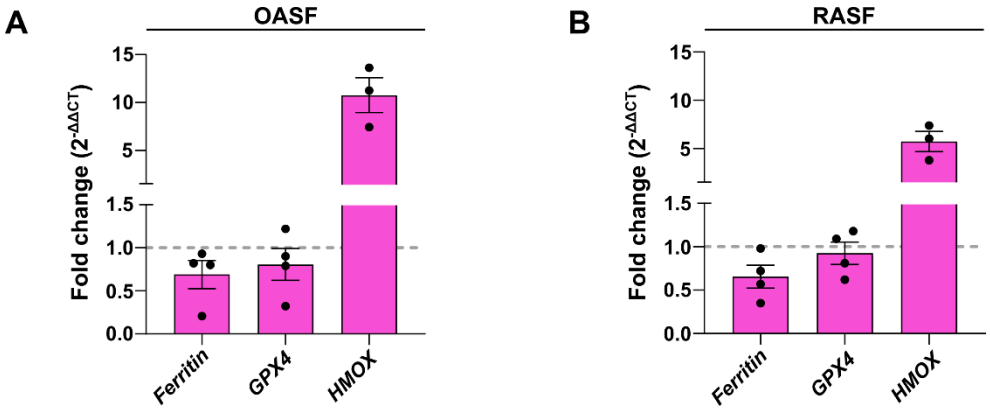

Figure 31: Impact of DRF on gene transcription level in OASF and RASF

(A) The bar plot illustrates the fold change in gene transcription of *ferritin*, *GPX4* and *HMOX* in OASF following treatment with 2 µM DRF, relative to untreated control samples. Mean values and standard error of the mean are displayed, with black dots representing individual data points (*ferritin*, *GPX4*: n = 4; *HMOX*: n = 3). The gray dotted line marks the control level. **(B)** Similarly, the bar plot depicts the fold change in gene transcription of *ferritin*, *GPX4* and *HMOX* in RASF under the same treatment conditions. Mean values, standard error of the mean, and individual data points are presented as in (A), with gray dotted line indicating the control.

For western blot analysis, OASF and RASF were treated with TNFα to induce inflammation as described above. Thereafter, cells were exposed to 2 µM DRF for 3, 6 or

24 hours, or left untreated as a control (0 hours DRF). Subsequently, cells were lysed using NP40 buffer, followed by gel electrophoresis and western blotting as outlined in **8.2.9**. GPX4 protein levels were assessed using a GPX4 antibody and normalized to the corresponding β-actin signal.

In OASF, DRF treatment demonstrated no noticeable effect on GPX4 protein levels. After 3 hours of DRF exposure, the GPX4/β-actin ratio exhibited a value of 1.41 ± 0.49 relative units (RU), and after 6 hours, it exhibited a value of 1.38 ± 0.57 RU compared to the untreated control group (2.20 ± 0.25 RU). Following 24 hours of DRF treatment, a slight decrease in GPX4 levels was observed, reaching 1.18 ± 0.32 RU (**Figure 32 A-B**). Similarly, in RASF, no significant changes in GPX4 levels were detected after DRF treatment. The GPX4/β-actin ratio revealed 1.56 ± 0.35 RU in the untreated control group, 1.33 ± 0.50 RU after 3 hours of DRF, 1.12 ± 0.35 RU after 6 hours of DRF, and 0.98 ± 0.35 RU after 24 hours of DRF (**Figure 32 C-D**).

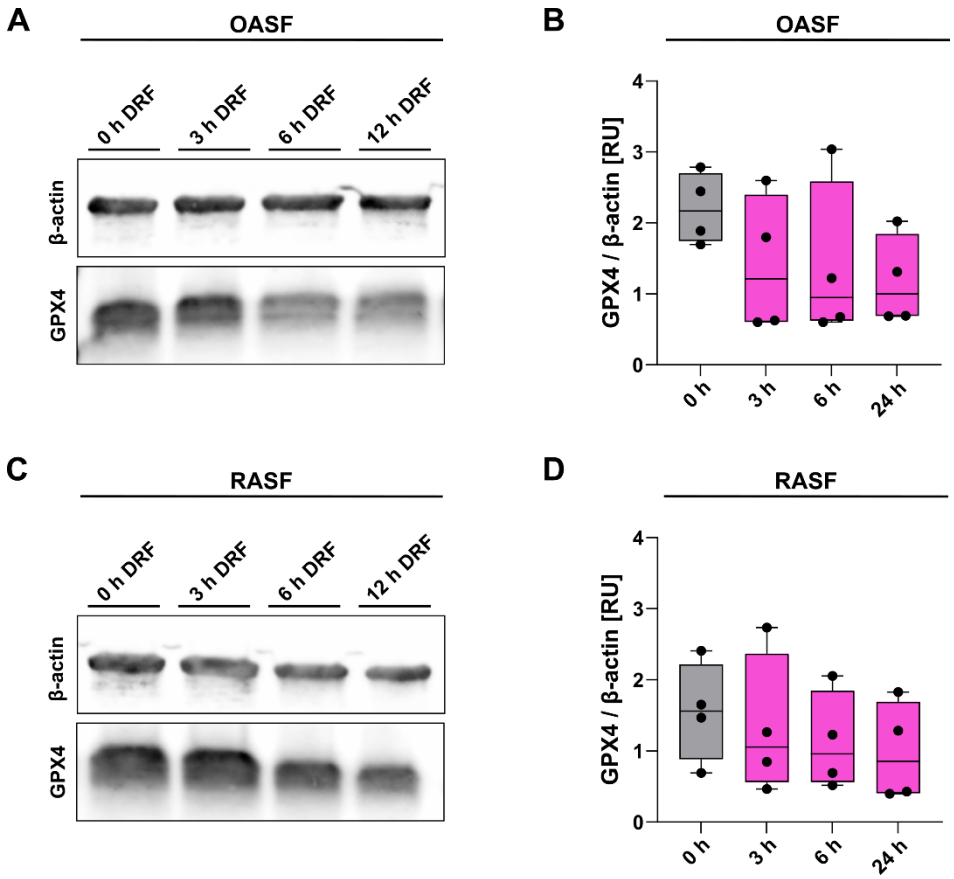

Figure 32: GPX4 protein level in OASF and RASF after DRF treatment

(A) Representative western blot showing GPX4 protein expression in OASF following treatment with 2 µM DRF for 0, 3, 6 or 24 hours. β-actin staining serves as a loading control. **(B)** Box-whisker plot quantifying GPX4 expression in OASF. GPX4 signals were normalized to β-actin and expressed in relative units (RU). Black dots represent individual measurements (n = 4). **(C)** The representative western blot illustrating GPX4 expression in RASF after treatment with 2 µM DRF for 0, 3, 6 or 24 hours. β-actin staining serves as a loading control. **(D)** A box-whisker plot demonstrating GPX4 expression in RASF. GPX4 signals were normalized to their respective β-actin signals and were expressed in RU. Black dots represent individual measurements (n = 4).

10 Discussion

The primary objectives of this study were twofold: firstly, to explore the intracellular regulation of ferroptosis with a focus on redox mechanisms, and secondly, to assess the potential pharmacological modulation of ferroptosis by diroximel fumarate.

Ferroptosis is an iron-dependent form of cell death characterized by lipid peroxidation. To date, GPX4 is the only known mammalian enzyme that can convert toxic lipid peroxides into their corresponding non-toxic alcohols, thereby providing protection against ferroptosis. Although the hallmarks of this process have been observed in several diseases, its cellular regulation remains unclear.

The study's key findings indicate that GPX4 undergoes glutathionylation at cysteine 75, which reduces its binding affinity to phospholipids, ultimately promoting ferroptotic cell death. The study further demonstrates that Grx2 can reverse this modification by de-glutathionylation of cysteine 75, thereby providing protection against ferroptosis. The significance of Grx2 is further highlighted by the increased lipid peroxidation in organs of Grx2-deficient mice and the reduced number of parvalbumin^{+} interneurons in their brains. Another key finding of this study is that diroximel fumarate exhibited no pharmacological effects in osteoarthritis or rheumatoid arthritis and has no regulatory role in ferroptosis.

10.1 Posttranslational modifications

Intracellular processes and interactions are based on signal transduction, such as redox regulation, which is defined by the transfer of electrons [64, 84]. Redox regulation is dependent on reversible oxidative posttranslational modifications of cysteine residues [63]. These modifications are hypothesized to serve a dual purpose. Firstly, they may act as a protective barrier against irreversible oxidation that might otherwise lead to protein degradation. Secondly, they may modulate protein function [85-87]. One type of reversible modification is glutathionylation, which involves the covalent attachment of GSH to cysteine residues. The process of glutathionylation can occur through several mechanisms, including direct oxidation involving a protein and GSH, thiol-disulfide exchange between a protein and GSSG, and via intermediates such as nitrosoglutathione [86, 88]. An example of a protein whose activity is modulated by glutathionylation is thioredoxin. Thioredoxins, which belong to the same protein superfamily as glutaredoxins (see **6.2**), act as electron

donors for various enzymes and are involved in the reduction of disulfide bonds between protein cysteines [64, 89]. Glutathionylation at cysteine 72 of thioredoxin leads to a complete loss of enzyme activity, which can be restored by reducing the glutathionylated cysteine [88].

Another example is hemoglobin, the iron-containing protein complex responsible for oxygen transport in the blood. Glutathionylation on cysteine 93 increases its oxygen affinity and reduces its thermostability [90, 91]. Increased levels of glutathionylated hemoglobin have been detected in type 1 diabetes mellitus, a metabolic disorder based on insulin deficiency and characterized by chronically elevated blood glucose levels [92, 93]. Increased levels of glutathionylated hemoglobin may result in decreased oxygen delivery to tissues due to increased oxygen affinity and resulting impaired oxygen release [92].

A notable example linked to a ferroptosis related protein is ovarian tumor deubiquitinase 1 (OTUB1). This enzyme interacts with SLC7A11, a subunit of system X_C^-, and protects it from ubiquitin-dependent degradation [94]. In an oxidative environment, OTUB1 is glutathionylated at cysteine 23 or 204, which enhances binding to SLC7A11 and thus prevents degradation of system X_C^- [95, 96]. This leads to increased intracellular GSH levels and improved protection against ferroptosis. However, when glutathionylation is reduced, the OTUB1-SLC7A11 interaction becomes unstable, which in turn promotes the ubiquitination and subsequent degradation of SLC7A11 [95]. In 2013, Aboushousha *et al.* demonstrated that this de-glutathionylation is glutaredoxin-dependent, thereby providing further evidence for the physiological regulation of ferroptosis by redox mechanisms [96].

This study revealed the presence of glutathionylation at cysteine 75 of GPX4 (**Figure 5 A**). This modification has been shown to alter the electrostatic surface potential of the protein, resulting in a negative charge in the region encompassing cysteine 75 (**Figure 5 B**). A similar region has previously been described as the possible lipid binding area of GPX4 [97]. Given the established role of posttranslational modifications in influencing proteins in terms of structure, localization, and/or activity, the impact of glutathionylated GPX4 on ferroptosis was investigated [63, 64].

10.1.1 Modulation of ferroptosis via GPX4 C75 glutathionylation

To study the effect of glutathionylation of GPX4 C75, mutant cell lines (MEF GPX4 C75S and MEF GPX4 C75E) were used as they serve as powerful tools to study the effects of glutathionylation. In MEF GPX4 C75S, the cysteine was replaced by serine, thereby preventing glutathione binding. This cysteine-to-serine mutation is a well-established model for studying redox-dependent proteins, as serine cannot be oxidatively modified [98, 99]. Serin and cysteine share similar size and polarity. The two amino acids have the same structure, except that serine contains an oxygen instead of the sulfur present in cysteine. In contrast, MEF GPX4 C75E features a cysteine-to-glutamic acid exchange. Since glutathionylation involves the attachment of GSH – a tripeptide composed of glutamic acid, cysteine, and glycine – glutamic acid was intended to mimic the negative charge introduced during this modification. A similar approach is often used to mimic phosphorylation [100, 101]. However, it has not been used to mimic glutathionylation. MD simulations confirmed this approach, demonstrating that GPX4 C75E exhibits similar electrostatic surface potential distribution as glutathionylated GPX4 cysteine 75, supporting the validity of this model (**Figure 5 B**). The GPX4 cysteine 75 mutations in the MEF cell lines appear to have no effect on the GPX4 protein level or the enzymatic activity, as evidenced by western blot analysis and activity measurements, which exhibited no differences between the three cell lines (MEF GPX4 WT, MEF GPX4 C75S, and MEF GPX4 C75E) (**Figure 8**). Induction of ferroptosis in these cells using different ferroptosis inducers revealed decreased cell survival (**Figure 6**) and increased lipid peroxidation (**Figure 7**) in GPX4 C75E MEFs. This suggests a higher susceptibility to ferroptosis in the cells mimicking the glutathionylated GPX4 cysteine 75.

10.1.2 Membrane interaction of GPX4

GPX4 is ubiquitously expressed in the cytosol of MEFs [3]. However, it must localize to the cellular membrane to interact with the lipid peroxides present there. This localization shift is facilitated by electrostatic interactions between GPX4 and the polar head groups of phospholipids [97, 102]. Furthermore, membrane binding affinity measurements revealed that the GPX4 C75E variant exhibits reduced binding to POPG phospholipids (**Figure 9**). In conjunction with the alterations in electrostatic surface potential surrounding cysteine 75 during glutathionylation, these findings suggest that glutathionylation of cysteine 75

impacts GPX4's membrane interaction, thereby potentially regulating its localization and functionality. Notably, cysteine 75 is located in a region that has been characterized as the lipid-binding site of GPX4 [102].

In addition to cysteine 75, other residues within GPX4 are also critical for membrane binding. It was demonstrated that arginine 152, in conjunction with lysine residues at positions 125 and 135, constitutes a cationic area that facilitates phospholipid interaction via double salt bridges. The substitution of arginine 152 with histidine (GPX4 R152H) has been shown to significantly diminish electrostatic attraction, attributable to the reduced positive charge of histidine [97, 102]. This GPX4 mutation has been identified in patients with sedaghatian-type spondylometaphyseal dysplasia (SSMD), a rare, neonatal-lethal disorder first described in 1980 [103]. SSMD is characterized by cardiorespiratory failure and central nervous system malformations [104, 105]. In 2022, Liu *et al.* revealed that the R152H variant destabilizes a critical loop that is essential for maintaining the active site. This destabilization results in a significant loss of enzymatic activity [105]. Although the precise pathophysiological mechanisms remain incompletely understood, current evidence suggests that the severe clinical manifestations of SSMD result from near-total GPX4 inactivation [105]. In subsequent MD simulations, conducted in collaboration with Yana Bodnar and Christopher Horst Lillig at the Institute for Medical Biochemistry and Molecular Biology at University Medicine Greifswald, it was observed that glutathionylation at cysteine 75 of GPX4 increases the number of hydrogen bonds between arginine 152 and a loop from 2 to 3, thereby affecting the binding affinity to membranes.

Taken together, these results emphasize the critical importance of precise electrostatic interactions and membrane association for the functionality of GPX4 and illustrate the severe physiological impact of their impairment.

10.1.3 Posttranslational modifications of other ferroptotic enzymes

In addition to glutathionylation, further posttranslational modifications can also influence protein structures and thereby regulate cellular processes. Examples of further posttranslational modifications include phosphorylation, ubiquitination, and lipidation. Phosphorylation involves the addition of a phosphate group, while ubiquitination refers to the attachment of the small protein ubiquitin to a target protein. Lipidation is defined as the covalent attachment of lipid molecules to proteins. This modification encompasses several

subtypes, including palmytoylation, in which palmitic acid is added, and myristoylation, in which myristic acid is attached to the protein. These modifications were already described as regulators of degradation of ferroptosis-related proteins [3].

For example, GPX4 can be ubiquitinated, leading to its subsequent degradation by the proteasome system. This, in turn, results in a decreased level of GPX4 and thereby sensitizes cells to ferroptosis [106]. The protein homeostasis of GPX4 can be regulated by the phosphorylation of serine 104. This phosphorylation prevents the degradation of GPX4, which is targeted by chaperone-mediated autophagy [107]. Another modification that has been shown to stabilize GPX4 is linear ubiquitination by the HOIL-interacting protein (HOIP). Linear ubiquitination is a distinct type of ubiquitination that involves attaching a polyubiquitin chain to a substrate protein [108]. HOIP has been demonstrated to play a role in the linear ubiquitin chain assembly complex (LUBAC), while deficiencies of this complex have been found to render cells more sensitive to ferroptosis [109, 110].

Other ferroptosis-related proteins, such as SLC7A11 and FSP1, are also regulated by posttranslational modifications. SLC7A11, for instance, has been observed to undergo ubiquitination, a process that ultimately results in its degradation and, consequently, the breakdown of system X_C^- [96]. Conversely, SLC7A11 can undergo palmytoylation by adding palmitic acid to cysteine 327. This modification has been shown to reduce ubiquitination, thereby stabilizing system X_C^- [111]. A similar mechanism involving ubiquitination and subsequent protein degradation has been observed in the case of FSP1 [112]. However, the posttranslational modifications previously discussed exclusively influence protein levels through the processes of degradation or stabilization. The only posttranslational modification with a direct physiological role in ferroptosis is the myristoylation of FSP1. Myristoylation at the N-terminus of FSP1 localizes it to the cell membrane, enabling the regeneration of oxidized CoQ_{10}. Reduced CoQ_{10} has been shown to scavenge lipid peroxyl radicals, thereby disrupting the autooxidation chain reaction that would otherwise lead to lipid peroxide accumulation [34, 113].

In summary, our understanding of posttranslational modifications in ferroptosis-related proteins has been largely limited to their roles in protein degradation or stabilization, thereby maintaining protein levels. The posttranslational modification presented here – glutathionylation of GPX4 – demonstrates, for the first time, a regulatory mechanism in the cellular environment. Specifically, glutathionylation of cysteine 75 leads to a more negative

surface potential of GPX4, resulting in decreased binding affinity to cellular membranes and impaired enzymatic functionality. A summary of the mentioned proteins with their posttranslational modifications found so far, including the GPX4 glutathionylation demonstrated in this work, is shown in **Figure 33**.

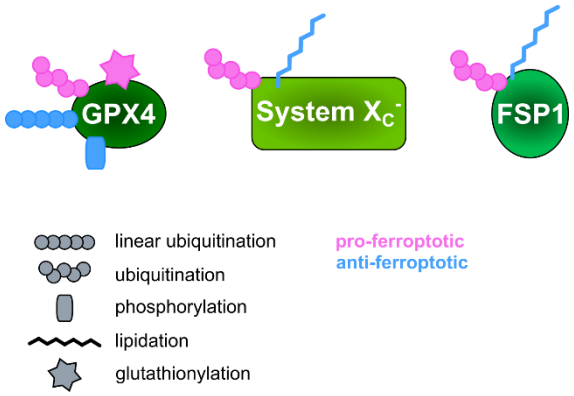

Figure 33: Overview of posttranslational modifications on ferroptosis-related proteins

The figure shows GPX4, System X_C^-, and FSP1, along with their known modifications including ubiquitination, linear ubiquitination, phosphorylation, lipidation, and glutathionylation. Each modification is colored according to its effect on ferroptosis: pro-ferroptotic (pink) or anti-ferroptotic (blue). Figure is adapted from [3].

10.2 Glutaredoxin 2 regulates ferroptosis

Redox regulation by posttranslational modifications of cysteine residues is a highly specific process mediated by oxidoreductases such as Grx1 and Grx2. These enzymes are able to reduce reversible modifications such as disulfide bonds and glutathionylation, highlighting their central role in cellular redox homeostasis [68, 71, 73]. The main focus of this thesis was on Grx2. This oxidoreductase has previously been implicated in the reduction of several target proteins, including sirtuin 1 and mitochondrial complex I.

Sirtuin 1 is a NAD^+-dependent deacetylase that plays an essential role in various processes, including cell cycle regulation, energy metabolism, and the aging process. Glutathionylation at cysteine 204 modulates the activity of sirtuin 1 and provides a substrate for Grx2. Grx2-dependent deglutathionylation of this enzyme is critical for vascular development [71, 114].

Complex I is a central component of the mitochondrial respiratory chain and essential for electron transfer from NADH to ubiquinone. This is necessary to generate the proton gradient that drives ATP synthesis. Under oxidative conditions, complex I is glutathionylated, which protects it from irreversible oxidation but also inhibits its activity.

Grx2 can reverse this modification and restore the functionality of the enzyme [115]. These examples illustrate that Grx2 is involved in several essential cellular processes.

This work demonstrates an important role of Grx2 in regulating ferroptosis. A knockout of Grx2 in MEFs decreases cell survival (**Figure 13**) and increases lipid peroxidation after ferroptosis induction (**Figure 14**), leading to the assumption that Grx2 deficient cells are more sensitive to ferroptosis. GPX4 seems to serve as a substrate for Grx2, since Grx2 is able to de-glutathionylate GPX4 cysteine 75 (**Figure 11**). Furthermore, this cysteine appears to be more oxidized in HeLa cells lacking Grx2, as demonstrated in a 2018 study using mass spectrometry documented in the dissertation of Daniel Trnka from the University of Greifswald [116]. Since the GPX4 (**Figure 15**) and GSH (**Figure 16**) levels in Grx2 deficient cells are already elevated under basal conditions, this could indicate a possible attempt to compensate the diminished protective function of GPX4, which would explain why the cells survive without targeted ferroptosis induction.

GPX4 is less glutathionylated under stressed conditions, e.g. by increased lipid peroxidation due to CHP treatment, demonstrating again the importance of a reduced cysteine 75 for protection against ferroptosis (**Figure 10**). This indicates that Grx2 de-glutathionylates GPX4 upon induction of ferroptosis.

Grx2 has been described as a potential redox sensor, given that its function can be modulated by the cellular redox environment [74]. Under normal conditions, i.e. at high intracellular concentrations of GSH, Grx2 is present in an inactive form. This inactivity is mediated by the coordination of an iron-sulfur cluster of two Grx2 molecules [74, 75]. The cluster is coordinated by four ligands: two active site cysteine residues and the cysteine residues of two molecules of GSH. These GSH molecules are in constant exchange with GSH in the environment [75]. Therefore, the stability of the cluster is directly dependent on the GSH concentration [75]. However, under oxidative stress, when the GSH concentration decreases and GSSG increases, the cluster is destabilized. This leads to the disassembly of the iron-sulfur cluster and the generation of active Grx2 monomers [74, 75].

This mechanism is particularly relevant in the context of ferroptosis. In ferroptotic cells, oxidative stress prevails, GSH is greatly reduced, and GSSG is increased [117, 118]. These conditions lead to the disassembly of the iron-sulfur cluster, thereby promoting the

activation of Grx2 [74, 117]. Reactivated Grx2 can then reduce glutathionylated cysteine 75 of GPX4, thereby restoring GPX4 functionality and inhibiting ferroptosis.

10.2.1 Importance of glutaredoxin 2 in the mouse organs

As previously mentioned, Grx2 plays a role in a variety of cellular processes. Its physiological relevance is also evident in various organs, for example in the brain. Grx2 has been demonstrated to impact the survival of primary oligodendrocyte progenitor cells and the maintenance of myelin structure in cerebellar organotypic slice cultures. These functions appear to have pathological significance, as mice with experimental autoimmune encephalomyelitis – a commonly used model for multiple sclerosis – exhibit reduced expression levels of Grx2 [76].

The findings presented in this thesis further support the importance of Grx2 in murine brain tissue. The knockout of Grx2 in mice has been shown to result in increased lipid peroxidation in the brains of adult animals (**Figure 18**) and a decrease in the number of parvalbumin-positive (PV^+) interneurons (**Figure 20**). PV^+ neurons are a type of GABAergic interneuron that play a pivotal role in modulating the excitability of neuronal networks through the repression of excessive neuronal activity. As has been previously established, Grx2 is typically found to be highly upregulated in interneurons, including Purkinje cells, which also express parvalbumin [118, 119]. Interestingly, alterations in parvalbumin expression are strongly associated with epilepsy [120]. Epilepsy is one of the most disabling chronic neurological disorders, characterized by epileptic seizures due to abnormal excessive or synchronous neuronal activity in the brain [121]. The loss of PV^+ interneurons may result in increased neuronal activity, thereby elevating the risk of epileptic seizures. And indeed, brain slices from $Grx2^{-/-}$ mice showed increased neuronal activity as evidenced by a higher firing rate compared to those from WT mice as measured by microelectrode array (MEA) (**Figure 34**). MEA recordings from WT and $Grx2^{-/-}$ mouse brains were kindly performed and provided by colleagues Paul Disse and Lara-Maria Preuth. The data demonstrates that neuronal activity is elevated in $Grx2^{-/-}$ mice, both upon exposure to varying concentrations of potassium chloride (KCl) and after incubation with 4-aminopyridine (4-AP). In MEA experiments, KCl is typically used to assess general neuronal excitability by increasing the extracellular potassium concentration. This increase in potassium concentration depolarizes neuronal membranes and facilitates the initiation of

action potentials [122]. In contrast, 4-AP has been demonstrated to induce hyperexcitability by blocking potassium channels, thereby slowing neuronal repolarization and promoting longer and more frequent action potentials [123].

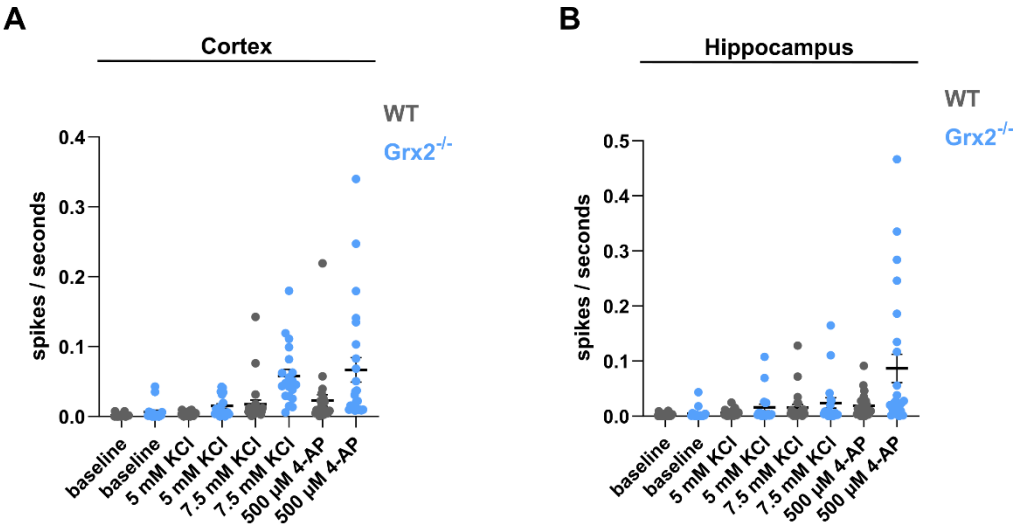

Figure 34: Neuronal activity in brain slices of WT and Grx2$^{-/-}$ mice

The figure shows neuronal activity, measured in spikes per second, in brain slices from WT mice (gray dots) and Grx2$^{-/-}$ mice (blue dots). Recordings were made using a microelectrode array (MEA). Measurements and data analysis were performed by Paul Disse and Lara-Maria Preuth, who kindly provided the data. KCl incubation was used to induce general neuronal excitability, whereas 4-AP treatment was used to promote neuronal hyperexcitability. **(A)** shows recordings from the cortex, while **(B)** shows recordings from the hippocampus. Figures show individual measurements as dots, as well as the mean value (black line) and standard error of the mean (error bar).

A similar phenotype to the above has previously been observed in the brains of GPX4-deficient mice and in mice expressing the GPX4$^{Cys/Cys}$ mutant, a functionally impaired variant [31, 83]. These studies demonstrated that specifically PV^{+} interneurons undergo cell death in the context of GPX4 deficiency or dysfunction, while other neuronal subtypes remain largely unaffected [31, 83]. This leads to the assumption that PV^{+} interneurons appear to be particularly sensitive to ferroptosis. Furthermore, these mice exhibited severe spontaneous epileptic seizures and increased neuronal excitability [31, 83]. The findings of both studies underscore the pivotal function of GPX4 in the survival of PV^{+} neurons and demonstrate that a GPX4-dependent loss of PV^{+} interneurons initiates seizures in mice.

In summary, the loss of Grx2 results in the loss of PV^{+} neurons, which is associated with increased neuronal activity. The observation of analogous outcomes in mice with

insufficient or lost GPX4 activity further underscores the importance of Grx2 in ensuring sufficient GPX4 functionality.

Furthermore, this study indicated an increase in lipid peroxidation in the liver tissues of adult mice lacking Grx2. The liver is the primary organ responsible for iron metabolism, making it particularly susceptible to ferroptosis due to excessive iron levels or impaired iron homeostasis [124]. Ferroptosis has been demonstrated to play a pivotal role in the progression of metabolic dysfunction-associated fatty liver disease (MASLD), as well as in the development of hepatocellular carcinoma. The interest in ferroptosis in liver cancer has been sparked since it was demonstrated that sorafenib – a clinical established compound to treat hepatocellular carcinoma – induces ferroptosis in liver cancer cells. This is a promising approach to treat chemotherapy-resistant liver cancer.

MASLD is a liver disease characterized by an increase in lipid deposition and hepatocyte cell death. MASLD is also known as non-alcoholic fatty liver disease (NAFLD) and is associated with several metabolic disorders including obesity, diabetes and hypertension. Ferroptosis has been found to be a key pathological factor in MASLD patients and ferroptosis inhibition has been identified as a promising therapeutic target [125].

Interestingly, recent studies have shown that depletion of Grx2 induces MASLD in mice [78]. This correlation supports the thesis that Grx2 protects against ferroptosis. Moreover, these findings suggest that Grx2 could serve as a therapeutic approach for diseases in which ferroptosis is implicated.

10.2.2 Role of different isoforms of Grx2 in ferroptosis

One of the morphological characteristics of ferroptosis is a change in the size of the mitochondria [7]. However, the precise function of mitochondria in ferroptosis remains to be fully elucidated [3]. The mitochondrial isoform of GPX4 is predominantly expressed in spermatocytes [3, 28]. Notably, the knockout of mitochondrial GPX4 in mice does not result in developmental disorders or a reduction in life expectancy; but it does lead to male infertility [126]. Furthermore, the lethality resulting from a complete GPX4 knockout can be counterbalanced by cytosolic GPX4, but not by the mitochondrial form [30, 127].

Interestingly, cytosolic GPX4 is detectable in mitochondria, presumably mainly in the intermembrane space (IMS) of mitochondria [30].

Grx2 also has several isoforms, which are distinguished by different subcellular localizations. While Grx2c and Grx2b are present in both the cytosol and nucleus, Grx2a is exclusively restricted to the mitochondria [66, 67]. The existence of these different isoforms and their specific localizations underscores the significance of Grx2 for diverse cellular processes. For instance, Grx2a has been identified as a central redox regulator in mitochondria [78], as evidenced by its role in de-glutathionylation of mitochondrial complex I, as already described in **10.2** [115], whereas the cytosolic isoform is connected to rearrangements of the cytoskeleton [128].

Nevertheless, the present study demonstrates that the overexpression of the mitochondrial Grx2 isoform in HeLa cells results in a comparable protective effect to that observed with the overexpression of the cytosolic Grx2 isoform (**Figure 22** and **Figure 23**). This phenomenon can be attributed to the role of Grx2 in maintaining redox homeostasis within mitochondria [78, 129], the presence of cytosolic GPX4 in the mitochondria [30], and the discussed importance of mitochondrial integrity during ferroptosis [7]. It is also known that increased expression of mitochondrial Grx2 reduces the susceptibility of HeLa cells to apoptosis [79]. The findings of this work indicate that the strongest protective effect of mitochondrial Grx2 overexpression is observed after CHP treatment, rather than after erastin treatment. This suggests that the cells were not exclusively protected against ferroptosis, but also against other forms of cell death, such as apoptosis. This outcome is consistent with the observation that CHP does not function as a specific ferroptosis inducer but rather elevates intracellular oxidative stress levels [130].

10.3 Glutaredoxin 1 has no clear effect on ferroptosis

Next to Grx2, Grx1 also serves as an oxidoreductase and is able to de-glutathionylate cysteine residues, thereby playing an important role in redox regulation [73, 131, 132]. Grx1 is mainly localized in the cytosol, but recent studies suggest that Grx1 can translocate to the cell nucleus [133]. The importance of Grx1 in cell death and diseases was outlined by Liu *et al.* in 2015 [134]. Grx1 was demonstrated to protect against cell death in retinal pigment epithelial (RPE) cells induced by H_2O_2. A loss of RPE cells is predominantly associated with age-related macular degeneration (AMD), a progressive eye disease

occurring due to oxidative damage and inflammation [133]. Grx1 was shown to de-glutathionylate protein kinase B [134]. Protein kinase B plays an important role in cell survival by inhibiting downstream proapoptotic molecules in its active state, thereby protecting the cell from apoptosis [135]. To maintain its active state, it must be phosphorylated at threonine 308 and serine 473. Under oxidative conditions, such as elevated GSSG levels, protein kinase B is glutathionylated. Increased glutathionylation leads to a reduction in phosphorylation, thereby inactivating protein kinase B. Grx1 de-glutathionylates protein kinase B, thereby stabilizing phosphorylation and activating protein kinase B [134].

However, the present thesis shows that a knockout of Grx1 seems to have no impact on protecting cells from ferroptosis since cell survival (**Figure 25**) and lipid peroxidation levels (**Figure 26** and **Figure 27**) after ferroptosis induction were kept unchanged compared to WT cells.

Although Grx1 and Grx2 are structurally related and perform similar functions, they differ in their surface properties. The active site of Grx2 is positively charged, while that of Grx1 is more negatively charged and has a smaller surface area (**Figure 35**) [136]. Since substrate recognition also depends on electrostatic interactions and contact surfaces, this could explain why Grx1 has no effect on ferroptosis. With its positively charged active site, Grx2 may be better able to bind to the negatively charged surface of GPX4, which is formed during glutathionylation (**Figure 5**). This suggests that GPX4 may not serve as a substrate for Grx1. However, this needs to be confirmed in further experiments. In summary, this indicates that Grx2 is a specific regulator of ferroptosis mechanisms.

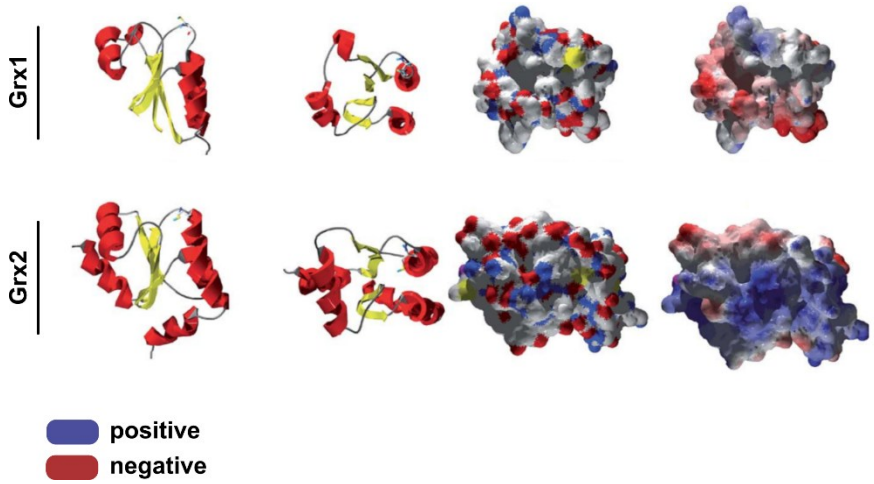

Figure 35: Electrostatic surface potential of Grx1 and Grx2

The figure shows the structures and surfaces of Grx1 and Grx2. The first and second columns show the secondary structure at different angles. The third column shows the surface of the active site and potential contact areas in atomic type coloring. The fourth column shows the electrostatic surface potentials mapped onto the surface, with red representing negative charge and blue representing positive charge. The figure is adapted from [136].

10.4 Relevance of ferroptosis in diseases

As already mentioned, ferroptosis plays a pivotal role in the development of diseases. Hallmarks of ferroptosis have been identified in diverse pathological conditions, including I/R injury, Alzheimer's disease, Parkinson's disease, and Multiple Sclerosis [3]. The inhibition of ferroptosis is therefore of particular interest for research into possible therapeutic approaches to halt the progression of the disease. On the other hand, the induction of ferroptosis is also being investigated as a possible therapeutic approach to induce ferroptotic cell death in cancer cells [3, 137].

10.4.1 Fumarate as therapeutic agents

Fumarates – especially in the form of dimethyl fumarate (DMF) or monomethyl fumarate (MMF) – were established in recent years as promising therapeutic agents in various disease areas, primarily due to their immunomodulatory and antioxidant properties [138]. A particularly potent candidate is diroximel fumarate (DRF) (Trade name: Vumerity®), which is a refined version of DMF with improved tolerability. DRF is better tolerated in the gastrointestinal than DMF because of its unique chemical structure, resulting in lowered

methanol production [139, 140]. However, both DRF and DMF share the active metabolite MMF [139].

Previous studies have demonstrated a stimulatory effect of diroximel fumarate on the NRF2 pathway [141]. The NRF2 transcription factor coordinates the expression of several antioxidant genes and has been reported to promote cell survival under oxidative stress through multiple mechanisms, thus playing a critical role in the regulations of redox homeostasis [142, 143]. Under physiological conditions, NRF2 is targeted for degradation by Kelch-like ECH-associated protein 1 (KEAP1)-mediated ubiquitination. However, under oxidative conditions, cysteines of KEAP1 get modified, resulting in suppression of ubiquitination and stabilization of NRF2 [3]. Stabilization of NRF2 results in increased cystine influx and increased GSH synthesis due to increased expression of system X_C^- and γ-GCL [144, 145]. NRF2 is also involved in iron metabolism by regulating ferritin levels and heme oxygenase (HMOX) levels [146]. Increased expression of ferritin results in a reduced amount of labile iron, but increased expression of HMOX is associated with heme degradation, which releases the labile iron [147, 148]. Due to the different effects on iron metabolism, the role of NRF2 in ferroptosis is not yet fully understood, as activation of NRF2 can have both protective (less labile iron) and promoting (more labile iron) effects on ferroptosis.

DRF has been identified as a pharmaceutical agent for the treatment of multiple sclerosis. However, current literature on its protective mechanism remains limited. Given the recognition of ferroptosis characteristics in multiple sclerosis pathology, the relationship between DRF, ferroptosis, and multiple sclerosis was investigated and is described as part of the manuscript in **1.1.2**. In this manuscript it was shown that DRF protects myelin structures of mouse cerebellar slice cultures and OLN93 cells, an oligodendroglial cell line derived from rat brain, against ferroptotic damage. Moreover, it was shown that treatment with DRF for 3 hours leads to an increase in transcripts of anti-ferroptotic genes such as *FSP1*, *SLC7A11* and *GPX4* in OLN93. This manuscript also demonstrates that the predecessor of DRF, DMF, elevates GPX4 levels in the blood of patients with multiple sclerosis. These findings suggest that DRF may exert a protective effect against ferroptosis in multiple sclerosis.

10.4.2 Diroximel fumarate has no impact on ferroptosis in rheumatoid and osteoarthritis

The present study aimed to examine the specificity of the drug by investigating its effects on osteoarthritis and rheumatoid arthritis samples, since it has been demonstrated that both of these conditions manifest an autoimmune and inflammatory pattern, similar to that observed in multiple sclerosis.

High levels of lipid peroxidation were detected in samples from osteoarthritis (OA) and rheumatoid arthritis (RA) patients, consistent with previous findings [149] (**Figure 29** and **Figure 28**).

Treatment of RASF and OASF cells with DRF did not improve cell viability (**Figure 30**) and showed only a minimal effect on the accumulation of lipid peroxidation (**Figure 29**). Despite the established sensitivity of these cells to ferroptosis, DRF did not offer protection against this form of cell death. However, a notable finding was the significant upregulation of *HMOX* expression following treatment (**Figure 31**). This finding suggests that diroximel fumarate activates the NRF2 pathway, given that *HMOX* is a well-known downstream target of NRF2 [150, 151]. However, the mRNA levels of *GPX4* and *ferritin*, as well as the protein level of GPX4, remained unchanged, or even downregulated after treatment (**Figure 31** and **Figure 32**). This finding is in contrast to the existing literature as ferritin is generally described as being regulated in an NRF2-dependent manner [152, 153]. In contrast, the regulation of GPX4 remains highly controversial. While some studies suggest that GPX4 is regulated by NRF2 [154], this appears unlikely due to the absence of structural *cis*-elements in its promoter region [3, 155]. Other sources propose that GPX4 expression is regulated posttranscriptionally via guanine-rich sequence-binding factor 1 (GRSF1), as a knockdown of GRSF1 has been shown to reduce GPX4 levels [3, 156]. The results presented in this study cannot be clearly classified. On the one hand, NRF2 activation by diroximel fumarate is supported by the observed upregulation of *HMOX*. On the other hand, the lack of change in *ferritin* levels challenges this interpretation, casting doubt on the extent of NRF2 activation.

The data presented here demonstrate a discrepancy between the effects of DRF in OA and RA samples, and those observed in rodent brain and oligodendrocyte samples. This finding suggests that the regulation of DRF and NRF2 might be cell type- and/or disease-specific.

11 Physiological and pharmacological regulation of ferroptosis - Outlook

The thesis revealed that ferroptosis can be regulated by reversible posttranslational modifications. Glutathionylation at cysteine 75 of GPX4 results in impaired membrane binding affinity, thereby impairing the functionality of GPX4. The oxidoreductase Grx2 was identified as a substrate for GPX4 and demonstrated a unique function in the prevention of ferroptosis. This process involves the reduction of glutathionylation at GPX4 cysteine 75, resulting in the restoration of membrane binding and the functional capacity of GPX4. Based on these findings, several promising perspectives for further research emerge.

A fundamental question emerges from the existence of the glutathionylation possibility of GPX4: Why does GPX4 possess the capacity to lose its positive charge at the lipid binding site by glutathionylation of cysteine 75? This process appears to be counterintuitive, as a permanent positive charge would be functionally beneficial for efficient membrane association. This raises the question of whether GPX4 has other cellular functions that require GPX4 to be no longer bound to the membrane. Therefore, it seems promising to investigate whether GPX4 in glutathionylated form preferentially converts alternative substrates or binds specific interaction partners.

Furthermore, the spectrum of posttranslational modifications that could affect GPX4 is not yet fully known. In addition to the known ubiquitination and phosphorylation, other modifications could potentially influence the function, localization, or stability of GPX4.

Another key aspect is the role of Grx2. The existing data shows that GPX4 is a substrate for Grx2, and that Grx2 exerts a protective effect against ferroptosis through its ability to de-glutathionylate GPX4 C75. However, further investigation is necessary to ascertain whether Grx2 also regulates other, potentially novel substrates in the context of ferroptosis. Notably, redox-sensitive enzymes involved in lipid metabolism or iron homeostasis may also be regulated by Grx2. While there has been no clear effect of Grx1 on ferroptosis, further investigation is warranted, particularly with regard to other oxidoreductases such as thioredoxins, which may offer alternative avenues for investigation in this field.

These regulatory mechanisms provide potential approaches for therapeutic intervention. For example, targeted modulation of Grx2 expression may have clinical implications for disease progression. Upregulation of Grx2 in multiple sclerosis patients could protect cells

from ferroptotic cell death and thus have neuroprotective effects. Conversely, targeted downregulation of Grx2 in tumor cells could specifically induce ferroptosis, which could promote cell death in cancer cells and thus represent a promising therapeutic principle.

In addition, the results of this thesis provide new insights into the effect of DRF in the context of ferroptosis-associated diseases and indicate a cell-type-specific mode of action for the compound. While a NRF2 activation was detected by the upregulation of *HMOX* in RASF and OASF cells, there was no protective effect against ferroptosis – an unexpected finding given the known role of NRF2 in the induction of antioxidative protective mechanisms. In particular, the absence of regulation of *GPX4* and *ferritin* despite NRF2 activation introduces a paradox that needs to be further explored in future studies.
One potential explanation for this observation could be the cell type specificity of DRF, as observed in OLN93 cells, where in addition to *HMOX*, *ferritin* and *GPX4* were highly upregulated. This observation underscores the importance of analyzing the effect of NRF2 stimulators not in a generalized manner but differentiated by cell type and disease.

In summary, the present thesis highlights two aspects of ferroptosis regulation and paves the way towards further research in this field. Firstly, it underscores the role of posttranslational modifications as a previously underappreciated physiological layer of control, revealing new insights into how ferroptotic cell death is regulated at the molecular level. The extension of these findings to include additional modifications, enzymes, and cellular contexts holds promise for a more profound comprehension of ferroptosis and its biological significance. Secondly, the present study explores the pharmacological potential of DRF as an anti-ferroptotic drug. Although DRF acts as a potential NRF2 activator, its effectiveness is highly dependent on the cellular context. The varying effects on different cell types and disease models make further research into both the molecular mechanisms and the therapeutic relevance essential and show that DRF cannot yet be considered as an established ferroptosis inhibitor.

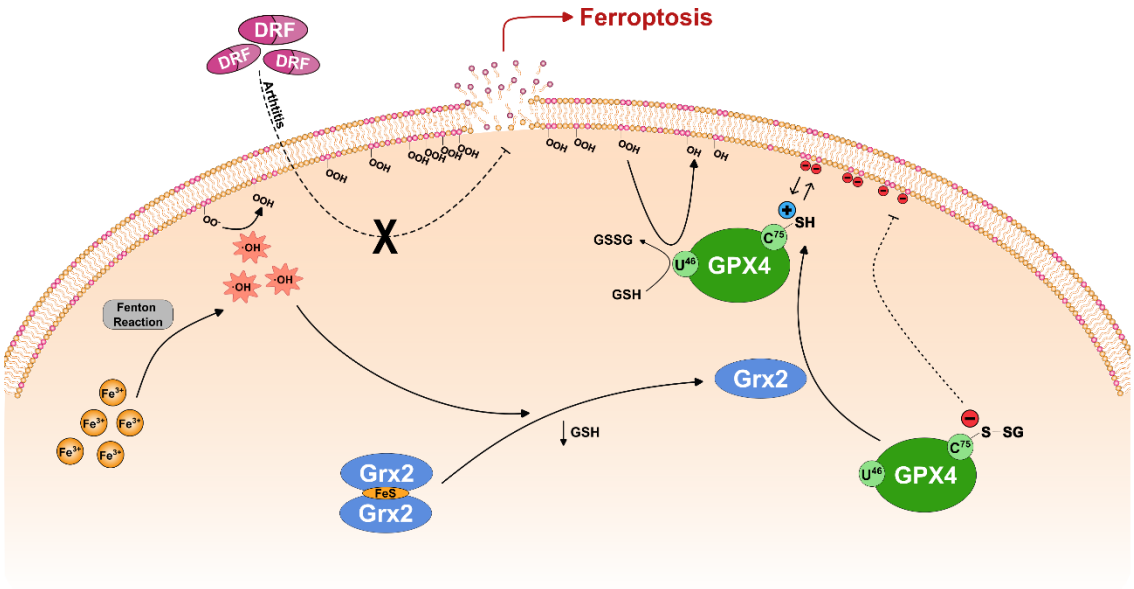

Figure 36: Physiological and pharmacological regulation of ferroptosis

The figure illustrates the physiological and pharmacological mechanisms of ferroptosis regulation as demonstrated in this thesis. Ferroptosis is an iron-dependent form of cell death caused by the accumulation of lipid peroxides. The enzyme GPX4 reduces these lipid peroxides to non-toxic lipid alcohols, thereby preventing ferroptosis. Under physiological conditions, GPX4 is glutathionylated at cysteine 75 (C75), resulting in a negatively charged surface potential and impaired membrane binding. Under stress conditions, characterized by elevated levels of hydroxyl radicals and low levels of GSH, the protein Grx2 loses its iron-sulfur cluster and regains its oxidoreductase activity. This allows Grx2 to de-glutathionylate GPX4 at C75, resulting in a shift in surface potential to a more positively charged state. As a result, GPX4 can associate more effectively with the cell membrane, which is essential for detoxification of lipid peroxides and protection against ferroptosis. On the pharmacological side, the compound DRF showed no effect on the progression of ferroptosis in models of rheumatoid arthritis and osteoarthritis.

12 References

1. Galluzzi, L., et al., *Molecular mechanisms of cell death: recommendations of the Nomenclature Committee on Cell Death 2018.* Cell Death Differ, 2018. **25**(3): p. 486-541.

2. Galluzzi, L., et al., *Essential versus accessory aspects of cell death: recommendations of the NCCD 2015.* Cell Death Differ, 2015. **22**(1): p. 58-73.

3. Berndt, C., et al., *Ferroptosis in health and disease.* Redox Biol, 2024. **75**: p. 103211.

4. Kerr, J.F., A.H. Wyllie, and A.R. Currie, *Apoptosis: a basic biological phenomenon with wide-ranging implications in tissue kinetics.* Br J Cancer, 1972. **26**(4): p. 239-57.

5. Suzanne, M. and H. Steller, *Shaping organisms with apoptosis.* Cell Death Differ, 2013. **20**(5): p. 669-75.

6. Vanden Berghe, T., et al., *Regulated necrosis: the expanding network of non-apoptotic cell death pathways.* Nat Rev Mol Cell Biol, 2014. **15**(2): p. 135-47.

7. Dixon, S.J., et al., *Ferroptosis: an iron-dependent form of nonapoptotic cell death.* Cell, 2012. **149**(5): p. 1060-72.

8. Li, J., et al., *Ferroptosis: past, present and future.* Cell Death Dis, 2020. **11**(2): p. 88.

9. Wiernicki, B., et al., *Excessive phospholipid peroxidation distinguishes ferroptosis from other cell death modes including pyroptosis.* Cell Death Dis, 2020. **11**(10): p. 922.

10. Muckenthaler, M.U., et al., *A Red Carpet for Iron Metabolism.* Cell, 2017. **168**(3): p. 344-361.

11. Galy, B., M. Conrad, and M. Muckenthaler, *Mechanisms controlling cellular and systemic iron homeostasis.* Nat Rev Mol Cell Biol, 2024. **25**(2): p. 133-155.

12. Reichert, C.O., et al., *Ferroptosis Mechanisms Involved in Neurodegenerative Diseases.* Int J Mol Sci, 2020. **21**(22).

13. Fenton, H.J.H., *Oxidation of tartaric acid in presence of iron.* Journal of the Chemical Society, Transactions, 1894. **65**: p. 899-910.

14. Muckenthaler, M.U., B. Galy, and M.W. Hentze, *Systemic iron homeostasis and the iron-responsive element/iron-regulatory protein (IRE/IRP) regulatory network.* Annu Rev Nutr, 2008. **28**: p. 197-213.

15. Anderson, C.P., et al., *Mammalian iron metabolism and its control by iron regulatory proteins.* Biochim Biophys Acta, 2012. **1823**(9): p. 1468-83.

16. Dai, Y., H. Tang, and S. Pang, *The Crucial Roles of Phospholipids in Aging and Lifespan Regulation.* Front Physiol, 2021. **12**: p. 775648.

17. Qiu, B., et al., *Phospholipids with two polyunsaturated fatty acyl tails promote ferroptosis.* Cell, 2024. **187**(5): p. 1177-1190 e18.

18. Harayama, T. and H. Riezman, *Understanding the diversity of membrane lipid composition.* Nat Rev Mol Cell Biol, 2018. **19**(5): p. 281-296.

19. Cai, Z., *Lipid Peroxidation*, in *Encyclopedia of Toxicology*, P. Wexler, Editor. 2005, Elsevier. p. 730-734.

20. Yin, H., L. Xu, and N.A. Porter, *Free radical lipid peroxidation: mechanisms and analysis.* Chem Rev, 2011. **111**(10): p. 5944-72.

21. Ayala, A., M.F. Munoz, and S. Arguelles, *Lipid peroxidation: production, metabolism, and signaling mechanisms of malondialdehyde and 4-hydroxy-2-nonenal.* Oxid Med Cell Longev, 2014. **2014**: p. 360438.

22. Friedmann Angeli, J.P., et al., *Inactivation of the ferroptosis regulator Gpx4 triggers acute renal failure in mice.* Nat Cell Biol, 2014. **16**(12): p. 1180-91.

23. Doll, S., et al., *ACSL4 dictates ferroptosis sensitivity by shaping cellular lipid composition.* Nat Chem Biol, 2017. **13**(1): p. 91-98.

24. Liang, D., et al., *Ferroptosis surveillance independent of GPX4 and differentially regulated by sex hormones.* Cell, 2023. **186**(13): p. 2748-2764 e22.

25. Gibson, D.D., K.R. Hornbrook, and P.B. McCay, *Glutathione-dependent inhibition of lipid peroxidation by a soluble, heat-labile factor in animal tissues.* Biochim Biophys Acta, 1980. **620**(3): p. 572-82.

26. Maiorino, M., M. Conrad, and F. Ursini, *GPx4, Lipid Peroxidation, and Cell Death: Discoveries, Rediscoveries, and Open Issues.* Antioxid Redox Signal, 2018. **29**(1): p. 61-74.

27. Thomas, J.P., et al., *Enzymatic reduction of phospholipid and cholesterol hydroperoxides in artificial bilayers and lipoproteins.* Biochim Biophys Acta, 1990. **1045**(3): p. 252-60.

28. Pfeifer, H., et al., *Identification of a specific sperm nuclei selenoenzyme necessary for protamine thiol cross-linking during sperm maturation.* FASEB J, 2001. **15**(7): p. 1236-8.

29. Brigelius-Flohe, R. and M. Maiorino, *Glutathione peroxidases.* Biochim Biophys Acta, 2013. **1830**(5): p. 3289-303.

30. Liang, H., et al., *Short form glutathione peroxidase 4 is the essential isoform required for survival and somatic mitochondrial functions.* J Biol Chem, 2009. **284**(45): p. 30836-44.

31. Ingold, I., et al., *Selenium Utilization by GPX4 Is Required to Prevent Hydroperoxide-Induced Ferroptosis.* Cell, 2018. **172**(3): p. 409-422 e21.

32. Bersuker, K., et al., *The CoQ oxidoreductase FSP1 acts parallel to GPX4 to inhibit ferroptosis.* Nature, 2019. **575**(7784): p. 688-692.

33. Nakamura, T., et al., *Phase separation of FSP1 promotes ferroptosis.* Nature, 2023. **619**(7969): p. 371-377.

34. Doll, S., et al., *FSP1 is a glutathione-independent ferroptosis suppressor.* Nature, 2019. **575**(7784): p. 693-698.

35. Mishima, E., et al., *A non-canonical vitamin K cycle is a potent ferroptosis suppressor.* Nature, 2022. **608**(7924): p. 778-783.

36. Ingold, K.U. and D.A. Pratt, *Advances in radical-trapping antioxidant chemistry in the 21st century: a kinetics and mechanisms perspective.* Chem Rev, 2014. **114**(18): p. 9022-46.

37. Bannai, S., H. Tsukeda, and H. Okumura, *Effect of antioxidants on cultured human diploid fibroblasts exposed to cystine-free medium.* Biochem Biophys Res Commun, 1977. **74**(4): p. 1582-8.

38. Lu, S.C., *Glutathione synthesis.* Biochim Biophys Acta, 2013. **1830**(5): p. 3143-53.

39. Bannai, S. and E. Kitamura, *Transport interaction of L-cystine and L-glutamate in human diploid fibroblasts in culture.* J Biol Chem, 1980. **255**(6): p. 2372-6.

40. Sato, M., et al., *The ferroptosis inducer erastin irreversibly inhibits system x(c)- and synergizes with cisplatin to increase cisplatin's cytotoxicity in cancer cells.* Sci Rep, 2018. **8**(1): p. 968.

41. Murphy, T.H., et al., *Glutamate toxicity in a neuronal cell line involves inhibition of cystine transport leading to oxidative stress.* Neuron, 1989. **2**(6): p. 1547-58.

42. Kalogeris, T., et al., *Ischemia/Reperfusion.* Compr Physiol, 2016. **7**(1): p. 113-170.

43. Pan, J., et al., *Reperfusion injury following cerebral ischemia: pathophysiology, MR imaging, and potential therapies.* Neuroradiology, 2007. **49**(2): p. 93-102.

44. Chouchani, E.T., et al., *Ischaemic accumulation of succinate controls reperfusion injury through mitochondrial ROS.* Nature, 2014. **515**(7527): p. 431-435.

45. Shaik, N.F., R.F. Regan, and U.P. Naik, *Platelets as drivers of ischemia/reperfusion injury after stroke.* Blood Adv, 2021. **5**(5): p. 1576-1584.

46. Zhao, J., et al., *Liproxstatin-1 Alleviates Lung Transplantation-induced Cold Ischemia-Reperfusion Injury by Inhibiting Ferroptosis.* Transplantation, 2023. **107**(10): p. 2190-2202.

47. Tuo, Q.Z., et al., *Tau-mediated iron export prevents ferroptotic damage after ischemic stroke.* Mol Psychiatry, 2017. **22**(11): p. 1520-1530.

48. Thompson, A.J., et al., *Multiple sclerosis.* Lancet, 2018. **391**(10130): p. 1622-1636.

49. Hu, C.L., et al., *Reduced expression of the ferroptosis inhibitor glutathione peroxidase-4 in multiple sclerosis and experimental autoimmune encephalomyelitis.* J Neurochem, 2019. **148**(3): p. 426-439.

50. Van San, E., et al., *Ferroptosis contributes to multiple sclerosis and its pharmacological targeting suppresses experimental disease progression.* Cell Death Differ, 2023. **30**(9): p. 2092-2103.

51. Jhelum, P., et al., *Ferroptosis induces detrimental effects in chronic EAE and its implications for progressive MS.* Acta Neuropathol Commun, 2023. **11**(1): p. 121.

52. Lv, Z., et al., *Single cell RNA-seq analysis identifies ferroptotic chondrocyte cluster and reveals TRPV1 as an anti-ferroptotic target in osteoarthritis.* EBioMedicine, 2022. **84**: p. 104258.

53. Miao, Y., et al., *Contribution of ferroptosis and GPX4's dual functions to osteoarthritis progression.* EBioMedicine, 2022. **76**: p. 103847.

54. Han, J., et al., *Moderate mechanical stress suppresses chondrocyte ferroptosis in osteoarthritis by regulating NF-kappaB p65/GPX4 signaling pathway.* Sci Rep, 2024. **14**(1): p. 5078.

55. Tanski, W., et al., *Iron metabolism in patients with rheumatoid arthritis.* Eur Rev Med Pharmacol Sci, 2021. **25**(12): p. 4325-4335.

56. Zhao, T., et al., *Ferroptosis in Rheumatoid Arthritis: A Potential Therapeutic Strategy.* Front Immunol, 2022. **13**: p. 779585.

57. Ayton, S., et al., *Ferritin levels in the cerebrospinal fluid predict Alzheimer's disease outcomes and are regulated by APOE.* Nat Commun, 2015. **6**: p. 6760.

58. Ayton, S., et al., *Regional brain iron associated with deterioration in Alzheimer's disease: A large cohort study and theoretical significance.* Alzheimers Dement, 2021. **17**(7): p. 1244-1256.

59. Mandal, P.K., et al., *Hippocampal glutathione depletion with enhanced iron level in patients with mild cognitive impairment and Alzheimer's disease compared with healthy elderly participants.* Brain Commun, 2022. **4**(5): p. fcac215.

60. Bradley, M.A., et al., *Elevated 4-hydroxyhexenal in Alzheimer's disease (AD) progression.* Neurobiol Aging, 2012. **33**(6): p. 1034-44.

61. Hare, D., et al., *A delicate balance: Iron metabolism and diseases of the brain.* Front Aging Neurosci, 2013. **5**: p. 34.

62. Riederer, P., et al., *Transition metals, ferritin, glutathione, and ascorbic acid in parkinsonian brains.* J Neurochem, 1989. **52**(2): p. 515-20.

63. Lorenzen, I., et al., *Redox Regulation of Inflammatory Processes Is Enzymatically Controlled.* Oxid Med Cell Longev, 2017. **2017**: p. 8459402.

64. Hanschmann, E.M., et al., *Thioredoxins, glutaredoxins, and peroxiredoxins--molecular mechanisms and health significance: from cofactors to antioxidants to redox signaling.* Antioxid Redox Signal, 2013. **19**(13): p. 1539-605.

65. Martin, J.L., *Thioredoxin--a fold for all reasons.* Structure, 1995. **3**(3): p. 245-50.

66. Hudemann, C., et al., *Identification, expression pattern, and characterization of mouse glutaredoxin 2 isoforms.* Antioxid Redox Signal, 2009. **11**(1): p. 1-14.

67. Lonn, M.E., et al., *Expression pattern of human glutaredoxin 2 isoforms: identification and characterization of two testis/cancer cell-specific isoforms.* Antioxid Redox Signal, 2008. **10**(3): p. 547-57.

68. Lillig, C.H. and C. Berndt, *Glutaredoxins in thiol/disulfide exchange.* Antioxid Redox Signal, 2013. **18**(13): p. 1654-65.

69. Rodriguez-Manzaneque, M.T., et al., *Grx5 is a mitochondrial glutaredoxin required for the activity of iron/sulfur enzymes.* Mol Biol Cell, 2002. **13**(4): p. 1109-21.

70. Haunhorst, P., et al., *Crucial function of vertebrate glutaredoxin 3 (PICOT) in iron homeostasis and hemoglobin maturation.* Mol Biol Cell, 2013. **24**(12): p. 1895-903.

71. Brautigam, L., et al., *Glutaredoxin regulates vascular development by reversible glutathionylation of sirtuin 1.* Proc Natl Acad Sci U S A, 2013. **110**(50): p. 20057-62.

72. Lillig, C.H., C. Berndt, and A. Holmgren, *Glutaredoxin systems.* Biochim Biophys Acta, 2008. **1780**(11): p. 1304-17.

73. Matsui, R., et al., *Redox Regulation via Glutaredoxin-1 and Protein S-Glutathionylation.* Antioxid Redox Signal, 2020. **32**(10): p. 677-700.

74. Lillig, C.H., et al., *Characterization of human glutaredoxin 2 as iron-sulfur protein: a possible role as redox sensor.* Proc Natl Acad Sci U S A, 2005. **102**(23): p. 8168-73.

75. Berndt, C., et al., *How does iron-sulfur cluster coordination regulate the activity of human glutaredoxin 2?* Antioxid Redox Signal, 2007. **9**(1): p. 151-7.

76. Lepka, K., et al., *Iron-sulfur glutaredoxin 2 protects oligodendrocytes against damage induced by nitric oxide release from activated microglia.* Glia, 2017. **65**(9): p. 1521-1534.

77. Waxman, S.G., *Nitric oxide and the axonal death cascade.* Ann Neurol, 2003. **53**(2): p. 150-3.

78. Scalcon, V., et al., *Mitochondrial depletion of glutaredoxin 2 induces metabolic dysfunction-associated fatty liver disease in mice.* Redox Biol, 2022. **51**: p. 102277.

79. Enoksson, M., et al., *Overexpression of glutaredoxin 2 attenuates apoptosis by preventing cytochrome c release.* Biochem Biophys Res Commun, 2005. **327**(3): p. 774-9.

80. Dolma, S., et al., *Identification of genotype-selective antitumor agents using synthetic lethal chemical screening in engineered human tumor cells.* Cancer Cell, 2003. **3**(3): p. 285-96.

81. Dixon, S.J., et al., *Pharmacological inhibition of cystine-glutamate exchange induces endoplasmic reticulum stress and ferroptosis.* Elife, 2014. **3**: p. e02523.

82. Chen, Y., et al., *Oxidative stress induces mitochondrial iron overload and ferroptotic cell death.* Sci Rep, 2023. **13**(1): p. 15515.

83. Wirth, E.K., et al., *Neuronal selenoprotein expression is required for interneuron development and prevents seizures and neurodegeneration.* FASEB J, 2010. **24**(3): p. 844-52.

84. Forman, H.J., F. Ursini, and M. Maiorino, *An overview of mechanisms of redox signaling.* J Mol Cell Cardiol, 2014. **73**: p. 2-9.

85. Giustarini, D., et al., *S-glutathionylation: from redox regulation of protein functions to human diseases.* J Cell Mol Med, 2004. **8**(2): p. 201-12.

86. Dalle-Donne, I., et al., *S-glutathionylation in protein redox regulation.* Free Radic Biol Med, 2007. **43**(6): p. 883-98.

87. Klatt, P. and S. Lamas, *Regulation of protein function by S-glutathiolation in response to oxidative and nitrosative stress.* Eur J Biochem, 2000. **267**(16): p. 4928-44.

88. Casagrande, S., et al., *Glutathionylation of human thioredoxin: a possible crosstalk between the glutathione and thioredoxin systems.* Proc Natl Acad Sci U S A, 2002. **99**(15): p. 9745-9.

89. Arner, E.S. and A. Holmgren, *Physiological functions of thioredoxin and thioredoxin reductase.* Eur J Biochem, 2000. **267**(20): p. 6102-9.

90. Anashkina, A.A., et al., *Glutathione Non-Covalent Binding Sites on Hemoglobin and Major Glutathionylation Target betaCys93 Are Conservative among Both*

Hypoxia-Sensitive and Hypoxia-Tolerant Mammal Species. Int J Mol Sci, 2023. **25**(1).

91. Craescu, C.T., et al., *Covalent binding of glutathione to hemoglobin. II. Functional consequences and structural changes reflected in NMR spectra.* J Biol Chem, 1986. **261**(31): p. 14710-6.

92. Niwa, T., et al., *Increased glutathionyl hemoglobin in diabetes mellitus and hyperlipidemia demonstrated by liquid chromatography/electrospray ionization-mass spectrometry.* Clin Chem, 2000. **46**(1): p. 82-8.

93. Al-Abed, Y., et al., *Characterization of a novel hemoglobin-glutathione adduct that is elevated in diabetic patients.* Mol Med, 2001. **7**(9): p. 619-23.

94. Liu, T., et al., *The Deubiquitylase OTUB1 Mediates Ferroptosis via Stabilization of SLC7A11.* Cancer Res, 2019. **79**(8): p. 1913-1924.

95. Aboushousha, R., et al., *Glutathionylation chemistry promotes interleukin-1 beta-mediated glycolytic reprogramming and pro-inflammatory signaling in lung epithelial cells.* FASEB J, 2021. **35**(5): p. e21525.

96. Aboushousha, R., et al., *Glutaredoxin attenuates glutathione levels via deglutathionylation of Otub1 and subsequent destabilization of system x(C)().* Sci Adv, 2023. **9**(37): p. eadi5192.

97. Cozza, G., et al., *Glutathione peroxidase 4-catalyzed reduction of lipid hydroperoxides in membranes: The polar head of membrane phospholipids binds the enzyme and addresses the fatty acid hydroperoxide group toward the redox center.* Free Radic Biol Med, 2017. **112**: p. 1-11

.

98. Oblong, J.E., et al., *Site-directed mutagenesis of active site cysteines in human thioredoxin produces competitive inhibitors of human thioredoxin reductase and elimination of mitogenic properties of thioredoxin.* J Biol Chem, 1994. **269**(16): p. 11714-20.

99. Pavlin, M., et al., *Unraveling the Impact of Cysteine-to-Serine Mutations on the Structural and Functional Properties of Cu(I)-Binding Proteins.* Int J Mol Sci, 2019. **20**(14).

100. Otto, N.M., et al., *A Glutamate-Substituted Mutant Mimics the Phosphorylated and Active Form of Guanylyl Cyclase-A.* Mol Pharmacol, 2017. **92**(1): p. 67-74.

101. Zisch, A.H., et al., *Replacing two conserved tyrosines of the EphB2 receptor with glutamic acid prevents binding of SH2 domains without abrogating kinase activity and biological responses.* Oncogene, 2000. **19**(2): p. 177-87.

102. Roveri, A., et al., *Cardiolipin drives the catalytic activity of GPX4 on membranes: Insights from the R152H mutant.* Redox Biol, 2023. **64**: p. 102806.

103. Sedaghatian, M.R., *Congenital lethal metaphyseal chondrodysplasia: a newly recognized complex autosomal recessive disorder.* Am J Med Genet, 1980. **6**(4): p. 269-74.

104. Elcioglu, N. and C.M. Hall, *Spondylometaphyseal dysplasia-Sedaghatian type.* Am J Med Genet, 1998. **76**(5): p. 410-4.

105. Liu, H., et al., *Characterization of a patient-derived variant of GPX4 for precision therapy.* Nat Chem Biol, 2022. **18**(1): p. 91-100.

106. Sun, X., et al., *TRIM21 ubiquitylates GPX4 and promotes ferroptosis to aggravate ischemia/reperfusion-induced acute kidney injury.* Life Sci, 2023. **321**: p. 121608.

107. Wu, K., et al., *Creatine kinase B suppresses ferroptosis by phosphorylating GPX4 through a moonlighting function.* Nat Cell Biol, 2023. **25**(5): p. 714-725.

108. Li, J., S. Liu, and S. Li, *Mechanisms underlying linear ubiquitination and implications in tumorigenesis and drug discovery.* Cell Commun Signal, 2023. **21**(1): p. 340.

109. Kirisako, T., et al., *A ubiquitin ligase complex assembles linear polyubiquitin chains.* EMBO J, 2006. **25**(20): p. 4877-87.

110. Dong, K., et al., *HOIP modulates the stability of GPx4 by linear ubiquitination.* Proc Natl Acad Sci U S A, 2022. **119**(44): p. e2214227119.

111. Wang, Z., et al., *AMPKalpha1-mediated ZDHHC8 phosphorylation promotes the palmitoylation of SLC7A11 to facilitate ferroptosis resistance in glioblastoma.* Cancer Lett, 2024. **584**: p. 216619.

112. Ma, Y., et al., *CD36 promotes tubular ferroptosis by regulating the ubiquitination of FSP1 in acute kidney injury.* Genes Dis, 2024. **11**(1): p. 449-463.

113. Eisenhaber, F., et al., *Prediction of lipid posttranslational modifications and localization signals from protein sequences: big-Pi, NMT and PTS1.* Nucleic Acids Res, 2003. **31**(13): p. 3631-4.

114. Zee, R.S., et al., *Redox regulation of sirtuin-1 by S-glutathiolation.* Antioxid Redox Signal, 2010. **13**(7): p. 1023-32.

115. Beer, S.M., et al., *Glutaredoxin 2 catalyzes the reversible oxidation and glutathionylation of mitochondrial membrane thiol proteins: implications for mitochondrial redox regulation and antioxidant DEFENSE.* J Biol Chem, 2004. **279**(46): p. 47939-51.

116. Trnka, D., *Functional characterization of human class I and class II mitochondrial glutaredoxins*, in *Faculty of Mathematics and Natural Sciences*. 2018, University of Greifswald.

117. Daniel, T., et al., *Role of GSH and Iron-Sulfur Glutaredoxins in Iron Metabolism-Review.* Molecules, 2020. **25**(17).

118. Godoy, J.R., et al., *Redox atlas of the mouse. Immunohistochemical detection of glutaredoxin-, peroxiredoxin-, and thioredoxin-family proteins in various tissues of the laboratory mouse.* Biochim Biophys Acta, 2011. **1810**(1): p. 2-92.

119. Vig, P.J., et al., *Decreased parvalbumin immunoreactivity in surviving Purkinje cells of patients with spinocerebellar ataxia-1.* Neurology, 1996. **47**(1): p. 249-53.

120. Godoy, L.D., et al., *Parvalbumin Role in Epilepsy and Psychiatric Comorbidities: From Mechanism to Intervention.* Front Integr Neurosci, 2022. **16**: p. 765324.

121. Devinsky, O., et al., *Epilepsy.* Nat Rev Dis Primers, 2018. **4**: p. 18024.

122. Massobrio, P., et al., *Selective modulation of chemical and electrical synapses of Helix neuronal networks during in vitro development.* BMC Neurosci, 2013. **14**: p. 22.

123. Yamaguchi, S. and M.A. Rogawski, *Effects of anticonvulsant drugs on 4-aminopyridine-induced seizures in mice.* Epilepsy Res, 1992. **11**(1): p. 9-16.

124. Yu, Y., et al., *Hepatic transferrin plays a role in systemic iron homeostasis and liver ferroptosis.* Blood, 2020. **136**(6): p. 726-739.

125. Peleman, C., et al., *Ferroptosis is a targetable detrimental factor in metabolic dysfunction-associated steatotic liver disease.* Cell Death Differ, 2024. **31**(9): p. 1113-1126.

126. Schneider, M., et al., *Mitochondrial glutathione peroxidase 4 disruption causes male infertility.* FASEB J, 2009. **23**(9): p. 3233-42.

127. Azuma, K., et al., *Mitochondrial glutathione peroxidase 4 is indispensable for photoreceptor development and survival in mice.* J Biol Chem, 2022. **298**(4): p. 101824.

128. Gellert, M., et al., *Redox regulation of cytoskeletal dynamics during differentiation and de-differentiation.* Biochim Biophys Acta, 2015. **1850**(8): p. 1575-87.

129. Kanaan, G.N., et al., *Glutaredoxin-2 controls cardiac mitochondrial dynamics and energetics in mice, and protects against human cardiac pathologies.* Redox Biol, 2018. **14**: p. 509-521.

130. Persoon-Rothert, M., et al., *Prevention of cumene hydroperoxide induced oxidative stress in cultured neonatal rat myocytes by scavengers and enzyme inhibitors.* J Mol Cell Cardiol, 1990. **22**(10): p. 1147-55.

131. Mashamaite, L.N., J.M. Rohwer, and C.S. Pillay, *The glutaredoxin mono- and di-thiol mechanisms for deglutathionylation are functionally equivalent: implications for redox systems biology.* Biosci Rep, 2015. **35**(1).

132. Mieyal, J.J., et al., *Molecular mechanisms and clinical implications of reversible protein S-glutathionylation.* Antioxid Redox Signal, 2008. **10**(11): p. 1941-88.

133. Hanschmann, E.M., et al., *Cytosolic glutaredoxin 1 is upregulated in AMD and controls retinal pigment epithelial cells proliferation via beta-catenin.* Biochem Biophys Res Commun, 2022. **618**: p. 24-29.

134. Liu, X., et al., *Glutaredoxin 1 (Grx1) Protects Human Retinal Pigment Epithelial Cells From Oxidative Damage by Preventing AKT Glutathionylation.* Invest Ophthalmol Vis Sci, 2015. **56**(5): p. 2821-32.

135. Zhang, X., et al., *Akt, FoxO and regulation of apoptosis.* Biochim Biophys Acta, 2011. **1813**(11): p. 1978-86.

136. Berndt, C., J. Schwenn, and C.H. Lillig, *The specificity of thioredoxins and glutaredoxins is determined by electrostatic and geometric complementarity.* Chem. Sci., 2015. **6**: p. 7049-7058.

137. Conrad, M., S.M. Lorenz, and B. Proneth, *Targeting Ferroptosis: New Hope for As-Yet-Incurable Diseases.* Trends Mol Med, 2021. **27**(2): p. 113-122.

138. Cheng, J., Y. Xiao, and P. Jiang, *Fumarate integrates metabolism and immunity in diseases.* Trends Endocrinol Metab, 2025.

139. Sabet, H., et al., *Safety and effectiveness of diroximel fumarate in relapsing forms of multiple sclerosis: a systematic review and meta-analysis.* Neurol Sci, 2025.

140. Gudesblatt, M., et al., *De-escalation of Disease-Modifying Therapy for People with Multiple Sclerosis Due to Safety Considerations: Characterizing 1-Year Outcomes in 25 People Who Switched from Ocrelizumab to Diroximel Fumarate.* Adv Ther, 2024. **41**(8): p. 3059-3075.

141. Yousuf, M.S., et al., *Diroximel fumarate acts through Nrf2 to attenuate methylglyoxal-induced nociception in mice and decrease ISR activation in DRG neurons.* Diabetes, 2025.

142. Yamamoto, M., T.W. Kensler, and H. Motohashi, *The KEAP1-NRF2 System: a Thiol-Based Sensor-Effector Apparatus for Maintaining Redox Homeostasis.* Physiol Rev, 2018. **98**(3): p. 1169-1203.

143. Suzuki, T., et al., *Systemic Activation of NRF2 Alleviates Lethal Autoimmune Inflammation in Scurfy Mice.* Mol Cell Biol, 2017. **37**(15).

144. Habib, E., et al., *Expression of xCT and activity of system xc(-) are regulated by NRF2 in human breast cancer cells in response to oxidative stress.* Redox Biol, 2015. **5**: p. 33-42.

145. Marcellin, L., et al., *Alteration of Nrf2 and Glutamate Cysteine Ligase expression contribute to lesions growth and fibrogenesis in ectopic endometriosis.* Free Radic Biol Med, 2017. **110**: p. 1-10.

146. Kerins, M.J. and A. Ooi, *The Roles of NRF2 in Modulating Cellular Iron Homeostasis.* Antioxid Redox Signal, 2018. **29**(17): p. 1756-1773.

147. Dodson, M., R. Castro-Portuguez, and D.D. Zhang, *NRF2 plays a critical role in mitigating lipid peroxidation and ferroptosis.* Redox Biol, 2019. **23**: p. 101107.

148. Chen, C., et al., *Induction of ferroptosis by HO-1 contributes to retinal degeneration in mice with defective clearance of all-trans-retinal.* Free Radic Biol Med, 2023. **194**: p. 245-254.

149. Wu, J., et al., *TNF antagonist sensitizes synovial fibroblasts to ferroptotic cell death in collagen-induced arthritis mouse models.* Nat Commun, 2022. **13**(1): p. 676.

150. Inouye, S., et al., *NRF2 and HSF1 coordinately regulate heme oxygenase-1 expression.* Biochem Biophys Res Commun, 2018. **506**(1): p. 7-11.

151. Loboda, A., et al., *Role of Nrf2/HO-1 system in development, oxidative stress response and diseases: an evolutionarily conserved mechanism.* Cell Mol Life Sci, 2016. **73**(17): p. 3221-47.

152. Kasai, S., et al., *Emerging Regulatory Role of Nrf2 in Iron, Heme, and Hemoglobin Metabolism in Physiology and Disease.* Front Vet Sci, 2018. **5**: p. 242.

153. Zhang, L., et al., *Nrf2 Is a Potential Modulator for Orchestrating Iron Homeostasis and Redox Balance in Cancer Cells.* Front Cell Dev Biol, 2021. **9**: p. 728172.

154. Zhao, T., et al., *Regulating Nrf2-GPx4 axis by bicyclol can prevent ferroptosis in carbon tetrachloride-induced acute liver injury in mice.* Cell Death Discov, 2022. **8**(1): p. 380.

155. Ufer, C., A. Borchert, and H. Kuhn, *Functional characterization of cis- and trans-regulatory elements involved in expression of phospholipid hydroperoxide glutathione peroxidase.* Nucleic Acids Res, 2003. **31**(15): p. 4293-303.

156. Ufer, C., et al., *Translational regulation of glutathione peroxidase 4 expression through guanine-rich sequence-binding factor 1 is essential for embryonic brain development.* Genes Dev, 2008. **22**(13): p. 1838-50.

157. Nguyen, L., et al., *JNK Signalling Regulates Self-Renewal of Proliferative Urine-Derived Renal Progenitor Cells via Inhibition of Ferroptosis.* Cells, 2023. **12**(17).

158. Lim, J.K.M., et al., *Oncogenic RAS signaling suppresses ferroptosis via transcriptional upregulation of GCH1.* bioRxiv, 2024: p. 2024.01.27.577524.

159. Pensotti, R., et al., *Redox homeostasis in ferroptosis and aging: a causal role for fard-1 and dhs-25 in Caenorhabditis elegans*. bioRxiv, 2025: p. 2025.01.07.631721.

160. Berndt, C., et al., *FeS-cluster coordination of vertebrate thioredoxin regulates suppression of hypoxia-induced factor 2α through iron regulatory protein 1*. bioRxiv, 2024: p. 2020.08.04.235721.

13 Publications during the doctorate

13.1 JNK Signaling Regulates Self-Renewal of Proliferative Urine-Derived Renal Progenitor Cells via Inhibition of Ferroptosis

All authors:

Lisa Nguyen, **Leonie Thewes**, Michelle Westerhoff, Wasco Wruck, Andreas S. Reichert, Carsten Berndt, and James Adjaye.

Copyright notice:

Impact factor: 5.1 (2023)

Summary and contribution:

The rising mortality rate due to renal diseases necessitates the development of novel therapeutic modalities in addition to conventional dialysis and organ transplantation. A promising approach involves the cell replacement with urine-derived renal progenitor cells (UdRPCs). These progenitor cells can be extracted from urine at a low cost and without ethical concerns. A significant aspect of the research involves the investigation of the c-Jun N-terminal kinase (JNK) signaling pathway, as it plays a pivotal role in regulating proliferation and cell survival, and is associated with both acute and chronic kidney disease. This study demonstrates a correlation between JNK signaling and the maintenance of proliferation and self-renewal in UdRPCs. Furthermore, we observed an influence of JNK on the protection against ferroptosis. Inhibition of the JNK pathway has been observed to result in increased lipid peroxidation and decreased cell survival in UdRPCs. However, this effect can be mitigated by the ferroptosis inhibitor Lip-1. The influence of the JNK signaling pathway on UdRPCs extends beyond proliferation, encompassing their metabolic state and mitochondrial function. Given the established role of ferroptosis in the development of kidney diseases, the targeted modulation of the JNK signaling pathway can serve as a model for ferroptosis-induced kidney conditions, while promoting JNK signaling in UdRPCs may offer a novel strategy for kidney regeneration experiments. My contributions to the project included the measurement of accumulated lipid peroxides and cell death by flow cytometric analysis. I also performed cell viability assays and measured intracellular GSH levels in the UdRPCs. Finally, I assisted in the preparation of the manuscript.

13.2 Oncogenic RAS signaling suppresses ferroptosis via transcriptional upregulation of GCH1

All authors:

Jonathan K. M. Lim, Frauke Stölting, Tal Levy, **Leonie Thewes**, Daniel Picard, Sofya Tishina, Hai-Feng Zhang, Oksana Lewandowska, Tobias Reiff, Marc Remke, Johannes Brägelmann, Filippo Beleggia, Carsten Berndt, Silvia von Karstedt, Guido Reifenberger, Barak Rotblat, Gabriel Leprivier

Copyright notice:

Summary and contribution:

In human cancer, particularly in cases of pancreatic, colorectal, and lung adenocarcinomas, the RAS proto-oncogenes are frequently mutated, thereby constituting an important component of cancer research. The occurrence of RAS mutations leads to the oncogenic transformation of cells that include not only tumor initiation but also enhanced stress response and cell death evasion. Specifically, oncogenic RAS has been shown to enhance resistance to apoptosis induction, a process that may contribute to therapy-resistance. This observation has fueled research into the potential benefits of inducing alternative cell death modalities in cancer cells. In this study, our focus was on ferroptotic cell death, and we demonstrated that oncogenic RAS signaling confers a protective effect against ferroptosis induction. The evidence suggests that oncogenic RAS signaling leads to the upregulation of the ferroptosis suppressor GTP cyclohydrolase 1 (GCH1) via transcriptional induction by the transcription factor ETS1 downstream of the RAS-MAPK signaling cascade. Conversely, the suppression of GCH1 or GCH1-mediated tetrahydrobiopterin (BH4) synthesis renders oncogenic RAS-expressing cells sensitive to ferroptosis, thereby making targeted regulation of GCH1 clinically relevant for the treatment of RAS-driven cancers. My contributions to the research project included the measurement of accumulated lipid peroxides by flow cytometric analysis after ferroptosis induction via Erastin or FINO2 and inhibition using dihydrobiopterin (BH2), BH4, and Fer-1.

13.3 Ferroptosis in Health and Disease

All authors:

Carsten Berndt, Hamed Alborzinia, Vera Skafar Amen, Scott Ayton, Uladzimir Barayeu, Alexander Bartelt, Hülya Bayir, Christina M. Bebber, Kivanc Birsoy, Jan P. Böttcher, Simone Brabletz, Thomas Brabletz, Ashley R. Brown, Bernhard Brüne, Giorgia Bulli, Alix Bruneau, Quan Chen, Gina M. DeNicola, Tobias P. Dick, Ayelén Distéfano, Scott J. Dixon, Jan B. Engler, Julia Esser-von Bieren, Maria Fedorova, José Pedro Friedmann Angeli, Manuel A. Friese, Dominic C. Fuhrmann, Ana J. García-Sáez, Karolina Garbowicz, Magdalena Götz, Wei Gu, Linda Hammerich, Behrouz Hassannia, Xuejun Jiang, Aicha Jeridi, Yun Pyo Kang, Valerian E. Kagan, David B. Konrad, Stefan Kotschi, Peng Lei, Marlène Le Tertre, Sima Lev, Deguang Liang, Andreas Linkermann, Carolin Lohr, Svenja Lorenz, Tom Luedde, Axel Methner, Bernhard Michalke, Anna V. Milton, Junxia Min, Eikan Mishima, Sebastian Müller, Hozumi Motohashi, Martina U. Muckenthaler, Shohei Murakami, James A. Olzmann, Gabriela Pagnussat, Zijan Pan, Thales Papagiannakopoulos, Lohans Pedrera Puentes, Derek A. Pratt, Bettina Proneth, Lukas Ramsauer, Raphael Rodriguez, Yoshiro Saito, Felix Schmidt, Carina Schmitt, Almut Schulze, Annemarie Schwab, Anna Schwantes, Mariluz Soula, Benedikt Spitzlberger, Brent R. Stockwell, **Leonie Thewes**, Oliver Thorn-Seshold, Shinya Toyokuni, Wulf Tonnus, Andreas Trumpp, Peter Vandenabeele, Tom Vanden Berghe, Vivek Venkataramani, Felix C.E. Vogel, Silvia von Karstedt, Fudi Wang, Frank Westermann, Chantal Wientjens, Christoph Wilhelm, Michele Wölk, Katherine Wu, Xin Yang, Fan Yu, Yilong Zou, Marcus Conrad.

Copyright notice:

Impact factor: 10.7 (2023)

Summary and contribution:

Following its initial characterization as a form of iron-dependent cell death in 2012, the field of ferroptosis research has witnessed a marked surge in scholarly interest. The research community's current efforts are focused on investigating the regulatory mechanisms and sensitivity of ferroptosis, in addition to its pharmacological potential. In this comprehensive review, we have collated the latest insights into ferroptosis and key areas of research in conjunction with over 90 experts in the field. My contribution to this

review was the preparation of chapter 3.3, which deals with the posttranslational modifications of ferroptotic enzymes. This chapter elucidates the influence of these various modifications on the regulation of this cell death mechanism, both pro-ferroptotic and anti-ferroptotic. In addition to my contributions to the content, I assisted with the formatting of the manuscript and participated in the editorial work.

13.4 Redox homeostasis in ferroptosis and aging: a causal role for *fard-1* and *dhs-25* in *Caenorhabditis elegans*

All authors:

Roberta Pensotti, Barbara Sciandrone, Federica Bovio, Laura Schröter, Silvia Maglioni, **Leonie Thewes**, Matilde Emma Forcella, Paola Alessandra Fusi, Andrea Rossi, Carsten Berndt, Natascia Ventura, Maria Elena Regonesi

Copyright notice:

This work is uploaded as a preprint on *BioRxiv* **2025**, 2025.01.07.631721 [159] and was recently submitted at *Cell Death and Differentiation*.

Summary and contribution:

Aging is a natural process characterized by a progressive physiological decline and an imbalance in redox regulation. Previous studies have identified a connection between ferroptosis and aging, with silencing frataxin, a mitochondrial protein involved in FeS cluster biogenesis, having been shown to extend the lifespan of *Caenorhabditis elegans* by inhibiting ferroptosis. While the role of ferroptosis in pathological conditions such as cancer and neurodegeneration has been demonstrated, its physiological roles and regulators remain to be fully elucidated. This study demonstrates the disruption of redox homeostasis in older *Caenorhabditis elegans* and a downregulation of genes involved in redox metabolism. Futhermore, the analysis of mutant strains of the fatty acyl-CoA reductase, *fard-1*, and the dehydrogenase, *dhs-25*, revealed an augmented sensitivity to a ferroptosis inducer, an increased lipid peroxidation, a predicted decline in total glutathione, and a diminished lifespan. Additionally, the expression of a homolog of *dhs-25*, hydroxysteroid 17-beta Dehydrogenase 8, was found to be downregulated in cells exhibiting heightened sensitivity to ferroptosis. In summary, we have identified genes that provide a promising link between ferroptosis and aging, as well as potential new interventions to improve healthy aging. My contribution to this research was to translate the results found in *Caenorhabditis elegans* into mammalian cells. This process entailed the execution of a series of assays, encompassing cell survival assays, gel electrophoresis, western blot analysis, and qPCR.

14 Further publications

14.1 FeS-cluster coordination of vertebrate thioredoxin regulates suppression of hypoxia-induced factor 2α through iron regulatory protein 1

All authors:

Carsten Berndt, Eva-Maria Hanschmann, Laura Magdalena Jordt, Manuela Gellert, **Leonie Thewes**, Clara Ortegón Salas, Gereon Poschmann, Christina Sophia Müller, Yana Bodnar, Susanne Schipper, Oliver Handorf, Ricardo Nowack, Jean-Marc Moulis, Carola Schulzke, Volker Schünemann, Christopher Horst Lillig

Copyright notice:

Summary and contribution:

Redox-controlled cellular functions depend on the presence of iron and other cofactors. Iron can be integrated into proteins different cofactors including heme and iron-sulfur clusters. These iron-containing proteins play critical roles in processes such as oxygen transport and electron transfer reactions. An imbalance in iron levels within the body has been linked to various pathological conditions. An excess of iron can result in cellular toxicity, while insufficient iron levels are associated with anemia, underscoring the significance of maintaining optimal iron homeostasis. Vertebrates regulate the internal iron balance via iron regulatory proteins (IRP). IRP1 is active under iron-deficient conditions, in which the iron-sulfur cluster of IRP1 is dissembled. The active form of IRP1 is capable of binding iron-responsive element (IRE) structures present within the mRNA of proteins such as hypoxia-induced factor 2α (HIF2α), which has been defined as a transcription factor for erythropoiesis, among other functions.

In this study, we sought to elucidate the role of thioredoxin 1 (Trx1) in the regulation of iron balance via IRP mechanisms. Trx1 contains an iron-sulfur (FeS) cluster, the disruption of which enables Trx1 to function as an oxidoreductase. The reduction of cysteinyl residues in apo-IRP1 by Trx1 is a prerequisite for their binding to IREs. My contribution to this work included the measurement of NADPH consumption of Trx1 in the presence of holo-

and apo-IRP1 under anaerobic conditions, as well as the measurement of IRP1/HIF2α-IRE binding using electrophoretic mobility shift assays.

15 Appendix

15.1 List of abbreviations

Table 14: List of abbreviations

Abbreviation	Definition
4-AP	4-aminopyridine
4-HNE	4-hydroxynonenal
ACD	Accidental cell death
ACSL4	Acyl-CoA synthetase long-chain family member 4
AD	Alzheimer's disease
AMD	Age-related macular degeneration
BLI	Bio-layer interferometry
BSA	Bovine serum albumin
C75	Cysteine 75
cDNA	Complementary deoxyribonucleic acid
CHP	Cumene hydroperoxide
CT	Cycle threshold
DMEM	Dulbecco's modified Eagle's medium
DMF	Dimethyl fumarate
DRF	Diroximel fumarate
EAE	Experimental autoimmune encephalomyelitis
EDTA	Ethylenediaminetetraacetic acid
FCS	Fetal calf serum
Fe	Iron
Fe^{2+}	Ferrous iron
Fe^{3+}	Ferric iron
FeS	Iron-sulfur
FSP1	Ferroptosis suppressor protein 1
GPX4	Glutathione peroxidase 4
GR	Glutahione reductase
GRSF1	Guanine-rich sequence-binding factor 1
Grx1	Glutaredoxin 1
Grx2	Glutaredoxin 2
Grxs	Glutaredoxins
GSH	Glutathione
GSS	Glutathione synthase
GSSG	Glutathione disulfide
H_2O	Water
H_2O_2	Hydrogen peroxide

H_2S	Hydrogen sulfide
HMOX	Heme oxygenase
HOIP	HOIL-interacting protein
HPE-IAM	β-(4-hydroxyphenyl)ethyl iodoacetamide
I/R	Ischemia/reperfusion
IC_{50}	Half-maximal inhibitory concentration
IMS	Intermembrane space
IRE	Iron-responsive elements
IRI	Ischemia/reperfusion injury
IRP	Iron-regulatory proteins
JNK	c-Jun N-terminal kinase
KEAP1	Kelch-like ECH-associated protein 1
Lip-1	Liproxstatin-1
LUBAC	Linear ubiquitin chain assembly complex
MASLD	Metabolic dysfunction-associated fatty liver disease
MBOAT	Membrane-associated O-acyl transferase
MD	Molecular dynamics
MEA	Microelectrode array
MEF	Mouse embryonic fibroblast
MMF	Monomethyl fumarate
MS	Multiple Sclerosis
MUFA	Monounsaturated fatty acid
NADPH	Nicotinamide adenine dinucleotide phosphate
NAFLD	Non-alcoholic fatty liver disease
NEM	N-ethylmaleimide
NO	Nitric oxide
OA	Osteoarthritis
OASF	Osteoarthritis synovial fibroblast
OTUB1	Ovarian tumor deubiquitinase 1
PA	Phosphatidic acid
PBS	Phosphate-buffered saline
PC	Phosphatidylcholine
PCOOH	Phosphatidylcholine hydroperoxide
PD	Parkinson’s disease
PE	Phosphatidylethanolamine
PI	Phosphatidylinositol
Prxs	Peroxiredoxins
PS	Phosphatidylserine
PUFA	Polyunsaturated fatty acid
PV^+	Parvalbumin-positive

qPCR	Quantitative polymerase chain reaction
RA	Rheumatoid arthritis
RASF	Rheumatoid arthritis synovial fibroblast
RCD	Regulated cell death
RNA	Ribonucleic acid
RPE	Retinal pigment epithelial
RPMI	Roswell Park Memorial Institute
RU	Relative units
SFA	Saturated fatty acid
SSMD	Sedaghatian-type spondylometaphyseal dysplasia
TFR1	Transferrin receptor 1
Trx	Thioredoxin
UdRPCs	Urine-derived renal progenitor cells
WT	Wild-type
γ-GCL	γ-glutamylcysteine ligase

15.2 Acknowledgement/Danksagung

First and foremost, I would like to thank my doctoral supervisor, PD Dr. Carsten Berndt, for supporting me from the very beginning of my academic journey and for continuously shaping and developing this project. I am especially grateful for the trust and patience extended to me throughout this time. I also deeply appreciate the many opportunities to present my research at international conferences and to establish valuable collaborations and networks across borders.

I would also like to thank my mentor, Prof. Dr. Petra Bauer, for her support, valuable discussions, and the revision of this thesis.

I am very grateful to Prof. Dr. Dr. Sven Meuth and Prof. Dr. Orhan Aktas for their financial support and for providing the great infrastructure that made this work possible.

A big thank you to all collaborators who contributed to the success of this project, whether through inspiring discussions or experimental support. In particular, I would like to thank Dr. Gereon Poschmann for the mass spectrometric analyses; PD Dr. Dr. Christopher Host Lillig and Yana Bodnar for their work on the molecular dynamics simulations; Dr. Manuel Etzkorn and Lora Denson for providing the nanodiscs and supporting the membrane binding experiments; Prof. Dr. Yvonne Janssen-Heininger for the Grx1 knockout cells; Prof. Dr. Christoph Thiele for the lipidomics analyses; Prof. Dr. Dr. Takaaki Akaike and Dr. Uladzimir Barayeu for the GSH measurements; Dr. Torsten Lowin for providing the patient samples; and last but not least, Dr. Irina Ingold and Dr. Marcus Conrad for generating the GPX4 cysteine mutants, for the close scientific exchange, and for the opportunity to visit their lab in Munich, which allowed me to discover new methods.

My thanks go to the SPP 2306 for the opportunity to present my work to other scientists in the field of ferroptosis and for the many interesting discussions. I would like to thank the GRK 2578 and iBrain for their financial support and for allowing me to attend conferences and present my research. I am also grateful to Biogen for their generous funding.

I extend my deepest thanks to the entire AG Berndt and all my colleagues at the Clinic for Neurology for the excellent collaboration, the warm and collegial atmosphere, and the constant support. I would also like to thank the students I have had the pleasure of supervising over the years, especially Carlotta John and Morris Haid.

Now, I want to especially mention Andrea Issberner, Laura Furlan, Derya Bachir, Diana Klees, Anne Busch, Pascal König and of course the "Bierchen oder so*" crew: Christina Hecker, Vera Dobelmann, Thomas Hildebrandt, and Michael Dietrich. You have all been

not only wonderful colleagues, but also dear friends. Your support, humor, and companionship made this time truly special, and I sincerely hope we will stay connected in the future.

To my friends and family, thank you for standing by me from the very beginning of my studies and for your unwavering pride and encouragement. A special thank you to my mother Simone and my sister Louisa – your support means the world to me. A heartfelt thank you to Annette for the careful proofreading of my thesis.

Finally, my deepest gratitude goes to Magnus. Thank you for being by my side for the past seven years. Your support, love and belief in me has given me the strength to never doubt myself. You inspire me every day.

All that remains is to say:

Thank you all – what an incredible journey this has been!

15.3 Declaration/Erklärung

Ich versichere an Eides statt, dass die Dissertation von mir selbständig und ohne unzulässige fremde Hilfe unter der Beachtung der "Grundsätze zur Sicherung guter wissenschaftlicher Praxis an der Heinrich-Heine-Universität Düsseldorf" erstellt worden ist.

Diese Dissertation wurde bei keiner anderen Institution in dieser oder ähnlicher Form eingereicht und es wurden keine erfolglosen Promotionsversuche unternommen.

Düsseldorf, den 05.05.2025

Leonie Christin Thewes